MICRO- AND MACROSCOPIC PHOTONIC CONTROL OF MATTER

By

Anton Ryabtsev

A DISSERTATION

Submitted to
Michigan State University
in partial fulfillment of the requirements
for the degree of

Chemistry – Doctor of Philosophy

2016

ABSTRACT

MICRO- AND MACROSCOPIC PHOTONIC CONTROL OF MATTER

By

Anton Ryabtsev

This dissertation outlines the development of several methods and techniques that enable comprehensive control of laser-matter interactions and nonlinear optical processes using shaped femtosecond pulses. Manipulation of the spectral phases and amplitudes of femtosecond laser pulses provides an effective way to adjust laser parameters, both those intrinsic to pulse generation within a laser and those induced by laser-matter interactions. When coupled with a fundamental understanding of the interactions between a laser's electric field and the molecules in the propagation media, these methods make the behavior of laser pulses predictable and allow the experimental information they carry to be extracted accurately. The ultimate motivation is to enhance the accuracy and reproducibility of spectroscopic measurements and to control nonlinear processes during light-matter interaction using shaped femtosecond pulses.

Ultrafast laser systems have become one of the most important scientific tools in femtochemistry, nanoscale material science, chemical detection and sensing, and many other applications where processes occur at femtosecond (fs, 10^{-15} of a second) timescales or when broad laser bandwidths are required. As with any measuring instrument, it is very important to know system's exact parameters in order to make meaningful, accurate and reproducible measurements. For ultrafast lasers, these parameters are the intensities of the spectral components, the spectral phase, the temporal profile, the pulse energy, and the spatial laser beam profile. Due to broadband nature of ultrafast laser sources, they are very sensitive to propagation media: gaseous, liquid or solid matter along the paths of laser pulses to the sample, including the material of the sample itself. Optical parameters describing the propagation media, such as linear and nonlinear dispersion, and birefringence, as well as physical parameters, such as temperature and pressure, all affect laser pulse parameters. In order for measurements not to be skewed, these interactions need to be taken into account and mitigated at the time of the experiment or handled later in data analysis and simulations.

Experimental results are presented in four chapters. Chapter 2 describes two topics: (1) single-shot real-time monitoring and correction of spectral phase drifts, which commonly originate from temperature and pointing fluctuations inside the laser cavity when the pulses are generated; (2) an all-optical method for controlling the dispersion of femtosecond pulses using other pulses. Chapter 3 focuses on the effects of the propagation media—how intense laser pulses modify media and how, in turn, the media modifies them back—and how these effects can be counteracted. Self-action effects in fused silica are discussed, along with some interesting and unexpected results. A method is then proposed for mitigating self-action processes using binary modulation of the spectral phases of laser pulses. Chapter 4 outlines the design of two laser systems, which are specifically tailored for particular spectroscopic applications and incorporate the comprehensive pulse control described in previous chapters. Chapter 5 shows how control of spatial beam characteristics can be applied to measurements of the mechanical motion of microscale particles and how it can potentially be applied to molecular motion. It also describes an experiment on laser-induced flow in air in which attempts were made to control the macroscopic molecular rotation of gases.

My research, with a pulse shaper as the enabling tool, provides important insights into ultrafast scientific studies by making femtosecond laser research more predictable, reliable and practical for measurement and control. In the long term, some of the research methods in this thesis may help the transition of femtosecond lasers from the laboratory environment into clinics, factories, airports, and other everyday settings.

ACKNOWLEDGEMENTS

My journey toward Ph.D. degree started a few years ago with a very persistent push from my Russian advisor Olga Smirnova at Bauman Moscow State Technical University. She basically made sure that I do not miss by far the greatest opportunity in my life to get graduate education at Michigan State University. I thank her for that opportunity and for her personal care for me.

I would like to thank all previous and current members of Dantus Research Group whom I had honor to work with all these years. They helped me to get my knowledge and hands-on experience in chemistry, lasers, optics, physics and other various fields of science. Special thanks go to my lab mates Gennady Rasskazov, Ilyas Saytashev and a wonderful theoretician Vadim Lozovoy for all collaborative work and for creating a home environment away from real home.

I would like to give special acknowledgements to my professor Marcos Dantus for all research projects he trusted me to work on and for the funding to complete them. I have learned so much from him, both about science and life. For me, being an international student, he has become more than just Principal Investigator, rather a mentor and a role model. I will remember his invaluable lessons for the rest of my life.

There is one more person who brought a lot of great ideas and solutions in all of my projects - Dmitry Pestov. I am grateful to Dmitry for that and for answering virtually all my questions.

And last, but by no means least, I want to thank my closest family members: mother, wife and daughter. I would not have survived the graduate school without your support.

TABLE OF CONTENTS

LIST OF FIGURES

KEY TO ABBREVIATIONS

2D	Two dimensional
AC	Autocorrelation
BBO	Beta barium borate
BPS	Binary phase shaping
CARS	Coherent anti-Stokes scattering
CFWM	Cascaded four-wave mixing
CPA	Chirp pulse amplification
CW	Continuous-wave
DFB	Distributed feedback
DM	dielectric mirror
DSLR	Digital single-lens reflex
EDFA	Erbium-doped fiber amplifier
FTSI	Fourier transform spectral interferometry
FWHM	Full width at a half maximum
FWM	Four-wave mixing
GDD	Group delay dispersion
GVD	Group velocity dispersion
HNLF	Highly nonlinear fiber
HWP	Half wave plate
IM	Intensity modulator
LDV	Laser Doppler velocimetry
LG	Laguerre-Gaussian
LI-GVD	Laser-induced group velocity dispersion
LMA	Large mode area

MI	Modulation instability
MII	Multiphoton intrapulse interference
MIIPS	Multiphoton intrapulse interference phase scan
MTV	Molecular tagging velocimetry
ND	Neutral density
OAM	Optical angular momentum
OKE	Optical Kerr effect
OSA	Optical spectrum analyzer
PBS	Polarized beam splitter
PCF	Photonic crystal fiber
PIV	Particle image velocimetry
PM	Polarization-maintaining
QWP	Quarter wave plate
RDE	Rotational Doppler effect
RT-MIIPS	Real-time multiphoton intrapulse interference phase scan
SHG	Second harmonic generation
SLM	Spatial light modulator
SMF	Single mode fiber
SOD	Second order dispersion
SP	Short pass
SPM	Self phase modulation
Ti	Titanium
TL	Transform limited
TOD	Third order dispersion
VND	Variable neutral density
WDM	Wavelength division multiplexer

XFROG	Cross-correlation frequency resolved optical gating
Yb	Ytterbium

Chapter 1 Introduction

Increasingly, at atomic and molecular levels, the ability to control processes is as important as the ability to measure their effects. The Office of Science for the U.S. Department of Energy has identified a set of five Grand Challenges for basic science [1]. The word *control* or its synonyms (manipulate, orchestrate and master) can be found in every one of their descriptions, and sometimes more than once. For example, "How do we control materials processes at the level of electrons?" and "How do remarkable properties of matter emerge from complex correlations of the atomic or electronic constituents and how can we control these properties?" In addition, one of the "Big Ideas for Future NSF Investments" in the National Science Foundation's research agenda for next few decades, called "The Quantum Leap: Leading the Next Quantum Revolution", has the aims of observing, manipulating and controlling particles and energy at quantum scales [2]. Science and technology are tightly linked together and drive each other; the goals described above can only be met through the development of instrumentation that is capable of performing the tasks.

In fundamental research in atomic and molecular science, the physical dimensions of interest are extremely small compared to the macroscopic world: typical spatial scales are measured in nanometers, and typical timescales are measured in picoseconds (10^{-12} s), femtoseconds (10^{-15} s) or even attoseconds (10^{-18} s). Reaching into the world of atoms and molecules requires very specialized instrumentation, and amongst the most important are lasers. The invention of lasers, and particularly ultrafast lasers, has greatly impacted our understanding of nature. The excellent spatial coherence of lasers means that they can be focused onto tiny spots, down to nanometers. Their broad, coherent bandwidths, in some cases exceeding an optical octave, mean that they can produce very short-duration pulses. Pulses shorter than 100 fs are routinely available and, for a Ti:sapphire oscillator, it has been possible to reach a few (or even single) optical cycles with durations < 5 fs [3, 4]. Supercontinuum generation, in which one or more nonlinear processes combine to generate new frequency components, is widely used in laser systems to broaden spectra and shorten pulse durations [5, 6]. Ultrafast lasers have become important scientific tools

and a necessary part of almost any experimental setup in physical chemistry research. As for any metrology instrument, the accuracy, precision, and stability of laser pulse parameters determine the quality of the measurements. As such, in order to get meaningful and reproducible results, it is crucially important to properly characterize laser pulses and to be able to correct or alter their parameters. Among the applications that require especially high-quality pulses are nonlinear spectroscopy, nonlinear multiphoton microscopy, femtosecond laser eye surgery and femtosecond micromachining.

Ultrafast lasers are not only tools for the measurement and control in femtosecond science, they also form the basis of attosecond science, the next level of fundamental research in the X-ray region of the electromagnetic spectrum. The generation of attosecond pulses is based on high-harmonic generation driven by femtosecond lasers and requires pushing the quality of femtosecond pulses to the limits of perfection [7]. Therefore, the ability to control the femtosecond laser sources is crucial for creating attosecond pulses with desirable parameters.

With these motivations, the goal of my research was to expand our ability to characterize and control laser pulses and light-matter interaction, and in turn improve our understanding of how lasers can be used to control chemical and physical processes on the fundamental level.

1.1 Introduction to femtosecond pulses

Ultrafast lasers are very complex instruments. Cavity misalignment, temperature fluctuations, and degradation of optics and optoelectronics all contribute to constant changes in laser performance. Most users of femtosecond lasers assume that the laser parameters are stable up to the specifications provided by the manufacturer, but this is usually incorrect and can lead to incorrect experimental measurements. In order to get the desired pulse parameters at the sample, pulses generally need to be controlled. Common methods of pulse control are based on gratings and prisms [8-10], dispersion compensation mirrors [11], and fiber Bragg gratings [12]. These methods have two major drawbacks: first, they offer limited control, usually affecting only linear chirp, as discussed in the next section; and second, since gratings and prisms are passive optics, they are static and cannot be controlled in real-time or with high-speed. In the Dantus research group, we rely on adaptive pulse shapers based on spatial light modulators (SLM) and enabled

by multiphoton intrapulse interference phase scan (MIIPS). In this dissertation, I take advantage of the great flexibility and accuracy of a well-calibrated pulse shaper to solve the problem of how to comprehensively control laser pulses and light-matter interaction.

To learn how one can control an ultrashort pulse, we need to understand what an ultrashort pulse is and how it is formed. A femtosecond pulse can be considered to be a collection of electromagnetic waves with different frequencies that overlap in space and time and constructively interfere. The electric field of a pulse $E(\omega)$ can be written as a sum of electric fields of all frequency components:

$$E(\omega) = \sum_i E(\omega_i) e^{-i\varphi_i(\omega)}, \tag{1}$$

where $E(\omega_i)$ and $\varphi(\omega_i)$ are the amplitude and phase of the i-th component of the electric field, respectively. The presence of different frequencies implies that the spectrum of such a pulse, $I(\omega)$, is broadband with a bandwidth that is inversely proportional to pulse duration. The pulse profile in the time domain is the temporal intensity of the pulse, which can calculated by taking the squared modulus of the electric field in the time domain, $E(t)$:

$$E(t) = \int \sqrt{I(\omega)} e^{i\varphi(\omega)} e^{-i\omega t} d\omega, \tag{2}$$

$$I(t) = \left| E(t) \right|^2, \tag{3}$$

where $\varphi(\omega)$ is the spectral phase of the femtosecond pulse. Figure 1 illustrates the relationship between spectral and temporal parameters of a femtosecond pulse. Figure 1a shows the experimental broadband spectrum of a Ti:sapphire oscillator (Venteon) with specially designed dispersion compensation dielectric mirrors, between 680 nm and 1040 nm. Figures 1b and 1c show the calculated electric field and intensity profiles of ultrashort pulses corresponding to this spectrum. Pulse duration is conventionally defined as the full-width half maximum (FWHM) of the intensity profile in the time domain $I(t)$ and is found to be 10.2 fs for the laser in Figure 1.

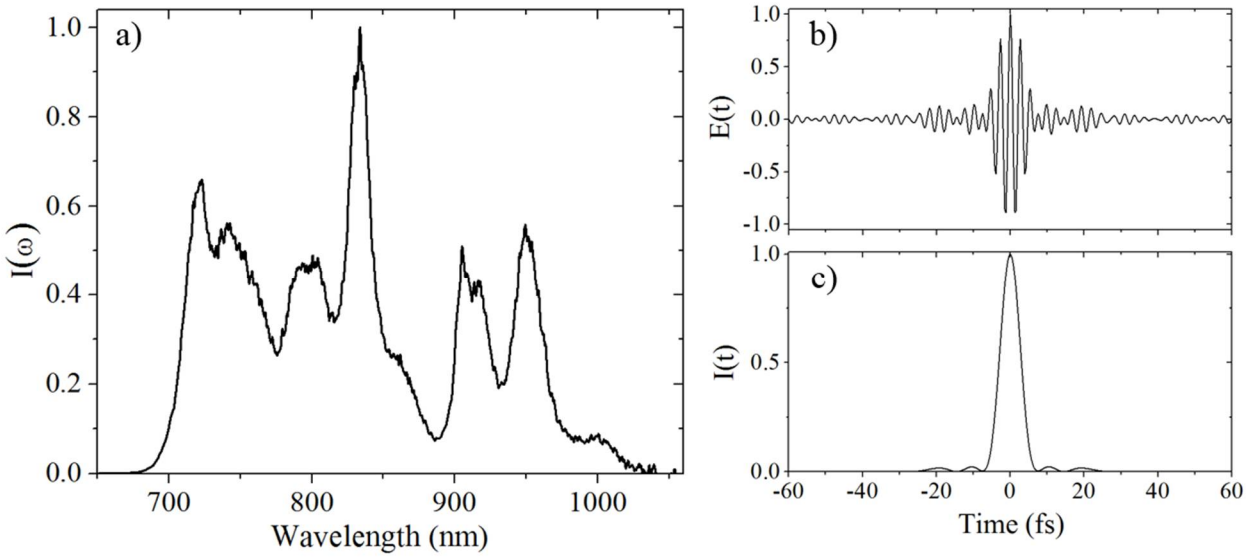

Figure 1. Experimental spectrum of an ultra-broadband Ti:sapphire oscillator (a), and calculated electric field (b) and intensity profiles (c) in the temporal domain.

The relationships between the phases of different spectral components of laser radiation defines the temporal coherence of laser pulses. If correlation is strong, then the radiation is considered coherent and the components of the electric field yield a single well-defined pulse. In the correlation is weak, then the radiation is considered incoherent. In the limiting case of random phases, the pulse would be a noise-like feature. Coherence can be regarded as a measure of the degree to which pulses are controllable. In this dissertation I consider all pulses from Ti:sapphire oscillators and amplifiers to be fully coherent. For the sources described in Chapter 4, I provide an assessment of the coherence and discuss the results.

The spectrum of a laser is determined by the mechanism by which the pulse is generated in a laser cavity (i.e. by the number of laser modes supported by the cavity), the gain bandwidth of the gain medium, and the mode-locking mechanism. For example, Ti:sapphire oscillators with Kerr-lens mode-locking [13] have Gaussian spectra, and fiber lasers operating in a normal-dispersion regime have characteristic "bat-ears" spectra [14]. The spectrum of a Venteon oscillator shown in Figure 1a exhibits intracavity spectral broadening due to the use of dispersion compensation multi-layer mirrors. The modulation periods of spectrum (periodic variations in spectral intensity) are related to the thicknesses of the layers in the dielectric coating. Measurements of the spectrum are can be made trivially using

commercially-available spectrometers. Amplitude modulation is an attractive possibility, from the point of view of control, but the inevitable energy losses and broadening of pulses are negative factors in intensity-sensitive applications such as nonlinear spectroscopy and multi-photon microscopy.

Knowing the laser spectrum alone is not sufficient for characterizing a femtosecond pulse. As one can see in Equation 2, for a complete characterization, the spectral phase $\varphi(\omega)$ must also be measured. The spectral phase can be expanded in a Taylor series around the central frequency of the laser ω_0:

$$\varphi(\omega) = \varphi_0 + \varphi_1 \cdot (\omega - \omega_0) + \frac{\varphi_2}{2!} \cdot (\omega - \omega_0)^2 + \frac{\varphi_3}{3!} \cdot (\omega - \omega_0)^3 + \ldots \quad , \tag{4}$$

where the first term is related to the constant phase, or carrier envelope phase, of the pulse; the second term is related to a delay of the pulse in time; the third and fourth terms are called second- and third-order dispersions, respectively; and all subsequent terms are collectively referred to as high-order dispersion. The first two terms do not change the pulse profile, but the others do. The effect is summarized in Figure 2. The spectrum is the same in all panels and corresponds to a typical spectrum from a Ti:sapphire amplifier. The top panels correspond to $\varphi(\omega)$=0, where the pulse profile has the shortest possible pulse duration for given spectrum, called transform-limited (TL) pulse duration. The central panels have a second-order dispersion (SOD), or quadratic phase profile, also known as a linear chirp, equal to 1000 fs^2. Here, the pulse broadens, and the peak power decreases accordingly. Furthermore, long wavelength (red) components travel faster than short wavelength (blue) components, or vice versa for a chirp with opposite sign. The bottom panels correspond to a third-order dispersion (TOD), or cubic phase profile, equal to -40000 fs^3. The pulse gets broader and develops a tail of pre-pulses, which precede or follow the main pulse according to the sign of the TOD. Higher-order dispersion leads to more complex pulse modulation, but usually with smaller effects on peak power and pulse duration.

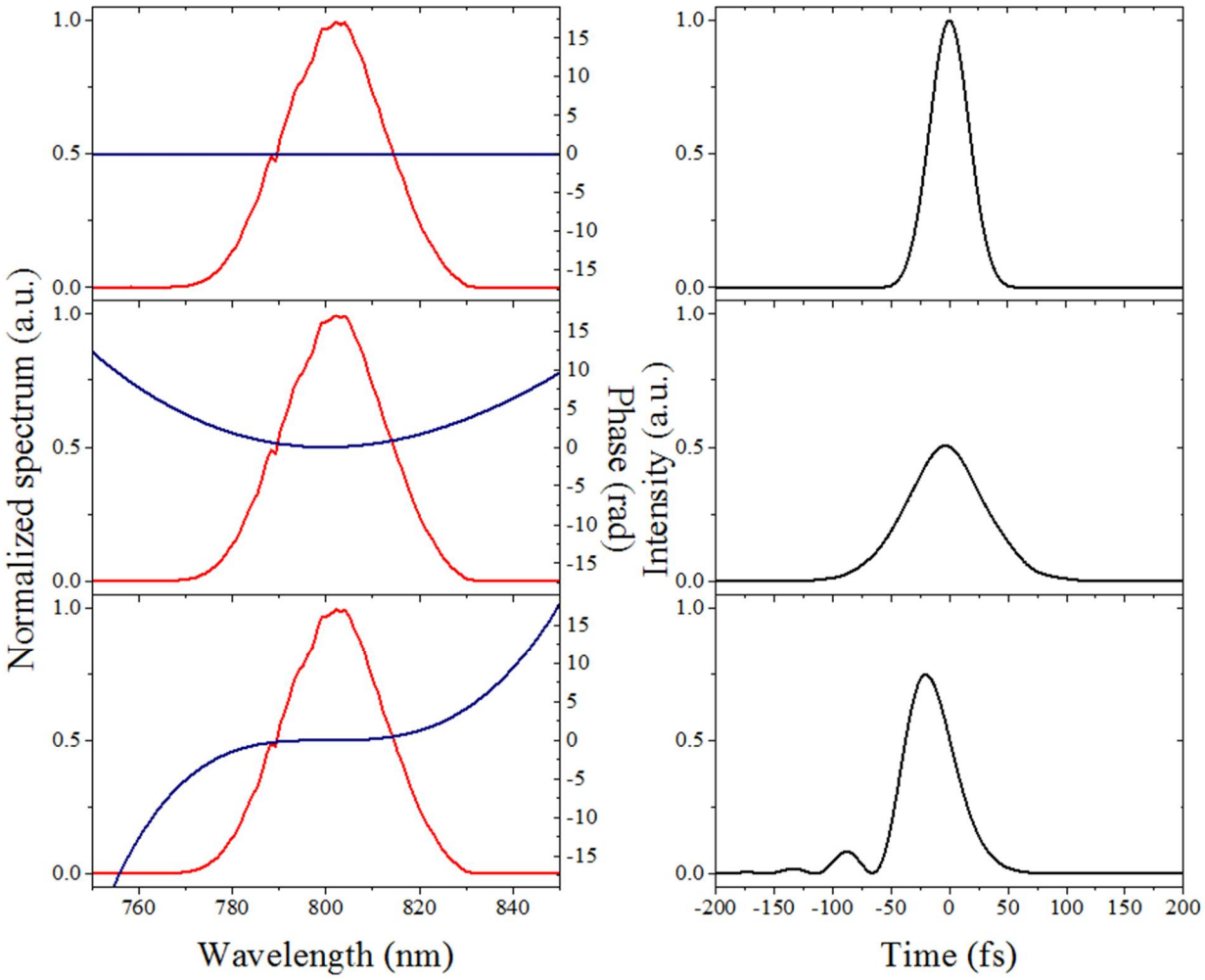

Figure 2. The effect of spectral phase on the pulse profile showing the spectra (left column) and corresponding pulse profiles (right column) for three different spectral phases: transform limited (top), chirp 1000 fs^2 (middle), and third-order dispersion −40 000 fs^3 (bottom).

When a pulse propagates through a medium, it undergoes a phase change due to material (static) dispersion. This change is related to the frequency-dependent refractive index of the material. Since an ultrashort pulse possesses a broad spectrum, different spectral components are delayed differently in the material causing group velocity dispersion (GVD). These phase changes accumulate as the pulse progresses along its path, as illustrated in Figure 3.

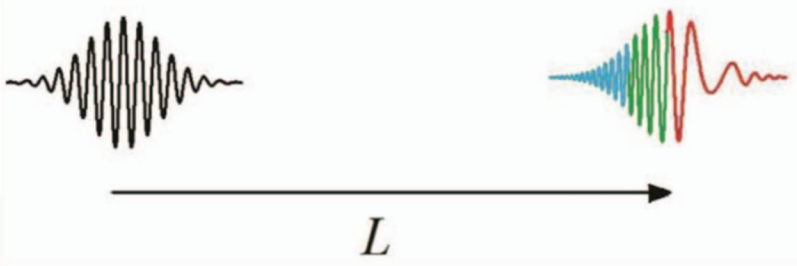

Figure 3. Schematic diagram showing phase distortions accumulated by a laser pulse while propagating through an optical medium with frequency-dependent refractive index. Adapted from [15].

This interaction can be represented mathematically using:

$$E(\omega) = \sum_{\omega} E(\omega) e^{i(k(\omega)x - \omega t)}, \tag{5}$$

where $k(\omega)$ is a frequency-dependent wavenumber given by $k(\omega) = \omega n(\omega)/c$. In this expression $n(\omega)$ is the refractive index of the medium and c is the speed of light. The refractive index is affected by the strength of the oscillator and the frequencies of electronic and vibrational resonances of the medium. For transparent media, one can assume that there is a single resonance in the vacuum ultraviolet region and that dispersion depends primarily on the oscillator strength of that resonance. The phase accumulated by a pulse inside the medium with length L can be presented as a Taylor series:

$$\varphi(\omega) = [k_0 + k' \cdot (\omega - \omega_0) + \frac{k''}{2!} \cdot (\omega - \omega_0)^2 + \frac{k'''}{3!} \cdot (\omega - \omega_0)^3 + ...] \cdot L \tag{6}$$

As with Equation 4, the first two terms do not affect the pulse, and the effects of the following terms—SOD, TOD, and high order dispersions—are illustrated in Figure 2. For intense laser pulses, in addition to the static dispersion, laser-induced dispersion starts to play a significant role. This effect is related to the intensity-dependent nonlinear refractive index and is addressed in Chapter 3.

1.2 Characterization and control of laser parameters

Phase distortion—usually as a combination of second-, third- and higher-order dispersion terms, is inevitable in femtosecond laser experiments. Lasers are never perfect to begin with, and their pulses are rarely transform limited. They are affected by the physics of laser generation and misalignment of internal

components. In addition, pulses acquire phase distortions when propagating through a dispersive medium or due to interactions with dispersive optics. For many applications, it is important to compensate for this phase distortion or compress pulses to transform-limited durations. There are many methods for pulse compression including grating and prism compressors, dielectric chirp mirrors, and fiber Bragg gratings. These passive compression schemes are often easy to implement and can compensate for a significant amount of phase distortion, but they are not able to compensate for higher-order phase dispersion. To have comprehensive control of spectral phase, it is necessary to use adaptive pulse compressors or pulse shapers [16]. A pulse shaper is an optical device that acts on a pulse in the spectral domain to affect a change in shape in the temporal domain. A typical pulse shaper is shown in Figure 4. It consists of a grating, which angularly disperses the incoming light, and a lens, which focuses individual wavelength components onto a phase mask. The mask is positioned in the Fourier plane of a pulse shaper and can act on the spectral parameters of an ultrashort pulse. Following the mask, the light goes through the same optical components, a lens and a grating, so that the output is again a collimated beam. With the invention of liquid-crystal-based spatial light modulators, replacing a fixed mask in a pulse shaper [16], it became possible to actively control spectral components of a pulse. SLMs contain liquid crystal elements with electronically addressable pixels, which act as a programmable mask. By applying voltage signals to pixels in liquid crystal array, one can use the birefringent properties of liquid crystals to effect a corresponding phase retardance. It effectively changes the spectral phase of a pulse, which according to Equations 2 and 3, changes the pulse in the time domain. The combination of two SLM masks gives the ability to control spectral amplitude or polarization, which in turn, gives virtually full control of a laser pulse.

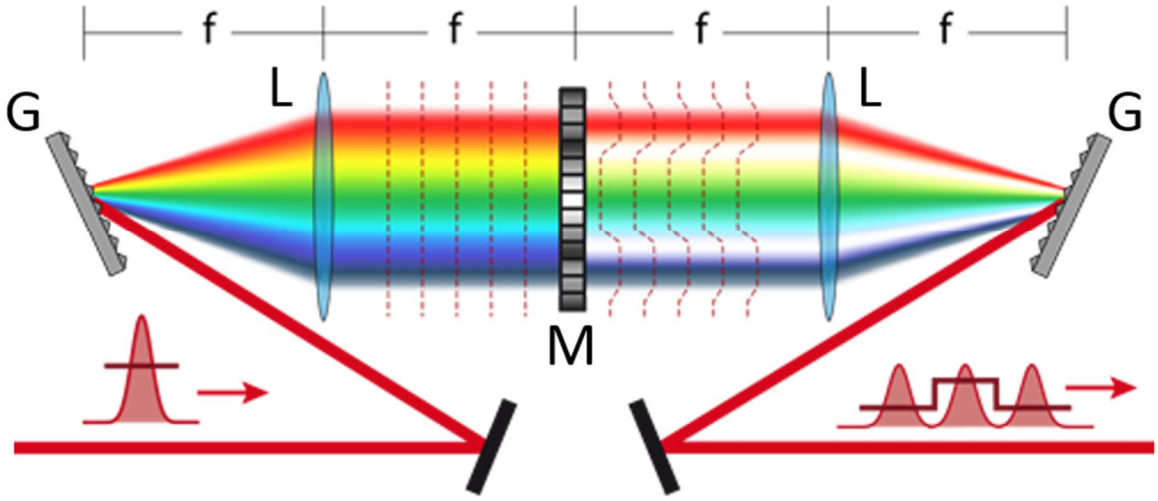

Figure 4. Schematic illustration of a 4-f pulse shaper. G are gratings, and L are lenses with focal length f. Adapted from http://web.physik.uni-rostock.de/optik/en/for_tec_d_en.html.

The main characteristics of the pulse shaper are given by SLM parameters, such as the number and size of the pixels, and the optical design. Two common types of SLM are a transmissive linear array of 128 or 640 pixels and a 2D matrix of 600 × 800 pixels with a reflective substrate. The focusing lens and the grating, which determines the spread of laser's spectral components on the SLM, define the optical resolution of a shaper. Better optical resolution allows more accurate characterization and compression. A folded design, where a mirror in Fourier plane reflects the light back through the same optical components through which the light enters, usually simplifies the alignment and minimizes the effect of unwanted shaper-induced phase and spatial distortions on pulses.

The Dantus research group has developed a series of methods for simultaneous pulse characterization and compression known as multi-photon intrapulse interference phase scan (MIIPS) [17-19]. These are based on a pulse shaper design with an SLM as a programmable mask. They rely on the sensitivity of second-harmonic generation (SHG) signal to the spectral phase of a pulse that arises from the constructive and destructive interferences inside it. By adding a known reference phase to the unknown phase of a laser pulse and tracking changes to the SHG signal, the algorithm is capable of determining the original phase distortions in the pulse. After the measurement, the pulse shaper applies a

compensation phase which is of opposite sign to the measured one. After a few iterations, the phase distortion of original pulse (SOD, TOD, and higher-order terms) is compensated for and pulse achieves the shortest possible transform-limited duration. The most important characteristic of MIIPS compression is that it can be performed with the sample in situ, allowing mitigation of all phase distortions accumulated by a laser pulse along its path.

1.3 Controlling laser-matter interaction

Femtosecond pulses, with pulse durations on the order of, or faster than, the time scales of electronic, vibrational and rotational energy transfer, help physicists and chemists understand processes that occur during and following light-matter interactions. Processes such as the excitation, fragmentation and ionization of molecules under intense laser fields can be controlled using the phase and amplitude of laser pulses [20]. Linearly-chirped pulses or phase step scans are successfully used to study solvated molecules in processes such as inhomogeneous broadening and solvatochromic shift, and to determine their electronic coherence lifetimes [21]. They can also be used to study fluorescence and stimulated emission [22]. Phase and amplitude control of laser pulses is also important in nonlinear spectroscopy. Pulse shaping methods have been successfully used to demonstrate chemically-selective imaging based on coherent Raman processes [23, 24]. A laser system with comprehensive control of parameters, which is capable of performing fast standoff imaging of chemicals in eye-safe wavelength regions, is presented in Chapter 4.

Chapter 2 Optical pulse control

This chapter discusses two topics related to the control of laser parameters with the goal of maintaining undistorted pulse shape at the location of a sample. The first one discusses the development of an automated system capable of real-time tracking and correction of laser's peak power originating from fluctuations in laser spectrum and in spectral phase. Theoretical explanation of the system's operation as well as experimental results for different types of lasers (a fiber oscillator and a Ti:sapphire amplifier) are presented. The second topic discusses a method of a laser pulse dispersion control without conventional optical elements, such as gratings, prisms or SLMs. It is based on an interaction of a weak pulse with a strong pulse inside a nonlinear media via cross-phase modulation. The proof of concept experimental implementation is presented and results are discussed.

2.1. Single-shot real-time dispersion measurement and control

Femtosecond laser systems are being used for an increasingly large number of applications given their ability to deliver high peak power densities (from 10^{10} W/cm^2 to 10^{16} W/cm^2) with very modest pulse energies (from 10^{-12} J to 10^{-3} J). Some of these technologies have transferred from the research laboratory to real-world applications, for example, femtosecond refractive surgery [25], cataracts surgery [26], and material processing [27, 28]. While the laser sources have experienced great progress in terms of output pulse characteristics, reliability, and size, they are still notoriously complex and sensitive to changes in ambient environment. In addition to the static dispersion introduced by the laser components themselves and high-numerical aperture microscope objectives, modern ultrafast laser design needs to take into account laser-induced nonlinear optical processes such as self-phase modulation [29], and laser induced group velocity dispersion [30]. As a result, minute changes in cavity length or alignment lead to deterioration in pulse characteristics. Applications of femtosecond lasers outside of laser laboratories thus require automated dispersion and amplitude drift characterization and compensation in order to maintain optimum performance without human assistance. If this can be accomplished, femtosecond lasers from high-rep rate industrial to high-intensity femtosecond petawatt class lasers [31] could certainly benefit from the technology.

It is possible to achieve some degree of automated pulse optimization without using pulse characterization. Given that the integrated second harmonic generation intensity achieves a maximum value for transform limited pulses, this intensity can be used as feedback for a closed loop, while a pulse shaper compensates arbitrary phase dispersion [32, 33]. Unfortunately, the process is time consuming and the degree of success of this approach depends on the square of the noise level of the laser system. For many cases it is sufficient to optimize chirp by feeding back the integrated SHG intensity to a prism or grating compressor [34], an approach that has been adopted by some commercial systems. Given that tracking SHG intensity does not provide sufficient phase information, these systems require dithering the chirp to find the optimum value. Ideally, phase optimization is based on accurate phase characterization.

Measuring phase distortions requires pulse characterization, on-the-fly correction requires single-shot pulse characterization; a topic that has received considerable attention since the early 1990's [35-39]. Following the single-shot pulse characterization the information needs to be processed and used to actuate optics in the laser compressor or to a pulse shaper. Operationally, phase drifts manifest themselves in nonlinear phase distortion, primarily in the second- and sometimes third-order distortion of the spectral phase (SOD and TOD, respectively). Therefore, a method is needed to directly provide quantitative SOD and TOD information with minimal use of time consuming phase retrieval algorithms.

In this project [40] we took advantage of the inherent sensitivity of nonlinear optical processes to phase distortions. This sensitivity, in particular to SOD and TOD, was discussed in the context of multiphoton intrapulse interference for control of two- and three-photon laser induced processes [41]. In that article it was noted that TOD leads to narrowing of the SHG spectrum and the addition of SOD leads to a shift of the maximum SHG to longer wavelengths (when both are positive). The ability to shift the maximum in a nonlinear optical process, such as multiphoton excitation, has been patented and used for a number of applications such as selective two-photon microscopy [42, 43]. Here we extracted SOD and TOD values from changes in the SHG spectrum. It is worth noting that we are not proposing a pulse characterization method for arbitrary phase distortions in a previously uncharacterized laser pulse. The intention of the work is to measure and correct small deviations in SOD and TOD occurring in laser

system over time. The real-time version of multiphoton intrapulse interference phase scan (RT-MIIPS) presented is for monitoring and stabilization of pulse energies and peak powers for optimum unattended ultrafast laser performance over an indefinite period of time.

2.1.1 Principle of RT-MIIPS measurement of SOD

The principle behind RT-MIIPS method hinges on the fact that TOD causes a narrowing of the SHG spectrum but the maximum value remains at $2\omega_0$, however, addition of SOD causes a shift in the position of maximum SHG due to multiphoton intrapulse interference (MII) at shorter or longer SHG wavelengths (depending on the SOD sign); as illustrated in Figure 5. In this part of work we used a home-built Yb-doped fiber oscillator [44].

A plot of group delay, such as the one shown in Figure 5, shows the time-domain relationship between spectral components of the laser pulse. We observe SHG spectrum is narrowed compared to that of a transform limited pulse when the spectral phase has a significant amount of third-order (cubic) distortion because the group delay, which is the first derivative of spectral phase with respect to frequency, has a parabolic shape (Figure 5a, color curves). All spectral components symmetrically around the peak of the parabola are equally delayed, with delay increasing towards the wings of the parabola. Components with equal delay produce efficient constructive MII, however as the relative delay increases, destructive interference takes place resulting in a narrow peak in SHG spectrum. If TOD and consequently group delay is centered around laser central wavelength (Figure 5a, triangles), the resulting peak will appear in the middle of a spectral range, corresponding to the peak position of SHG spectrum at transform limited (TL) pulse (Figure 5b, triangles and gray solid line, respectively). Adding of SOD to a spectral phase is equal to adding a linear group delay term which shifts parabola to shorter or longer wavelengths for negative and positive SOD, respectively (Figure 5a, circles and diamonds). Shift of the group-delay parabola result in corresponding spectral SHG shifts (Figure 5b, circles and diamonds).

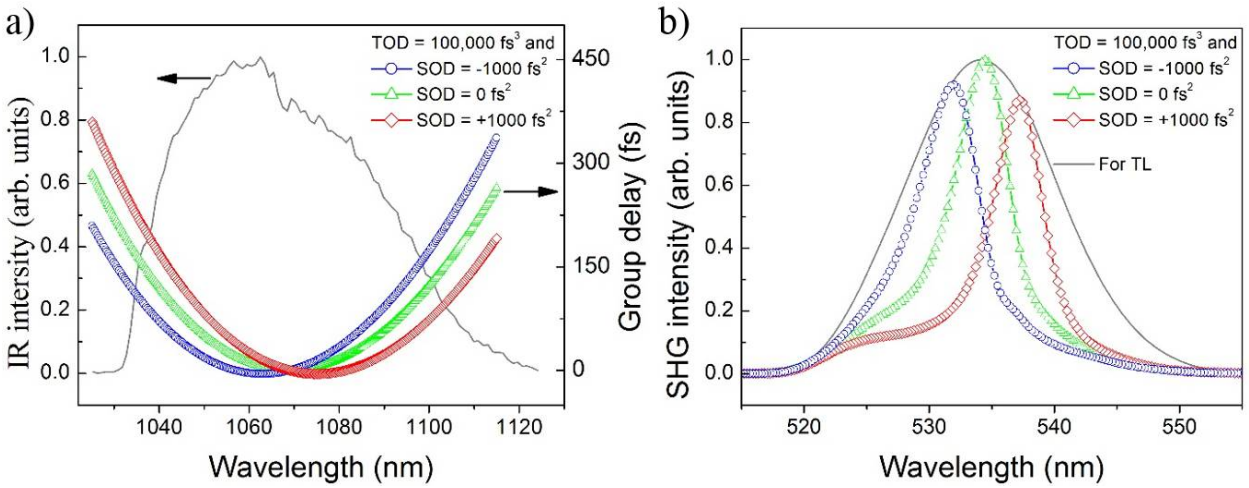

Figure 5. Principle of the RT-MIIPS measurement of SOD. (a) The experimental IR spectrum (black curve) from the Yb-doped fiber laser and the group delay curves corresponding to 3 spectral phases with different SOD values (see legend) and a fixed amount of TOD. (b) The SHG spectra calculated using the spectrum and phases from (a). Figure from [40].

The described behavior can be inferred from a mathematical analysis where the local maximum in the SHG spectrum at frequency $\omega_{\max}^{SHG} = 2\omega_{\max}$, where $\omega_{\max}$ is a fundamental frequency, corresponds to the spectral phase $\phi(\omega)$ of the fundamental spectrum that satisfies the relation:

$$\left.\frac{d^2\phi(\omega)}{d\omega^2}\right|_{\omega=\omega_{\max}} = 0 \quad . \tag{6}$$

The spectral phase with TOD only can be written as:

$$\phi(\omega) = \frac{\phi_3 \cdot (\omega - \omega_0)^3}{6} \quad , \tag{7}$$

where ω_0 is the central frequency of the fundamental laser spectrum and $\phi_3 = d^3\phi(\omega)/d\omega^3$ is the TOD. Substitution Equation 7 into Equation 6 results in $\phi_3 \cdot (\omega_{\max} - \omega_0) = 0$, which gives a local maximum in SHG spectrum at $\omega_{\max}^{SHG} = 2\omega_0$. When some amount of SOD ($\phi_2 = d^2\phi(\omega)/d\omega^2$) is added the spectral phase can be written as:

$$\phi(\omega) = \frac{\phi_3 \cdot (\omega - \omega_0)^3}{6} + \frac{\phi_2 \cdot (\omega - \omega_0)^2}{2} \quad . \tag{8}$$

Substitution Equation 8 into Equation 6 results in $\phi_2 + \phi_3 \cdot (\omega_{\max} - \omega_0) = 0$ i.e., the SHG peak shifts to $\omega_{\max}^{SHG} = 2 \cdot (\omega_0 - \phi_2 / \phi_3)$. Therefore, SOD changes are correlated with SHG peak shifts according to:

$$\Delta\omega_{\max}^{SHG} = -2 \cdot \phi_2 / \phi_3 . \tag{9}$$

From Equation 9, it follows that for a given positive TOD, the observed SHG spectrum peak shifts to shorter wavelengths when negative SOD is acquired by the pulse and vice versa. Given that laser pulses have spectra that are not ideal Gaussian functions, the method should be calibrated on the actual laser system to provide the most accurate results. The work was carried out using a home-built Yb-doped fiber oscillator producing sub-45 fs [44] and a reflective 4f pulse shaper (MIIPSBox640, Biophotonic Solutions Inc.). It is best to start with fully characterized pulses, which can be achieved by simply scanning SOD [45, 46]. The SHG spectrum for transform-limited pulses of the Yb fiber laser here covers the 515-555 nm range (bottom-to-bottom). The first step is to impose a reference phase mask with some amount of TOD to narrow SHG spectrum, which can be done with the pulse shaper or by introducing a dispersive optical element with the desired characteristics [30]. Here the cubic reference phase of +100,000 fs^3 is applied using a reflective 4f pulse shaper. The second step is to acquire a two-dimensional spectrogram as a function of linear chirped (Figure 6). The third step is to extract the position of the maximum SHG for each SOD value. Here we implement weighted averaging over spectral points above a fixed threshold to reduce the noise and achieve sub-spectrometer-limited resolution.

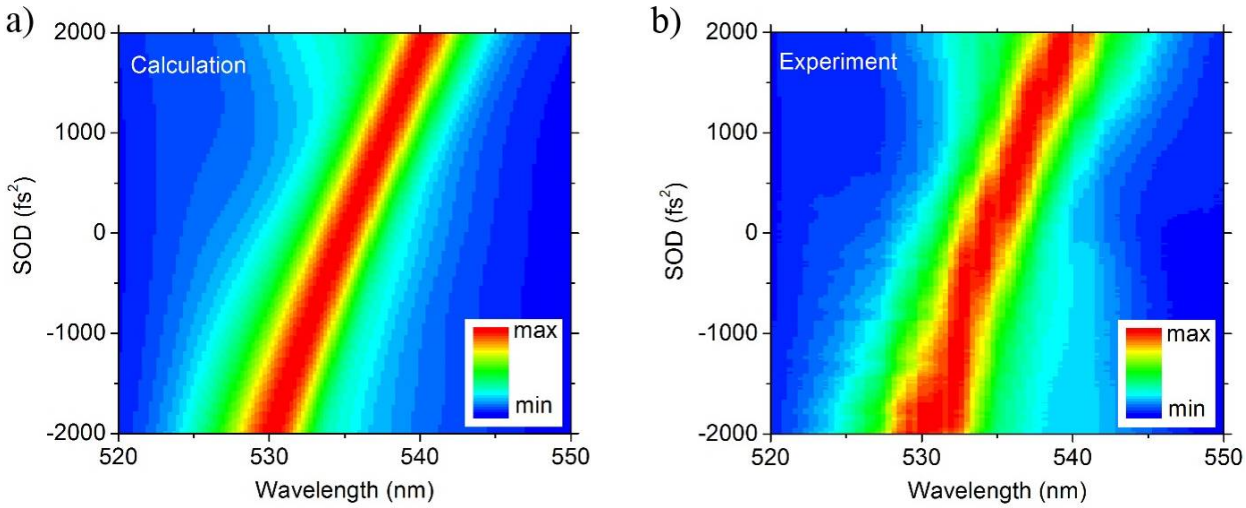

Figure 6. RT-MIIPS calibration for SOD measurements. (a) The SHG spectrogram calculated using the experimental laser spectrum. (b) Experimental SHG spectrogram. Calculated and experimental spectra correspond to a set of polynomial phases with SOD ranging from -2,000 fs^2 to 2,000 fs^2 (scanned) and TOD of 100,000 fs^3 (fixed). Every SHG spectrum is normalized. Figure from [40].

The wavelength of maximum SHG intensity as a function of SOD is fitted by a second-order polynomial, yielding the calibration curve. Once the one-to-one correspondence is established, one can accurately measure changes in SOD by acquiring a single SHG spectrum, and if the measurement corresponds to an undesired drift, the system can correct it. The standard deviation for the measured SOD values is found to be about 60 fs^2. It is worth noting that RT-MIIPS relies on spectroscopic changes in SHG (peak shifts) rather than on the intensity of SHG. Fluctuations in SHG intensity caused by noise limit integrated SHG-based methods. For instance, potentially minimal 2% fluctuations in integrated SHG result in uncertainty of ±150 fs^2 of SOD in a 40fs pulse. A long term drift of intensity, for instance due to pump diode power drifts/degradation, changes in reflection/transmission of optical elements, would cause a systematic drift. Of course the systematic intensity drifts can be corrected with regular re-calibration processes. RT-MIIPS on the other hand is not sensitive to intensity fluctuations. Its sensitivity is limited by the spectrometer resolution, therefore it can be used with very low laser intensities.

2.1.2 Principle of RT-MIIPS measurement of TOD

To measure and correct for both SOD and TOD, we have modified the reference phase to incorporate two cubic phase masks, which are offset spectrally, therefore, they have different group-delay

terms. The corresponding group delay for this reference phase consists of two parabolas (shown schematically in Figure 7a). Mathematically, the reference phase function can be written as:

$$\varphi_{ref}(\omega) = \begin{cases} \frac{\varphi_3}{6}(\omega-\omega_1)^3 + \tau\cdot(\omega-\omega_1) \quad if \quad \omega < \omega_0, \\ -\frac{\varphi_3}{6}(\omega-\omega_2)^3 - \tau\cdot(\omega-\omega_2) \quad if \quad \omega \geq \omega_0. \end{cases} \tag{10}$$

Here ω_1 and ω_2 are two frequencies within the spectrum equally offset from ω_0 ($\omega_1 < \omega_0$ and $\omega_2 > \omega_0$). Note that these are 'zero dispersion' frequencies if no phase distortion is present. In practice, they are defined through the corresponding wavelengths λ_1 and λ_2, which are calculated from the center wavelength λ_0 and offset $\Delta\lambda$ in nanometers;

$$\lambda_{1,2} = \frac{1}{2}\times\left(\lambda_0 \pm \Delta\lambda + \sqrt{\lambda_0^2 + \Delta\lambda^2}\right). \tag{11}$$

The amount of TOD (φ_3) introduced defines the sharpness of the local maxima in the SHG spectrum due to MII. The non-zero time delay τ allows suppressing sum frequency generation. The SHG spectrum due to the reference phase exhibits two local maxima, each corresponding to a different group delay parabola, as shown in Figure 7b. Due to the offset of the zero-dispersion points from the center (here λ_0 = 1070 nm, $\Delta\lambda$ = 30 nm), the maxima positions are affected by both SOD and TOD phase distortions and one can isolate the two contributions.

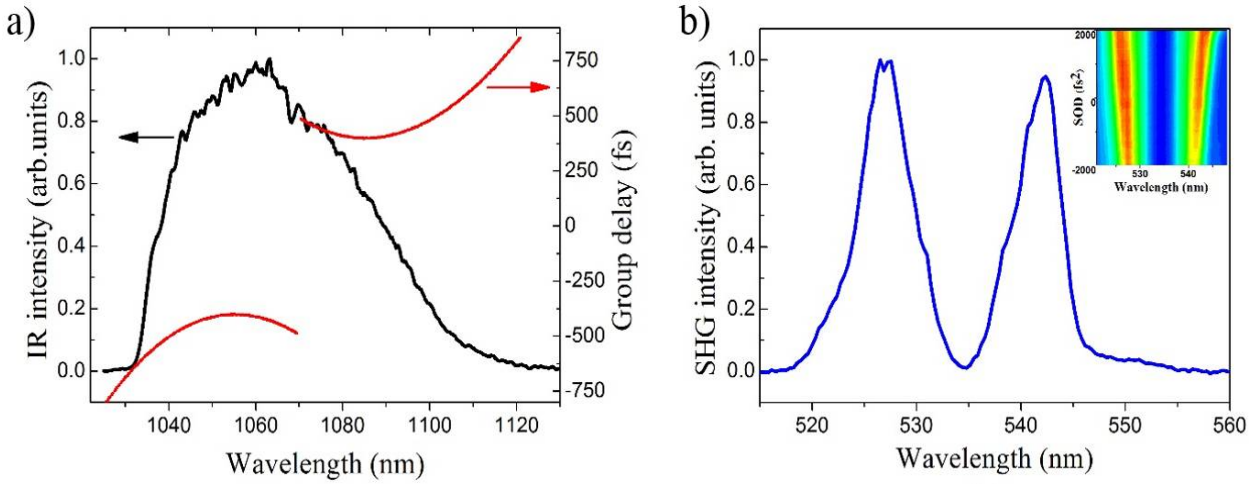

Figure 7. Principle of RT-MIIPS measurement of SOD and TOD. (a) Fiber laser fundamental spectrum and group delay corresponding to the reference phase mask (two incorporated cubic phase masks, see text). (b) SHG spectrum corresponding to the reference phase mask from (a). Inset – SHG spectrogram with SOD scanned from -2,000 to 2,000 fs^2. Figure from [40].

Indeed, if we define ω_A and ω_B as 'zero dispersion' frequencies in the presence non-zero phase distortion, the corresponding TOD ($\delta\varphi_3$) and SOD ($\delta\varphi_2$) drifts can be expressed as:

$$\begin{cases} \delta\varphi_3 = \varphi_3 \cdot \dfrac{\Delta\omega_B + \Delta\omega_A}{\omega_B - \omega_A}, \\ \delta\varphi_2 = \dfrac{\varphi_3}{2} \cdot \dfrac{\Delta\omega_B - \Delta\omega_A}{\omega_B - \omega_A} - \dfrac{\varphi_3}{2} \cdot \dfrac{(\Delta\omega_B + \Delta\omega_A)^2}{\omega_B - \omega_A}, \end{cases} . \tag{12}$$

where $\Delta\omega_A = \omega_A - \omega_1$ and $\Delta\omega_B = \omega_B - \omega_2$. If they are equal to zero, there is no phase distortion. Qualitatively, pure SOD distortions ($\delta\varphi_3$= 0) shift the two SHG peaks in the opposite directions and by the same amount $\Delta\omega_B = -\Delta\omega_A$. Pure TOD distortions move the peaks in the same direction.

As in the SOD measurements, RT-MIIPS TOD measurement is calibrated by running a linear chirp scan and recording the SHG spectra. The weighted SHG spectral peak positions as a function of chirp are then fitted with polynomials. The calibration data shown in Figure 7b, inset, corresponds to a linear chirp scan from -2,000 fs^2 to 2,000 fs^2. The reference phase parameters are: λ_0 = 1070 nm; $\Delta\lambda$ = 30 nm; $\varphi 3$ = 300,000 fs^3; and delay τ = 400 fs. The weighted SHG peak positions are fitted with third-order polynomials. The standard deviations for the measured SOD and TOD values are found to be about 100

fs^2 and 4000 fs^3, respectively. Again, the method proves to be more sensitive than measurements of integrated intensity.

2.1.3 Experiment

The experimental setup is shown schematically in Figure 8. The reflective pulse shaper is used to control phase and amplitude, and also to correct changes in phase and amplitude based on the closed-loop feedback. A small portion of laser beam from the laser output is split for monitoring the fundamental IR spectrum, and after frequency doubling in nonlinear crystal, for SHG spectrum acquisition (both by Ocean Optics USB4000 spectrometers). While this setup can be greatly simplified, we wanted the maximum flexibility for our first laboratory test.

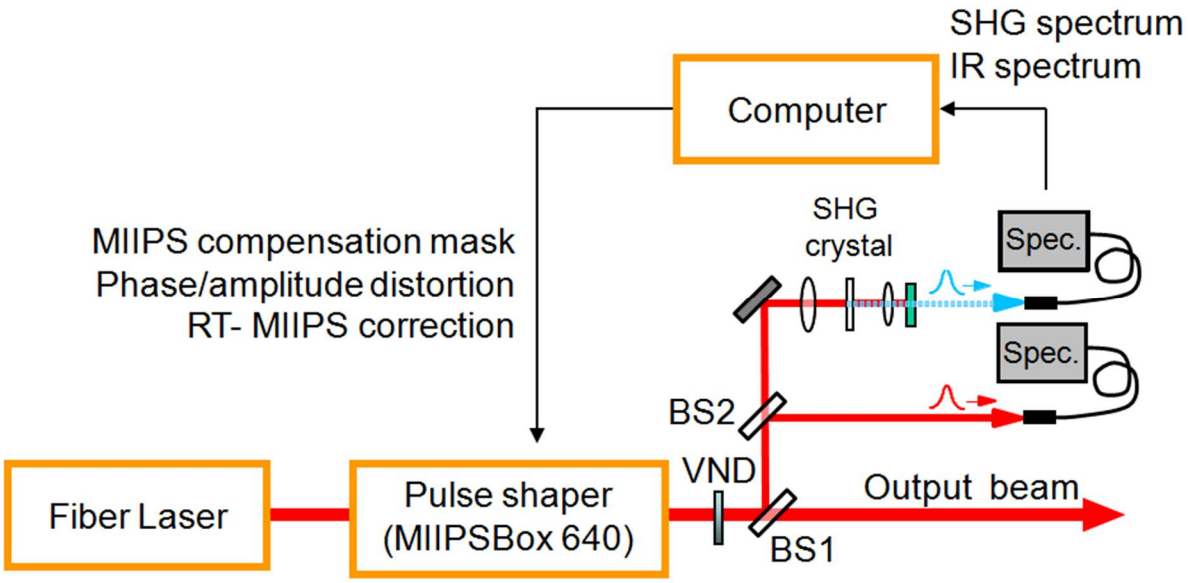

Figure 8. RT-MIIPS setup. VND, variable neutral density filter; BS1,2, beam splitters. Figure from [40].

To validate the performance of active phase monitoring and correction, we carried out several test experiments. In one of them we inserted in and out of the beam path a 30-mm thick piece of fused silica (Figure 9). Calculations based on the Sellmeier's equation give for fused silica 16 fs^2/mm of SOD at 1070 nm, i.e., about 480 fs^2 for the optic. The compensation routine measures it to be 450 ± 80 fs^2 (Figure 9a). As an indicator of pulse quality we use SHG signal intensity. All spectra were taken within a single data acquisition cycle. Each cycle took about 100 ms to complete, limited by the spatial light modulator

(SLM) response time. As expected, SHG signal drops when the fused silica sample is inserted due to group delay distortion (Figure 9b). When we activate the feedback loop, the pulse shaper applies a phase mask with a negative value to the measured SOD, thus recovering the original SHG intensity as shown in Figure 9c.

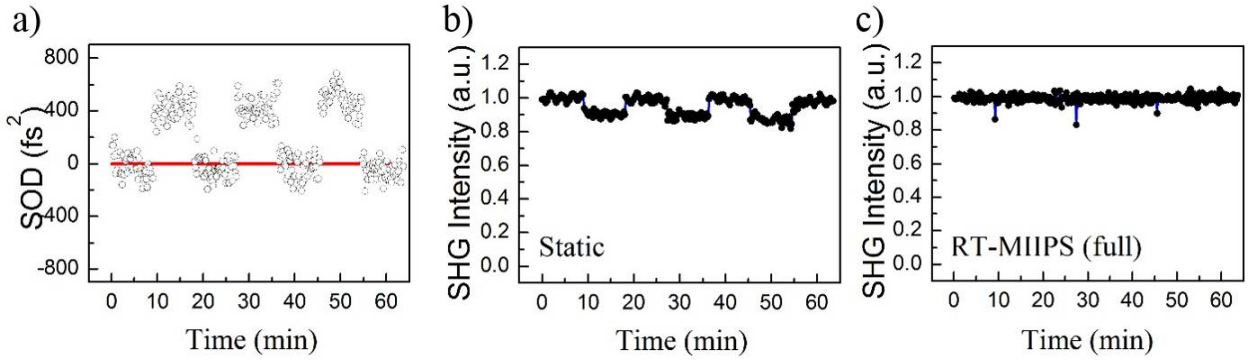

Figure 9. Validation of RT-MIIPS response to the insertion of a dispersive optical element. (a) SOD measured by RT-MIIPS. (b) Integrated SHG intensity (RT-MIIPS compensation off). (c) Integrated SHG intensity with RT-MIIPS compensation. All data are taken in the same acquisition cycle. Figure from [40].

The next comprehensive test applies well-characterized phase distortions – simultaneous sweeping of SOD and TOD, and amplitude attenuation performed by the pulse shaper. The functions for SOD, TOD and amplitude introduced are shown in the first column in Figure 10. The second column in Figure 10 shows the pulse energy, which varies as a function of the changes in amplitude introduced (Figure 10c). The peak power, monitored as integrated SHG intensity varies according to phase and amplitude as shown in Figure 10g. When the feedback loop is allowed to compensate for phase, there is a significant improvement in the integrated SHG intensity (Figure 10h). When phase and amplitude are corrected the SHG intensity remains stable despite the SOD, TOD and amplitude variations introduced. Note that given the measurement of sign and amplitude of SOD and TOD, there is no need for dithering and there is no evidence of overshooting in the closed-loop correction. The accuracy and stability of RT-MIIPS can be realized from close inspection of the first column in Figures 10a-10c, where the introduced phase and amplitude variations are shown as solid line and the experimental correction (with reverse sign) are shown as gray circles.

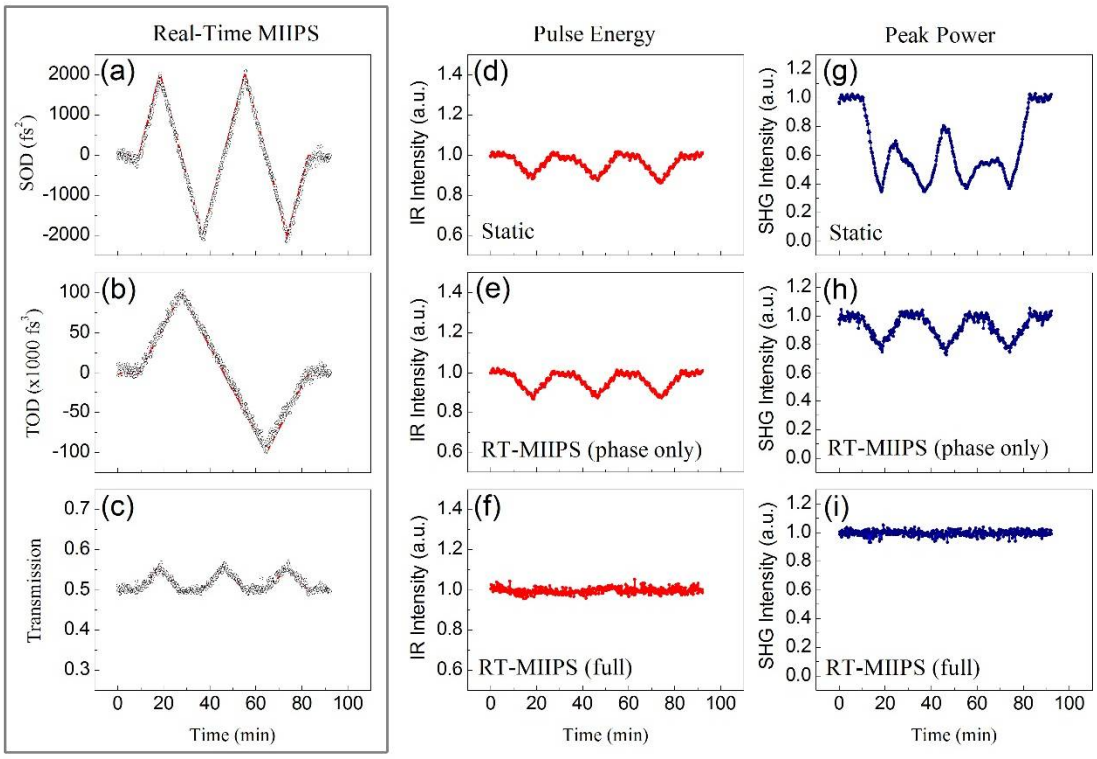

Figure 10. Validation of RT-MIIPS response to continuous sweeping of SOD, TOD and amplitude: (a) Measured SOD, swept by the shaper; (b) Measured TOD, swept by the shaper; (c) Applied transmission mask, swept by the shaper by as much as 10%; (d-f) Integrated IR spectra for (d) static phase compensation and transmission masks, (e) RT-MIIPS corrected phase and static transmission masks, and (f) RT-MIIPS corrected phase and transmission masks. (g-i) Integrated SHG spectra for (g) static phase compensation and transmission masks, (f) RT-MIIPS corrected phase and static transmission masks, and (i) RT-MIIPS corrected phase and transmission masks. Figure from [40].

In order to provide additional validation of the phase measurement and correction capabilities of RT-MIIPS, we present results for different laser systems. In the next experiment we have introduced phase distortion by adjusting the Ti:sapphire regenerative amplifier compressor (Spectra Physics), namely changing the distance between its gratings by means of built-in controllable linear stage. The detection setup is similar to Figure 8, and the pulse shaper is placed between oscillator and amplifier. Dispersion jumps were introduced for this case by changing the grating spacing in the compressor. The results from this run are presented in Figure 11.

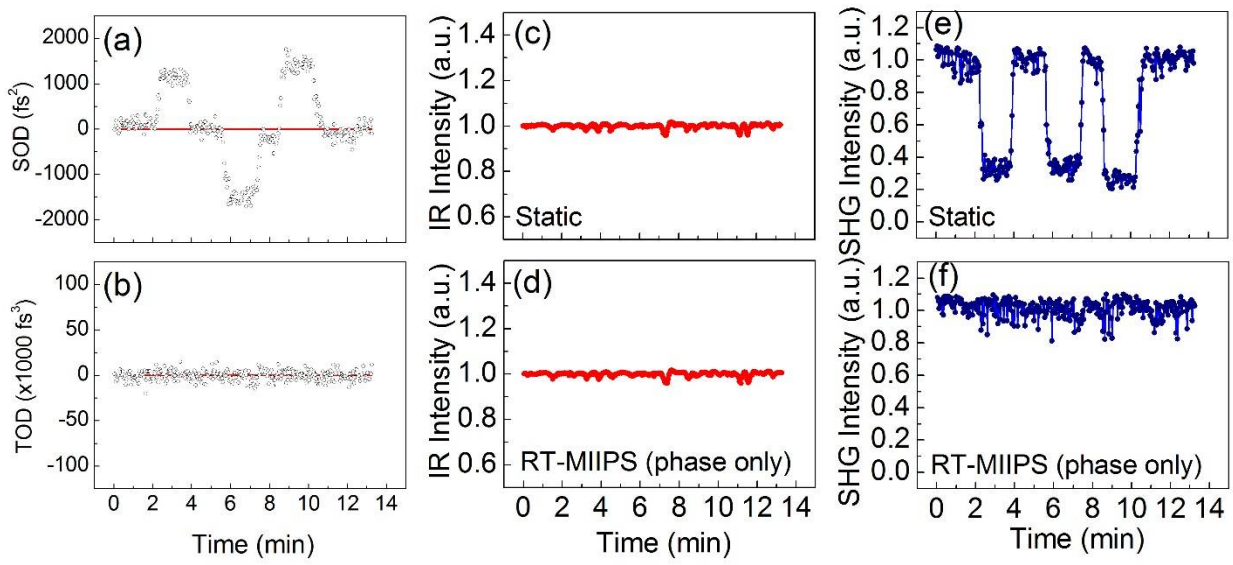

Figure 11. Validation of RT-MIIPS response to abrupt phase distortions introduced by the amplifier compressor: (a) Measured SOD drift; (b) Measured TOD drift; (c,d) Integrated IR spectra for static phase compensation and RT-MIIPS corrected phase, respectively; (e,f) Integrated SHG spectra for static phase compensation and RT-MIIPS corrected phase. Figure from [40].

For these experiments, RT-MIIPS measures changes in the phase (Figure 11a) which result in significant (70%) drop in peak power (Figure 11e), however, the pulse shaper automatically compensates the phase distortions and is able to maintain the peak power constant (Figure 11f). The fluctuations in peak power after compensation are inherent to the laser and are not caused by RT-MIIPS.

In general, RT-MIIPS measures any fluctuations of in the spectral phase including those intrinsic to the laser system. For the following experiments we used a regenerative amplifier system similar to the one used for the previous experiments but with a much more stable output (Micra Seed with Legend Amplifier, Coherent). We inserted four fused silica samples with different thickness in the laser path after the amplifier. The dispersion introduced by each sample was measured in 500 acquisition cycles. Each cycle took about 100 ms, the results are presented in Figure 12. The measurements turn out to be very precise with standard deviation within 4.2 fs^2. The accuracy is in a good agreement with theoretical values as show in Figure 12b.

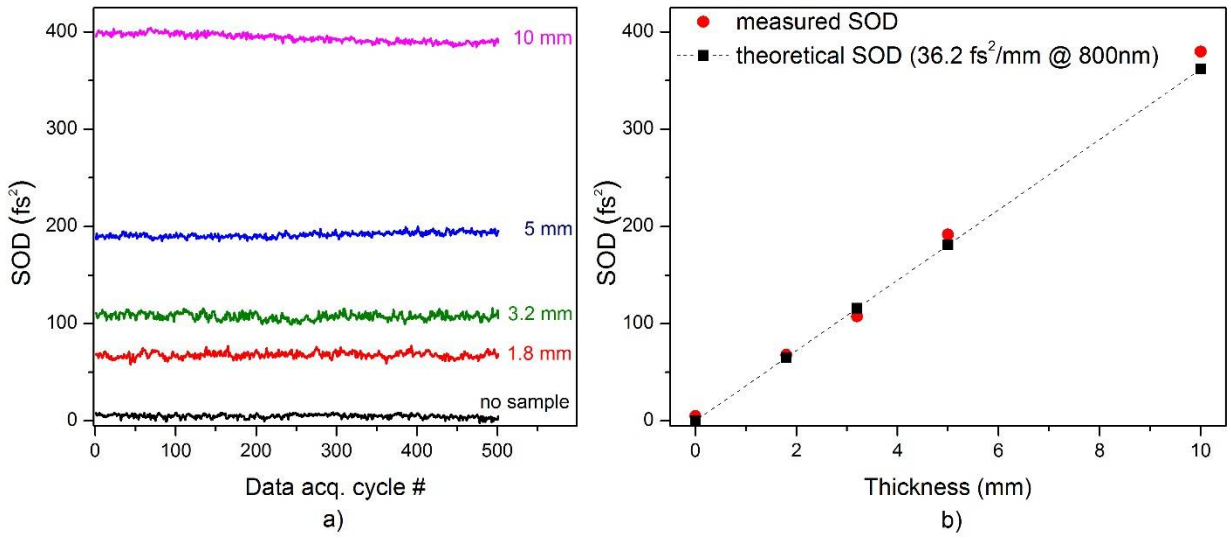

Figure 12. Chromatic dispersion measurements of fused silica: (a) Measured SOD as a function of time for 4 different samples – 1.8mm, 3.2 mm, 5 mm and 10 mm; (b) Measured SOD as a function of thickness. Squares represent calculated values of SOD for corresponding samples. Figure from [40].

2.1.4 Conclusion

To summarize, a method for real-time measurement and correction of amplitude as well as second and third order spectral phase distortions of ultrashort optical pulses has been demonstrated. The single-shot phase measurement exploits the well-understood dependence of the SHG spectrum on spectral phase. The current implementation is based on a programmable pulse shaper. It is worth noting that both measurement and compression can be achieved without a pulse shaper. The implementation of MIIPS by translating and tilting the grating in a compressor, shown by Hou et al. [46], could easily be part of the closed-loop approach demonstrated here. The encoding of the cubic reference phase can be achieved by using dielectric optics with desired characteristics or simply taking advantage of the cubic phase inherent to some optics like microscope objectives. The method shown here would be ideal for correction of phase and amplitude drifts in commercial laser systems (oscillators and amplifiers), to provide greater unassisted long-term performance. An application of RT-MIIPS being pursued in our laboratory, which takes advantage of its ability to measure laser-induced phase distortions, is time-domain pulse shaping which is described in next section [47].

2.2 Ultimate pulse shaping: controlling light with light

There are a several cases when the control of laser parameters via use of conventional optical schemes, such as grating and prism compressors or 4-f pulse shapers, is not feasible. The first reason is that these schemes are bulky and due to physical dimensions cannot fit into tight spaces like a laser cavity for need of intracavity dispersion control. The second reason is energy loss introduced by multiple optical components: a typical efficiency of a grating compressor is 70% and even lower for 4-f shaper. The third limitation is a wavelength range of laser pulses used: there are no gratings or SLMs designed for short (<400 nm) wavelength. The following work addresses these problems by use of an auxiliary laser pulse as a phase controlling mechanism.

In this project [47] we explored the ability of an intense pulse to control the dispersion experienced by a probe pulse taking advantage of the optical Kerr effect (OKE) and in particular what is known as cross-phase modulation [48]. Of particular interest is the spectral phase imprinted on the output pulses. One can envision a setup, such as that used in an enhancement cavity to create high harmonic generation [49], where part of the input laser could be used to control the intracavity dispersion and optimize the conversion efficiency. This approach is related to the proposal and eventual demonstration of phase modulation through the use of a pump pulse used to align molecules in the gas phase thereby causing a change in the refractive index, which in turn modulates the phase of a time delayed probe pulse [50, 51].

Measurements of laser-induced group delay dispersion (GDD) presented here are confirmed by two different experimental approaches and simulated through use of the OKE theory. In order to register single-shot time-resolved GDD measurements we used real-time multiphoton intrapulse interference phase scan (RT-MIIPS) [40], which is based on the predictable changes in the second harmonic spectrum of femtosecond lasers as a function of spectral phase [52]. The results obtained are validated by the Fourier-transform spectral interferometry (FTSI) method [53, 54]. Our measurements differ from traditional OKE measurements where the OKE phase shift [55, 56] or nonlinear absorption and refraction are obtained [57]. The spectral phase shift induced through the OKE is relatively small (less than 1 rad),

however, the GDD (second derivative of the phase with respect to frequency) is large enough to be useful for pulse compression.

2.2.1 Theory of laser induced phase manipulation

To illustrate the principle, we start with an intensity dependent correction to the refractive index of the media in time domain:

$$n(t) = n_0 + n_2 I(t) \tag{13}$$

where n_0 is the weak-field refractive index at carrier frequency, n_2 is the nonlinear refractive index of media, $I(t)$ is an intensity profile of the pulse, and higher order terms are neglected. If pump and probe pulses have mutually orthogonal polarization the probe beam experiences 2/3 of the nonlinear refractive index induced by the pump pulse [58]. This relationship is related to the cross-phase modulation phenomenon. The phase shift experienced by probe pulse in time domain is:

$$\Delta\phi(t) = -\frac{2}{3} \cdot n_2 I_{pump}(t) L \omega_0 / c \tag{14}$$

where ω_0 is the carrier frequency, L is the length of the medium, $I_{pump}(t)$ – intensity profile of pump pulse. The pump-induced phase change model is shown in Figure 13, where the probe pulse is illustrated by the black curve and the pump-induced phase distortion in the sample at different pump-probe delay times is depicted by a red curve. The function describing the phase distortion is broader since it depends on the crossing angle between the beams and dispersion of the medium. Note that the second derivative of the phase in the time domain has the opposite sign to that in the frequency domain [59].

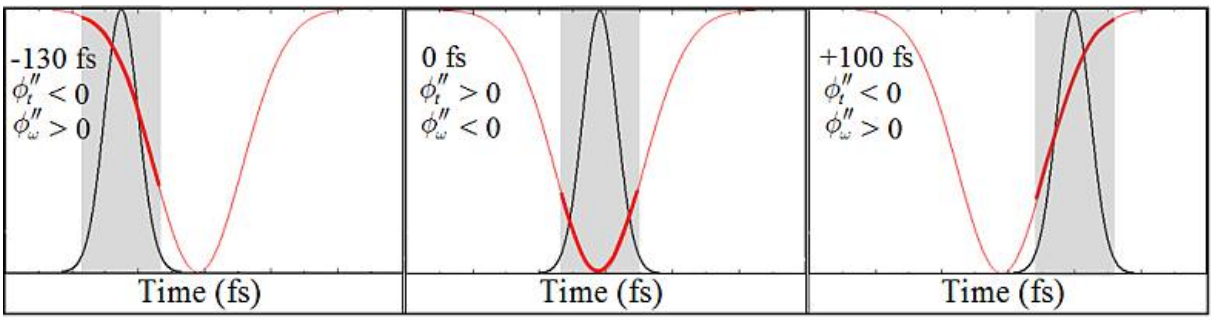

Figure 13. Schematic illustration of the OKE induced GDD (not in scale, pump peak intensity is a few orders of magnitude greater than probe) for three pump-probe relative positions at negative, 0 fs and positive time delays. Intensity profile of the probe pulse (black curve) moves along the OKE phase distortion function (red line). At different delay times the sign and magnitude of the GDD (φ_ω") changes. Figure from [47].

The electric field of the probe pulse at the exit of the sample is:

$$E(t) = E_0 e^{-t^2/2\tau_0^2} \times \exp[i\omega_0 t - i\left(n_0 + 2/3 * n_2 I_{pump} e^{-t^2/\tau_0^2}\right)\frac{L\omega_0}{c}], \tag{15}$$

where $E_0 = \sqrt{I_0}$, I_0 - intensity magnitude and τ_0 - full width at half maximum (FWHM) duration of a probe pulse, I_{pump} - intensity magnitude of a pump pulse. We used the first two terms of the Taylor expansion for the exponential function in the phase, and Fourier transformed it to the frequency domain to obtain GDD for small phase distortions, less than 1 radian:

$$\phi_\omega'' \approx \frac{2\tau_0^2 \cdot \phi_2}{1 + 4\phi_2^2}, \tag{16}$$

where $\phi_2 = -2/3 * n_2 I_{pump} L\omega_0 / c$ is a maximum of nonlinear phase shift.

2.2.2 Experimental setup

The pump-probe experimental setup is shown in Figure 14. The laser system comprises a Ti:sapphire oscillator (KMLabs), MIIPSBox640 pulse shaper (Biophotonic Solutions, Inc.) and regenerative amplifier (Spectra-Physics, Spitfire, 800 nm central wavelength, 1 kHz repetition rate). Pulses are compressed to their transform-limited duration of 40 fs by using the MIIPS technique [41]. The laser is split into two beams with orthogonal linear polarizations, denoted in the schematics as 'pump' and 'probe'. The probe beam is sent through a computer-controlled delay line. After passing through a

focusing lens the beams are overlapped at a 4° incidence angle on a 1.8 mm thick fused quartz sample placed a few centimeters away from the lens focus. The intensity of the pump beam on the sample is varied in a range of 0.3×10^{12} – 1.7×10^{12} W/cm^2 by adjusting a variable neutral density filter. The probe beam intensity is a few orders of magnitude lower than of the pump.

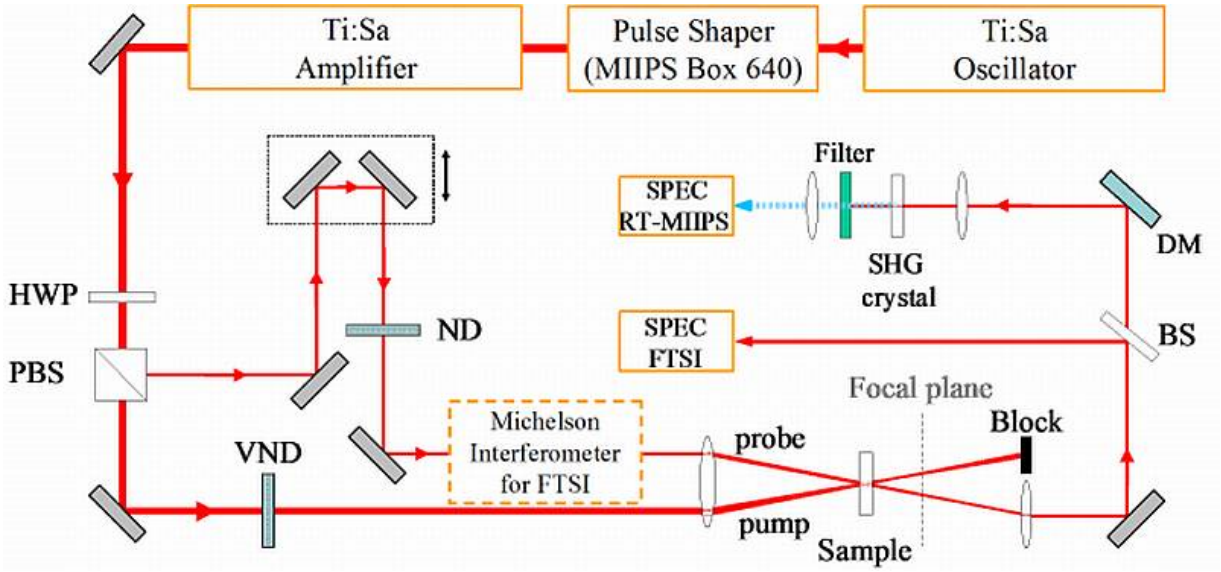

Figure 14. Experimental setup for transient dispersion measurements via RT-MIIPS and FTSI methods. The Michelson interferometer is used only for FTSI. HWP, half-wave plate; PBS, polarizing beam splitter; VND, variable neutral density filter, ND, neutral density filter, DM, dielectric mirrors. Figure from [47].

For the RT-MIIPS calibration and measurements [40], the probe beam after the sample is guided through a set of dielectric mirrors which introduce a static spectral phase distortion dominated by the third-order dispersion (TOD) of -150,000 fs^3. The conditioned probe beam is then focused on a second harmonic generation (SHG) crystal and the SHG spectrum is recorded with a fiber-coupled compact spectrometer (Ocean Optics HR4000). There is no contribution into SHG from the stray pump light because pump and probe have perpendicular polarization. For the RT-MIIPS calibration process we apply the procedure using only the probe beam through the sample. For pump-probe measurements, the pump beam is unblocked and the SHG spectrum is acquired for each pump-probe delay position.

For FTSI measurements, a Michelson interferometer is used to make two replicas of the probe pulse with 1 ps time separation. The pump pulse arrives at the sample after the first reference probe

replica so that the pump-induced changes affect only the second replica. These distortions lead to a phase change between the two replicas. The spectral interferometry signal collected by a spectrometer (Ocean Optics QE65000) bears these changes. The GDD values for each pump-probe delay position are extracted by Fourier transformation and polynomial fitting of the retrieved phase.

2.2.3 Results and discussion

RT-MIIPS measures the second derivative of spectral phase directly. The raw experimental data is a 2D spectrogram of SHG signal as a function of the pump-probe delay [40]. For each single SHG spectrum from this spectrogram a position of the maximum is calculated. Through one-to-one correspondence between SHG peak position and second derivative of spectral phase GDD can be extracted. The corresponding induced GDD values experienced by the probe pulse at each time delay value are plotted as a function of delay time in Figures 15-17.

Experimental results in Figure 15 show negative GDD around zero delay time with the minimum value of -139 fs^2. There is a subsequent rise of GDD at about 100 fs delay time with the maximum of +70 fs^2. This data were obtained with the pump peak intensity of 0.68×10^{12} W/cm^2. The FTSI measurements (see the blue squares in Figure 15 closely reproduce the RT-MIIPS results in shape and magnitude. The FTSI curve (red circles) was shifted vertically by 10 fs^2 during the data processing. The observed non-zero GDD offset originates from the unbalanced Michelson interferometer. The accuracy of the GDD measurements is within $\pm20fs^2$; determined during the calibration procedure using a calibrated pulse shaper [40].

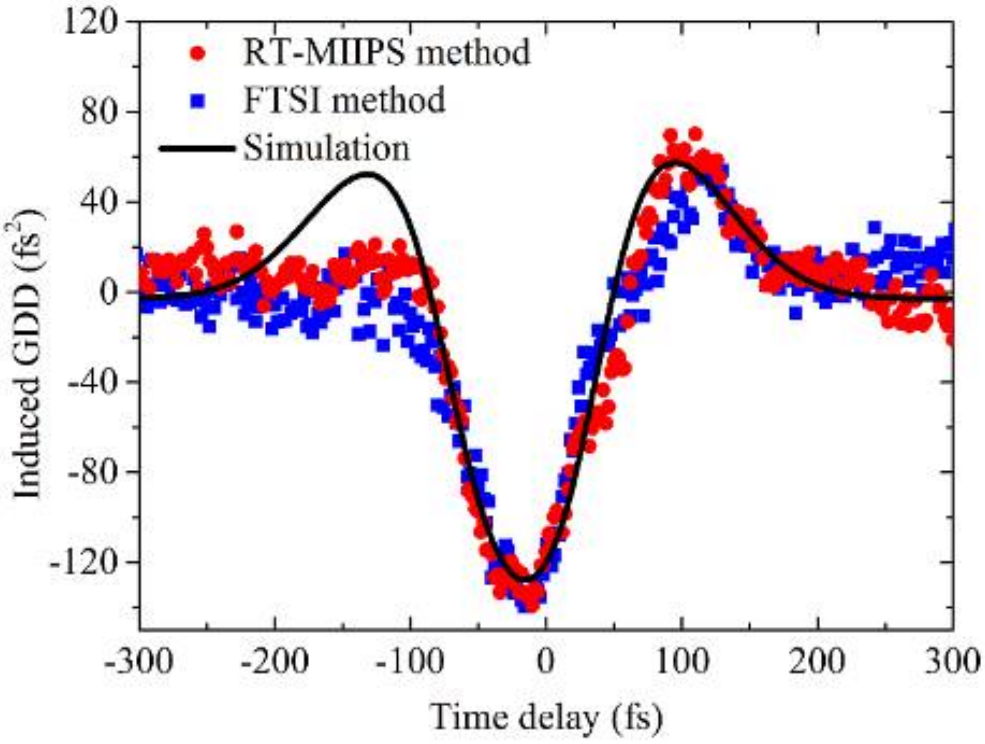

Figure 15. Experimental measurement and simulation of laser induced GDD acquired by the probe pulse with respect to pump-probe delay time. Red and blue curves are experimental data from RT-MIIPS and FTSI methods, respectively. Black solid curve is the result of OKE simulation model. Figure from [47].

The theoretical curve showed in Figure 15(black solid line) is a result of numerical simulation based on Fourier transformation of Equation 15. We assumed a Gaussian profile for the pump-induced phase with FWHM of 148 fs. The majority of the pulse broadening is caused by the crossing angle between the pulses. The asymmetric shape of the experimental GDD profile is caused by the optical response of the media through SPM [60] and the nuclear response [61]. To reach quantitative agreement between model and experiment we introduce a 1.85/3 factor for the nonlinear phase shift. This value is reasonably close to the theoretically expected value 2/3 [58]. The mismatch between theoretical and experimental values is likely from the cumulative uncertainty on the intensity measurements which depend on average power, pulse duration and beam size.

Figures 16 and 17 show the dependence of pump-induced GDD with respect to peak intensity and initial chirp value correspondingly. From Figure 16 it follows that as the intensity of the pump laser increases the GDD magnitude increases in both negative and positive GDD regions. In case of red curve

(squares) the GDD has it minimum -232 fs^2 and maximum +502 fs^2, values which are several times the corresponding GDD of fused silica with the same 1.8 mm thickness 65.16 fs^2.

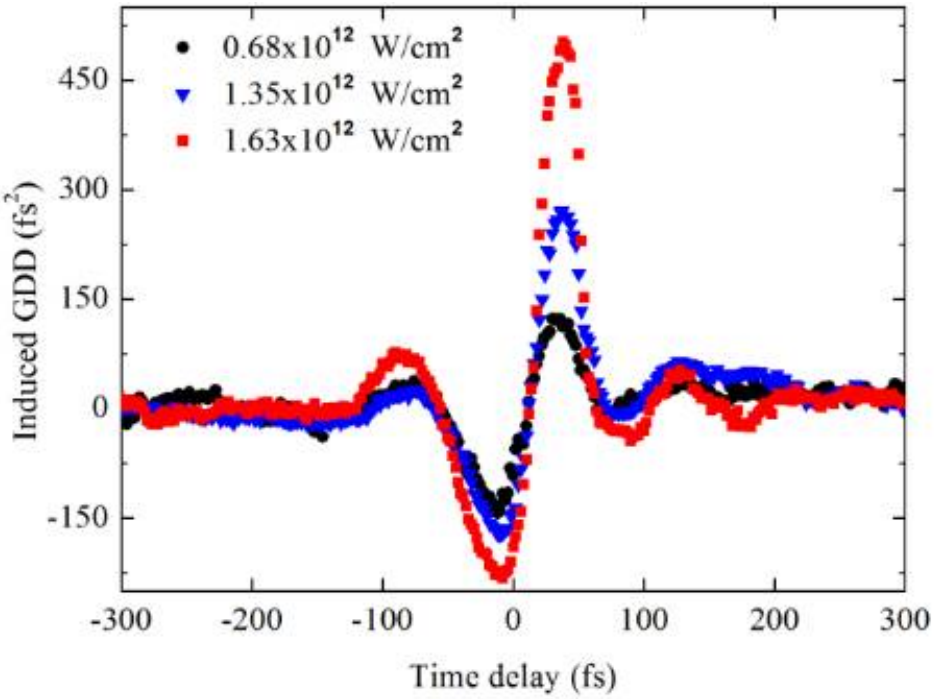

Figure 16. Group delay dispersion as a function of pump-probe delay time for different values of a pump peak intensity: 0.68×10^{12} W/cm^2, 1.35×10^{12} W/cm^2, 1.63×10^{12} W/cm^2. Figure from [47].

The observed oscillations (Figure 16, red squares) for positive pump-probe delay times are similar to those reported in fused silica when looking at Kerr gate signals [61] which assigns the oscillations to the nuclear contribution (phonons) to the signal. Figure 17 shows the dependence between induced GDD and initial chirp value. The green dots in Figure 17 indicate the time delays where total GDD is zero, meaning that the induced GDD cancels the chirp of the input probe pulse and therefore compresses it to TL duration. Figure 17 has evidence of the two-beam coupling process [62]. The energy transfer between pump and probe [63] beams is proven by the asymmetric shape of red (squares) and blue (triangles) curves in Figure 17. Changes in the overall width in the different measurements shown in Figures 15-17, is caused by changes in the crossing angle between pump and probe pulses. Narrower widths require near collinear geometry.

Nonlinear optical dispersion experienced by a single beam, and as acquired by a pulse when overlapped in time by another pulse results in spectral phase that to first approximation corresponds to either positive or negative chirp.

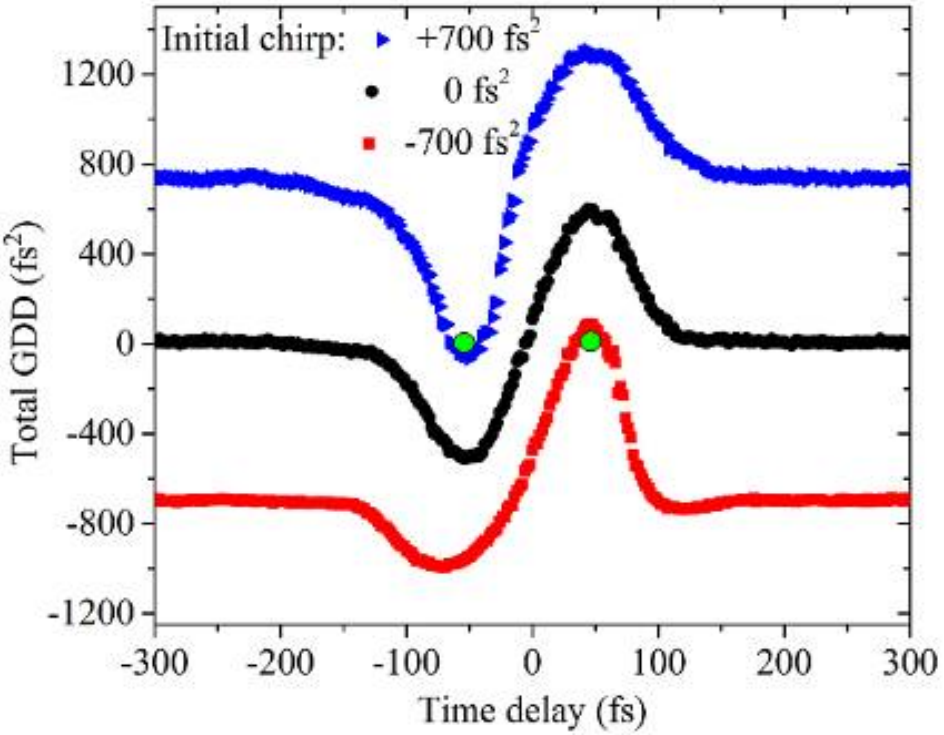

Figure 17. Group delay dispersion as a function of pump-probe delay time for different values of initial chirp. Black circles for 1.7×10^{12} W/cm^2, red squares and blue triangles for 1.15×10^{12} W/cm^2. Figure from [47].

2.2.4 Conclusion

The measurements presented in this work are relevant to pump-probe experiments carried out in fused silica cuvettes; femtosecond laser sources involving supercontinuum generation contained in hollow waveguides [64, 65]; ultrafast fiber lasers which combine high peak intensity and long propagation length; and silicon-based high-speed on-chip devices [66]. Finally, it has become of interest to use enhancement cavities to create high harmonic generation. The efficiency of such cavities depends on intracavity dispersion, which is managed through the use of chirped mirrors and prisms. While the inclusion of an intracavity bimorph deformable mirror together with a prism pair could be used to control the intracavity dispersion [67], one could consider using the concept described here, taking advantage of the interaction between two pulses in a nonlinear medium, to control intracavity dispersion.

The laser-induced GDD acquired by a probe pulse in fused silica as a result of interaction with an intense pump laser through changes in the refractive index of media has been measured. The GDD can be tuned in the range of hundreds of fs^2, both negative and positive, by changing a time delay between pulses. The induced GDD magnitude and sign depends not only on the intensity of the pump pulse but also on the initial chirp. A numerical model based on the optical Kerr effect is used to provide a theoretical foundation for the experimental results. The findings could be used to design a pulse shaping method which exploits the nonlinear interaction between strong and weak laser pulses inside a Kerr medium to control the temporal profile of the weak pulse through cross-phase modulation. This type of phase control could be important in enhancement cavities being used for producing higher harmonics or in a cavity where the space appears to be a limiting factor and other stretcher/compressor devices would not be suitable to use.

Chapter 3 Laser self-action

This chapter focuses on the propagation of an intense laser pulse in an optical medium. In addition to a chromatic dispersion, which is applicable to pulses with any intensity propagating in dispersive media, an intensity induced dispersion, driven by the term $n_2 I(t)$ in Equation 13, starts to play a significant role. The effect of chromatic dispersion is easily predicted and calculated from Equation 6 when a material and its length are known. For intensity induced dispersion, the changes in pulse parameters are often more severe and have non-linear dependence, therefore require careful measurement and correction. We study the effect of intensity-induced dispersion in fused silica, one of the most common materials for optical elements, chamber windows and cuvettes used in spectroscopic experiments. The experimental results are presented and discussed in the first section of this chapter. The second section illustrates a method of mitigation intensity induced pulse changes by applying a binary spectral phase on a laser pulse prior its interaction with a medium. Same mask applied after the interaction can reverse changes induced by the first mask and the shape of pulses is restored, free from intensity induced dispersion.

3.1 Laser-induced dispersion in fused silica

To first approximation, propagation of femtosecond lasers in transparent media leads to pulse broadening due to dispersion. For visible and near-IR wavelengths pulses experience positive group delay dispersion that is proportional to the length of the medium (see Equation 6). Since the early days of ultrafast lasers the static or intensity independent group velocity dispersion values for common optical materials were tabulated and methods were introduced to compensate the dispersion at least to second and third order. Laser induced changes to the refractive properties of the medium resulting in frequency broadening were first observed 55 years ago [68]. However, despite all the progress in nonlinear optics during the past decades, one can still expect to find surprising phenomena, especially as ultrashort femtosecond pulses with dispersion control to third-, fourth-, and even higher-orders become widely available.

When a high intensity laser pulse enters a dielectric medium, it perturbs the medium, causing nonlinear changes of the index of refraction leading to the free carrier excitation [69-72], and defect generation [73, 74]. These changes in turn affect the pulse characteristics as discussed in pulse steepening [72]. Peak intensities of the order of 10^{11} W/cm^2 are below the threshold for supercontinuum generation, but are high enough to induce optical Kerr effects in fused silica [75]. Kerr effects produce an intensity-dependent refractive index change (see Equation 13), which has been measured with high sensitivity and time resolution in a number of media [57, 76, 77]. Changes in the refractive index give rise to self-phase modulation (SPM). SPM causes frequency chirp and the generation of additional frequency components. It has been suggested that gas-phase molecular dynamics can lead to deterministic changes in the refractive index of the medium, as demonstrated experimentally by taking advantage of anomalous GDD associated with a rotational wave packet to compress laser pulses [50]. Soliton pulse compression, associated with self-compressed optical filaments caused by SPM have been observed and associated with the gas-glass-gas interfaces [78].

In general SPM affects femtosecond laser performance. In femtosecond lasers, nonlinear propagation effects such as SPM are therefore mitigated by temporal stretching of the pulses, as in chirped pulse amplification, or spatially expanding the laser beam, as in large mode area fibers. In ultrafast fiber laser design, high-energy pulses can accumulate a non-linear phase, causing wave-breaking and temporal profile changes of the output pulses [79]. Despite nonlinearity mitigating approaches, day-to-day variations in the performance of femtosecond lasers are quite common. It is therefore of fundamental importance to search for and quantify directly laser induced GVD and to provide a physical understanding that can be used for designing and modeling ultrafast lasers and devices. Our ability to measure and control spectral phase changes caused by nonlinear propagation in the spectral domain with high sensitivity [52], provides a new window into nonlinear optical processes. In this experiment, we took a closer look at the second derivative of the spectral phase or GDD acquired by high peak-intensity laser pulses during propagation in fused silica. We explored transform limited pulses and pulses for which a positive or negative pre-chirp is impressed before propagation in fused silica [30].

3.1.1 Experimental setup

A schematic of the experimental setup is presented in Figure 18. The output from a Ti:sapphire oscillator (Coherent Inc.) passes through a pulse shaper (FemtoFit, BioPhotonic Solutions, Inc.) and a regenerative amplifier (800 nm central wavelength, 1 kHz rep. rate, Legend, Coherent Inc.) and, after attenuation, is focused with a long focal length lens (f = 300 mm). The laser pulses are first characterized and high-order dispersion is eliminated to better than fifth order at the sample by using multiphoton intrapulse interference phase scan [52]. The initial chirp of the pulse is controlled by the same pulse shaper. The transform limited pulse duration at full-width half-maximum is 40 fs. For all the measurements presented here the average power is set to 10 mW; low enough to prevent unwanted nonlinear processes away from the sample. The sample, a 1 mm plate of fused silica, is placed on a translation stage. The peak intensity was varied by scanning the sample position along the converging laser beam (from 56 to 8mm from the focal plane), in a manner similar to a Z-scan [57], however the sample is not scanned through the focus. The focusing beam characteristics were measured using a beam profiler (LaserCam-HR, Coherent Inc.).

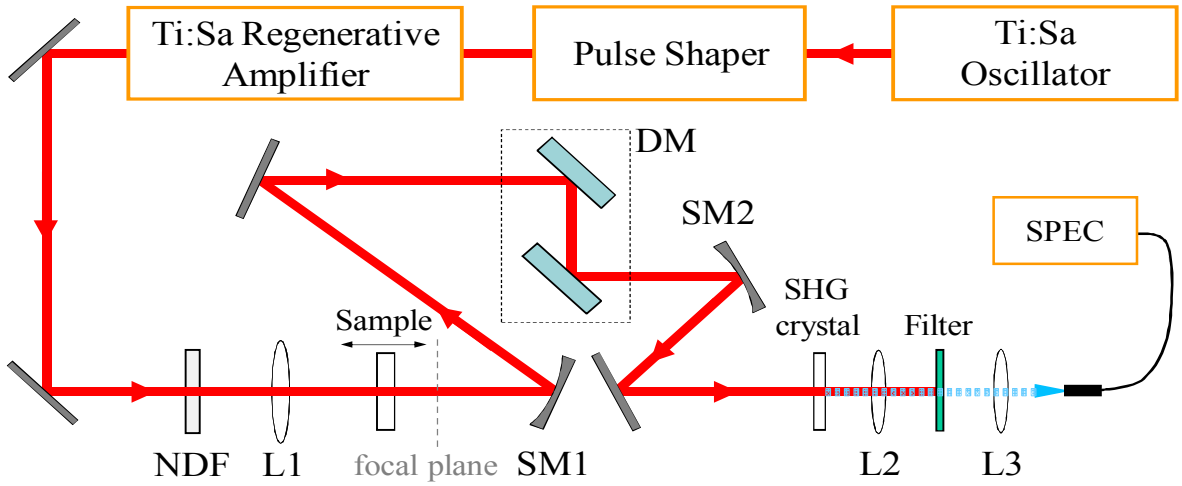

Figure 18. Experimental setup for direct GDD measurements. NDF, neutral density filter; L1,2,3, lenses; SM1, 2, spherical mirrors; DM, chirped dielectric mirrors; SPEC, spectrometer. Figure from [30].

The laser beam, collimated after the sample, is guided through a pair of chirped dielectric mirrors which introduce significant -1×10^5 fs^3 third-order spectral phase. After focusing on a 0.1-mm-thick BBO

crystal the second harmonic generation signal is recorded with a fiber-coupled compact spectrometer (Ocean Optics, HR4000). The SHG crystal is set far from the focal plane to avoid unwanted nonlinear processes and minimize beam profile effects. Reflective optics between the sample and the SHG crystal minimize spectral phase distortions.

For fused silica at 800nm, the GVD is equal to 36.2 fs^2/mm. Third order dispersion, from the dielectric a mirrors, causes a narrowing of the SHG spectrum due to nonlinear optical interference, as discussed in terms of multiphoton intrapulse interference [41]. When GDD is added to a pulse with third-order spectral phase, the peak SHG wavelength shifts [41]. Here, GDD was measured by tracking the wavelength shift as shown in Figure 19. The spectrometer resolution 0.12 nm was improved by using a Gaussian fit of the experimental spectra to determine the peak position, thus achieving ± 5 fs^2 precision. A calibration curve was made by scanning a known value of GDD using the interferometrically calibrated pulse shaper. Measuring GDD by tracking the spectral shift provides single-shot high-accuracy values ($\pm$ 20 fs^2), without the need for phase retrieval algorithms. We further tested the absolute accuracy by measuring the dispersion from different thicknesses of fused silica; fitting the obtained values resulted in a slope of 37.6fs^2, which is off by 1.4 fs^2 from the literature value. All measurements presented in this paper were obtained using RT-MIIPS method [80], discussed in Chapter 2. A typical GDD measurement as a function of peak intensity involved 2500 measurements which were completed in less than 5 minutes.

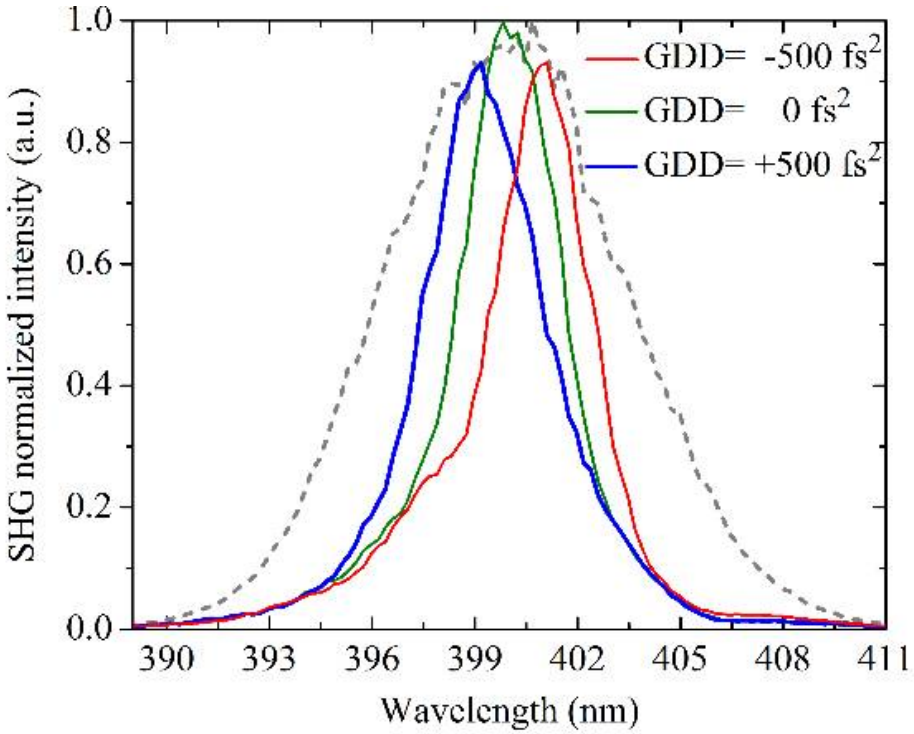

Figure 19. RT-MIIPS principle. Experimental SHG spectra for different GDD values. The SHG spectrum for transform limited pulse is shown as a dotted line for reference. Cubic spectral phase causes SHG spectral narrowing (green). The SHG peak value shifts towards longer (shorter) wavelengths in the presence of negative (positive) GDD, respectively. Figure from [30].

3.1.2 Results and discussion

The peak intensities, measured before the sample, ranging from 0.5×10^{11} W/cm^2 to 5.8×10^{11} W/cm^2, cover an important region where spectral changes occurring through SPM are small. Measured GDD values for a 1 mm fused silica plate as a function of peak intensity for five different pre-chirp conditions are presented in Figure 20a. The dispersion length L_D of fused silica is ~44 mm, and the nonlinear length L_{NL} is ~1 mm. Therefore, no significant dispersion or nonlinear phase shift from propagation through the sample are expected. Our measurements, however, indicate GDD changes are very significant despite the fact that the spectrum of the laser before and after the sample for intensities below 4×10^{11} W/cm^2 shows no difference or shift, for higher intensities one can notice ~5% wings resulting from SPM.

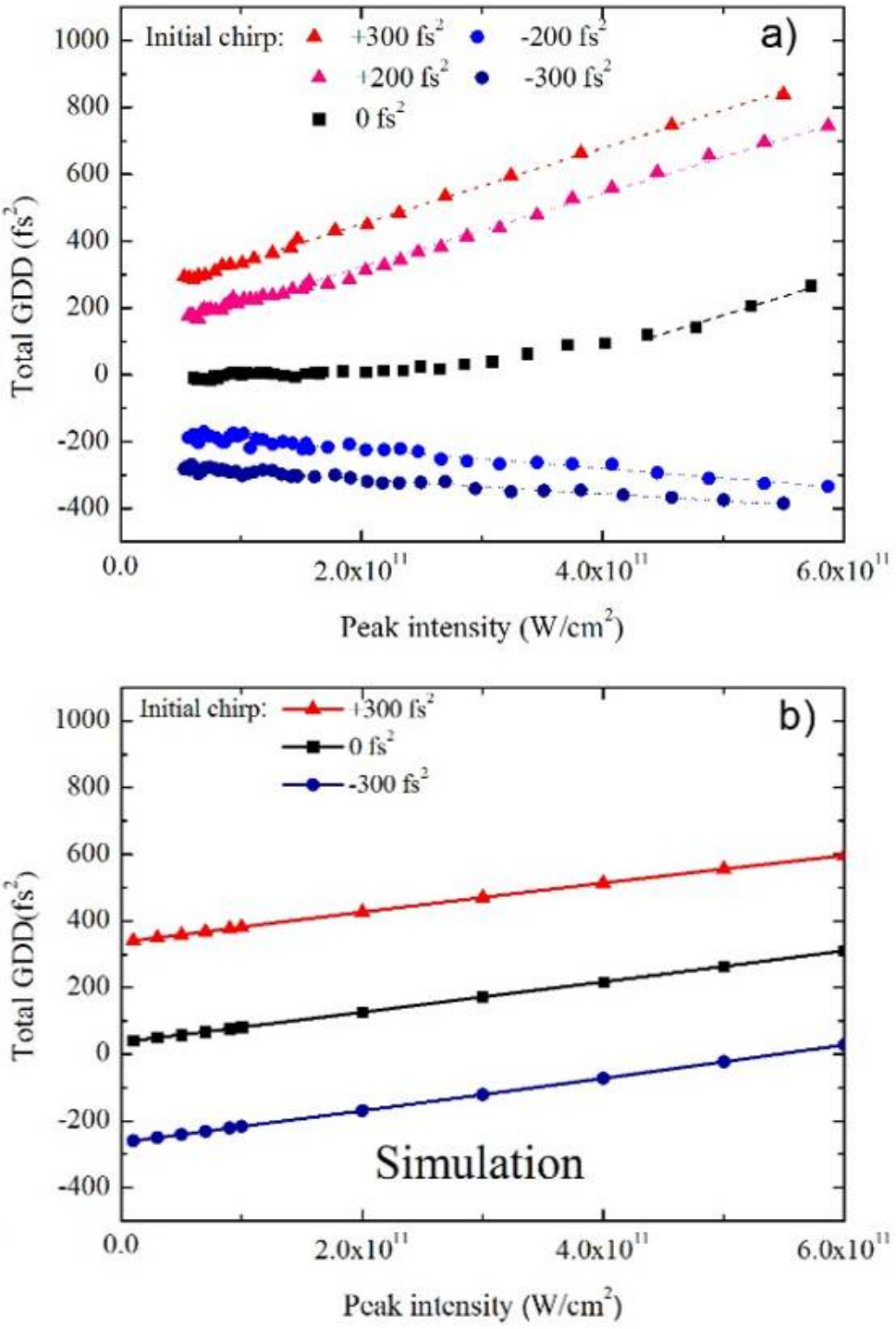

Figure 20. Group delay dispersion as a function of peak intensity after propagation through 1 mm of fused silica. (a) Experimental measurements. The applied initial pre-chirps are +300 fs^2 (red triangles), +200 fs^2 (pink triangles), 0 fs^2 (black squares), -200 fs^2 (blue circles), and -300 fs^2 (dark blue circles). Dotted lines are corresponding linear fits. (b) Numerical, split-step Fourier transform, simulation without adjusting parameters. Initial pre-chirps are +300 fs^2 (red triangles), 0 fs^2 (black squares), -300 fs^2 (dark blue circles). Figure from [30].

The most interesting observation in Figure 20a is that the induced dispersion has a different sign depending on the initial chirp impressed on the input pulses. We define induced GDD as the measured GDD minus the initial chirp and static dispersion from the material. Positive pre-chirped pulses acquire normal induced GDD that is linear with peak intensity. Induced GDD measured at 5.5×10^{11} W/cm^2 is about 550 fs^2 and can be understood in terms of SPM. Induced GDD for the TL pulses increases slowly up to 4.5×10^{11} W/cm^2 followed later by a linear dependence. At an intensity of 5.8×10^{11} W/cm^2 the induced GDD for transform limited pulses reaches 270 fs^2. The dependence at lower intensities does not show a linear behavior, but the region from 4.5×10^{11} W/cm^2 to 5.8×10^{11} W/cm^2 can be fitted by a line (black dashed line in Figure 20a) with a slope close to the slope that is observed for the positively pre-chirped pulses. The measurements with transform limited pulses appear to involve an intensity threshold before laser-induced GVD (LI-GVD) takes place. For negatively pre-chirped pulses an unexpected behavior is observed. Induced GDD is found to have a negative slope (blue dashed line in Figure 20a) and continues to accumulate anomalous induced GVD, reaching a value of -120 fs^2 for 5.5×10^{11} W/cm^2. Effective nonlinear n_2 coefficients are obtained based on fitting the slope of the experimental data, and using the approximate relation:

$$n_2^{eff} = \frac{GDD_{IND} \cdot c}{2\tau_0^2 \omega_0 L \cdot I_{PEAK}}, \tag{20}$$

where the induced GDD_{IND} is divided by the pulse duration τ_0 FWHM, the angular frequency ω_0, the length of the propagation L and the peak intensity I_{PEAK}. The effective n_2 for positive and zero chirp is $n_2^{eff} \approx (1.2\pm0.1)\times10^{-16}$ cm^2/W, which is close to the published n_2 for fused silica $(2.48\pm0.23)\times10^{-16}$ cm^2/W, measured with 100 fs pulses at 804 nm [81]. For negatively pre-chirped pulses the nonlinear refractive indices are negative. To our knowledge, anomalous laser-induced GVD has not been observed before. Our measurements starting below 10^{11} W/cm^2 reveal a linear behavior observed up to 6×10^{11} W/cm^2. The linear trend for normal and anomalous LI-GVD implies that free-carriers are not likely involved at these intensities.

We have carried out split-step Fourier transform numerical calculations to simulate our data [82]. Results for three initial chirp conditions are show in Figure 20b. Our simulations, without adjustable parameters, agree with the findings for positive pre-chirp and those for TL pulses. The difference in the value of the slope is likely due to the intensity distribution of the laser in the experiment and in the calculations. However, the calculations do not agree with the experimental findings for negatively pre-chirped pulses. The observation of anomalous dispersion associated with negative pre-chirp requires us to consider a different nonlinear process. Smolorz et al. considered two-beam coupling for chirped pulses [62], and indicate energy is transferred from high-frequency to low frequency components during the interaction. Energy transfer depends on phase matching and depends on the relative time delay between the chirped pulses. The relevance of beam coupling to our single-beam experiment is that only a negatively chirped pulse can experience energy transfer caused by the non-instantaneous response of the medium, from high-frequencies to low frequencies. This energy transfer may be responsible for the observed anomalous LI-GVD. At higher intensities, once significant SPM related spectral broadening is observed (data not shown), the anomalous LI-GVD trend is reversed.

3.1.3. Conclusion

The laser-induced group velocity dispersion in fused silica has been measured with high accuracy in a regime that is near the transform limit. The experiments were conducted using a direct single-shot measurement of dispersion. It has been shown that LI-GVD depends linearly on the peak power of the laser and it can be in excess of one order of magnitude the static GVD of the material. Most significantly, anomalous LI-GVD is observed when the input pulses are negatively pre-chirped. Normal laser induced dispersion can be understood in terms of self-phase modulation, however, anomalous LI-GVD cannot. The anomalous LI-GVD is speculated to be caused by energy transfer from higher to lower frequencies. The findings could have important implications for femtosecond laser design and compression, as well as for ultrafast laser science where knowledge of the exact value of frequency chirp is required.

3.2 Mitigation of self-action by binary phase shaping

Self-action mitigation requires a decrease in the laser peak power to a level where induced nonlinearities have no "visible" effect. Such methods include temporal stretching of pulses as in chirp pulse amplification (CPA) systems [83], splitting the pulse into a train of pulses as in divided-pulse amplification [84], and increasing mode area [85]. In general, Ti:Sapphire pulsed laser systems, such as CPA-based systems, stretch the pulses up to four orders of magnitude by introducing chirp. An alternative method is to introduce cascaded nonlinearities in a cavity for the compensation of laser-induced phase shift in a medium [86, 87]. The difficulty of this method is that it depends on the nonlinearity of the nonlinear crystal, and the amplification gain is orders of magnitude less than in CPA systems [87]. Divided pulse amplification and mode area increases can reduce peak intensity by at most two orders of magnitude.

In this project [88] we use a binary phase mask composed of either zeros or π at the Fourier plane of a 4-f shaper [89-91]. The idea of using binary phase shaping (BPS) comes from experiments where it was shown that BPS provides a robust mitigation of nonlinear optical processes [92] and the symmetry of the phase can be used to cause selective nonlinear excitation [93, 94]. BPS has been used to control multiphoton excitation induced chemical reactions [95], and for achieving vibrational mode selectivity in coherent anti-Stokes Raman scattering (CARS) spectroscopy [96]. Binary phase shaping causes a femtosecond pulse to break into a train of pulses with overall longer duration and lower peak power. It has been shown to increase the transmission distance of laser pulses in an optical fiber [97].

Pastirk et al. showed that a binary phase introduced prior to amplification can be compensated afterwards [98]. This concept and its possible applications are illustrated in Figure 21. We show (a) that a pulse can be stretched in the time domain by a binary phase, then amplified and recompressed by addition of the same binary phase [98]. This fact makes BPS attractive for optical amplification (b) and laser endoscopy (c). To use this template, you will need to apply the embedded styles to each paragraph-level item in your manuscript, or simply use this template as a visual guide.

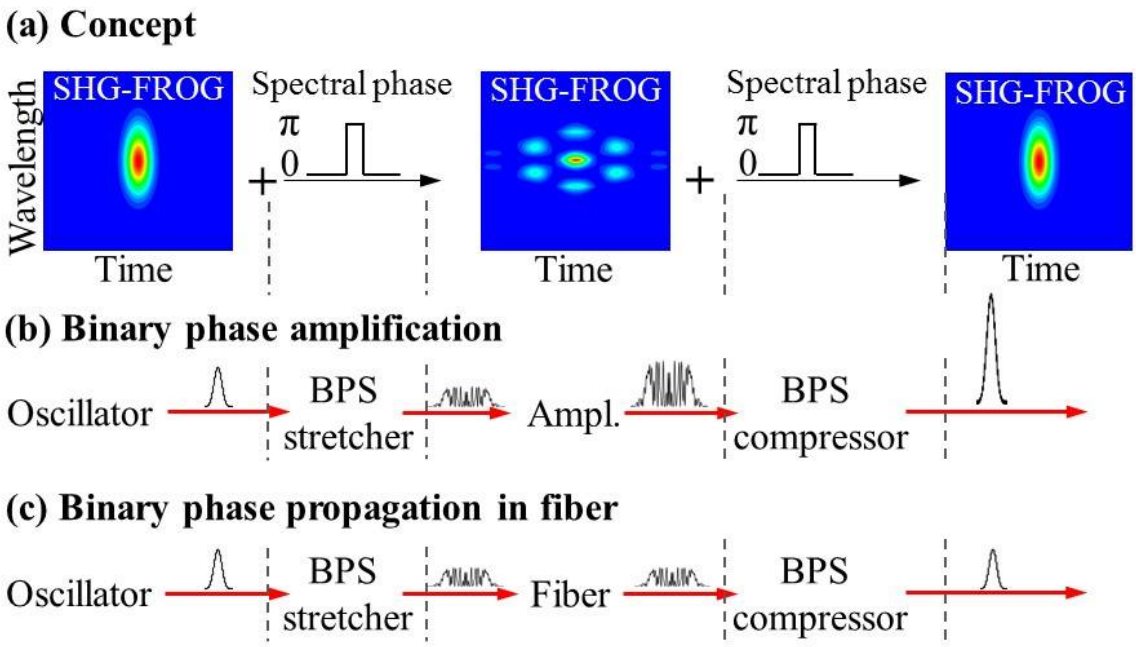

Figure 21. (a) The concept of using BPS in (b) optical amplification systems and (c) fiber lasers. Figure from [88].

3.3.1 Numerical simulations and experimental results

We conducted experiments and numerical simulations on how BPS affects temporal pulse shape. For both experiments and simulations we used the fundamental laser spectrum of a Ti:sapphire amplifier with 40fs pulse duration (τ0), see Figure 22a. The spectrum is spread over 600 pixels of spatial light modulator (SLM), as it is in our experiment (explained further). We introduce the term 'bit', which stands for the partition number. Since the spectrum covers 600 pixels, it corresponds to the maximum number of 1-pixel bits. In Figure 22a we show the fundamental spectrum and the optimum 14-bit (600/14≈42 pixels per bit) binary phase out of 16,384 phases to achieve more than an order of magnitude peak intensity reduction in the time domain. To calculate the pulse shape in the time domain we used the Fourier transform:

$$I(t) = \left(\int \sqrt{I(\omega)} e^{i\varphi(\omega)} e^{-i\omega t} d\omega \right)^2, \tag{21}$$

where I(ω) is the pulse spectrum (red curve in Figure 22a), and φ(ω) is the binary spectral phase (black curve in Figure 22a). Figure 22b compares the time profiles of a transform limited pulse, periodic zero/ π and the optimal phase (shown in Figure 22a).

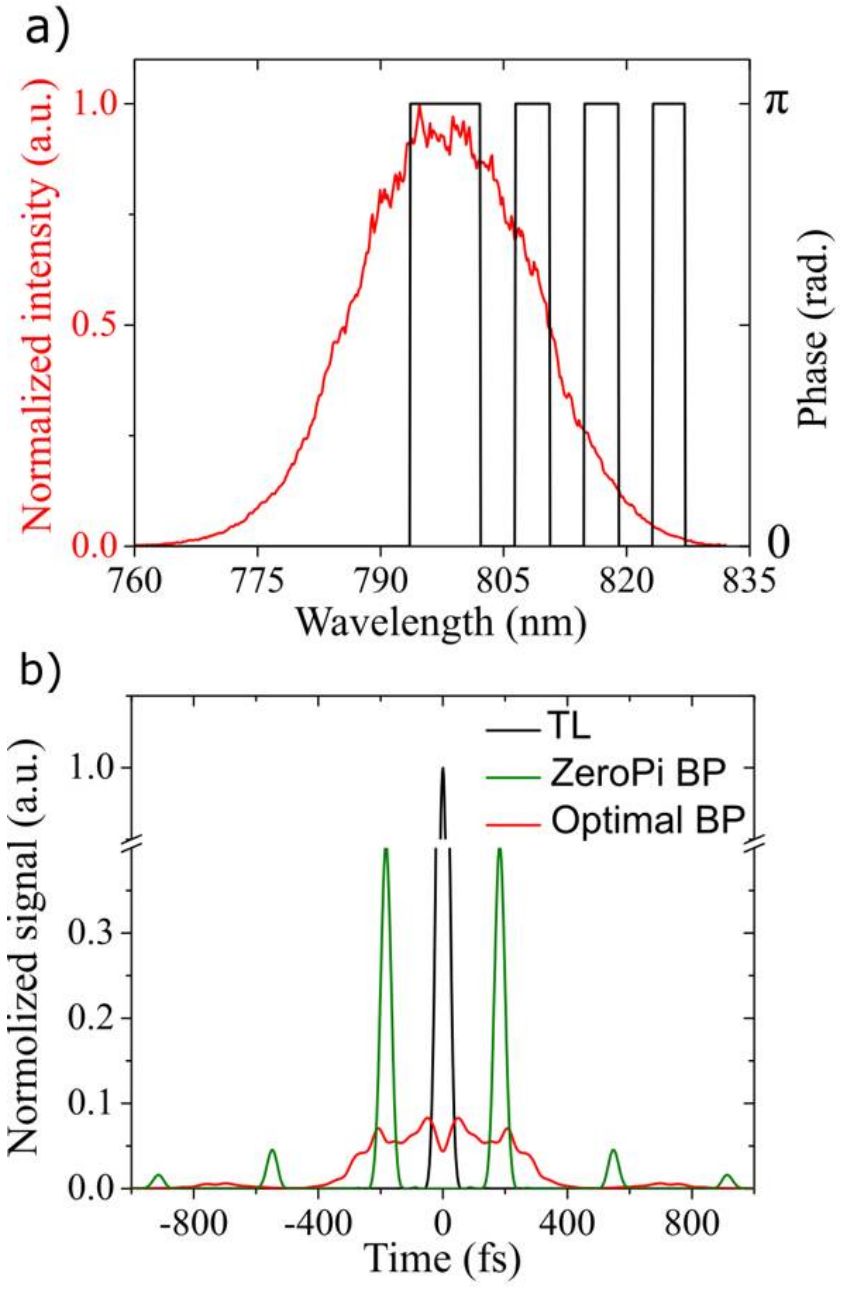

Figure 22. Effect of binary phase shaping for 14 bit binary phases. (a) The red curve corresponds to the laser spectrum; the black line correspond to the optimum 14 bit phase mask. (b) Comparison between simulated pulse profiles in time domain for TL (black), zero/pi sequence (green), and optimal (red) 14 bit binary phases. Note the break in the vertical axis.

In Figure 23 we show the 128×128 matrix of inversed peak power ratio values corresponding to all possible 14-bit binary phases. The search-space corresponds to the peak power reduction for each of the different BPS possible. The row and column index of each element is defined by first and second half of its binary number representation, respectively. In this representation coordinates (0,0) and (128,128) correspond to TL pulses. The global optimum phase with coordinates (65,86) creates 12 times peak power reduction, in this case.

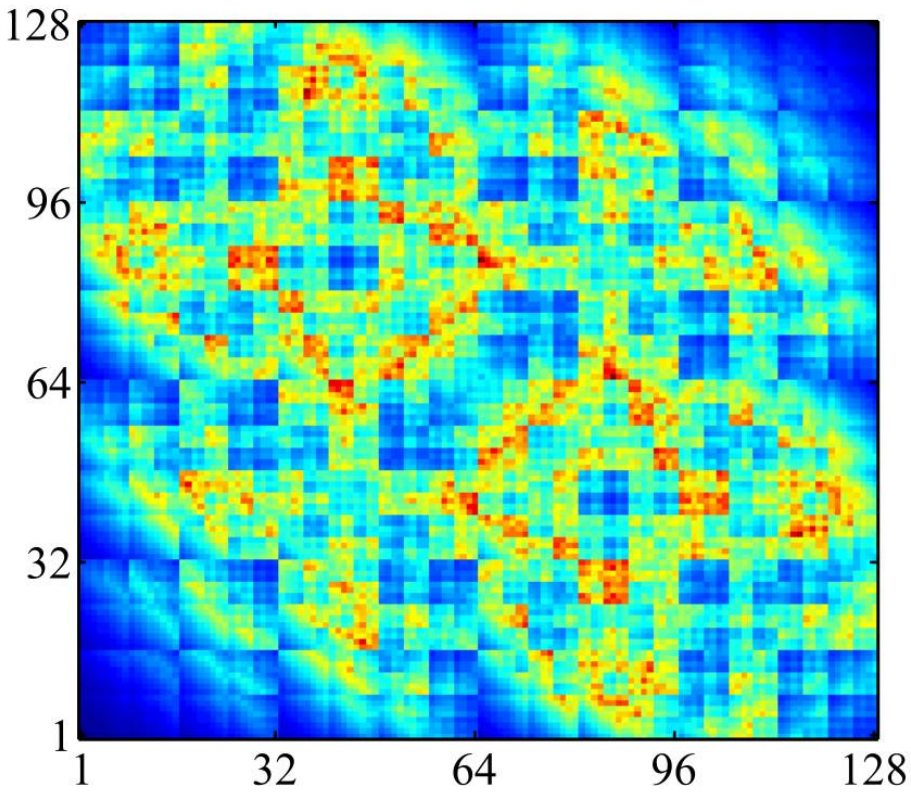

Figure 23. Binary phase matrix 128×128 showing inverse peak power ratio for 14 bit phases. The row and column index of each element is defined by first and second half of its binary number representation, respectively. Red is best, black is no peak power reduction

We find a pattern for the location of the best phases. The pattern is conserved when increasing the number of bits and becomes more detailed. Figure 23 shows the peak power ratio values for the 14 bit binary phases sorted in ascending order.

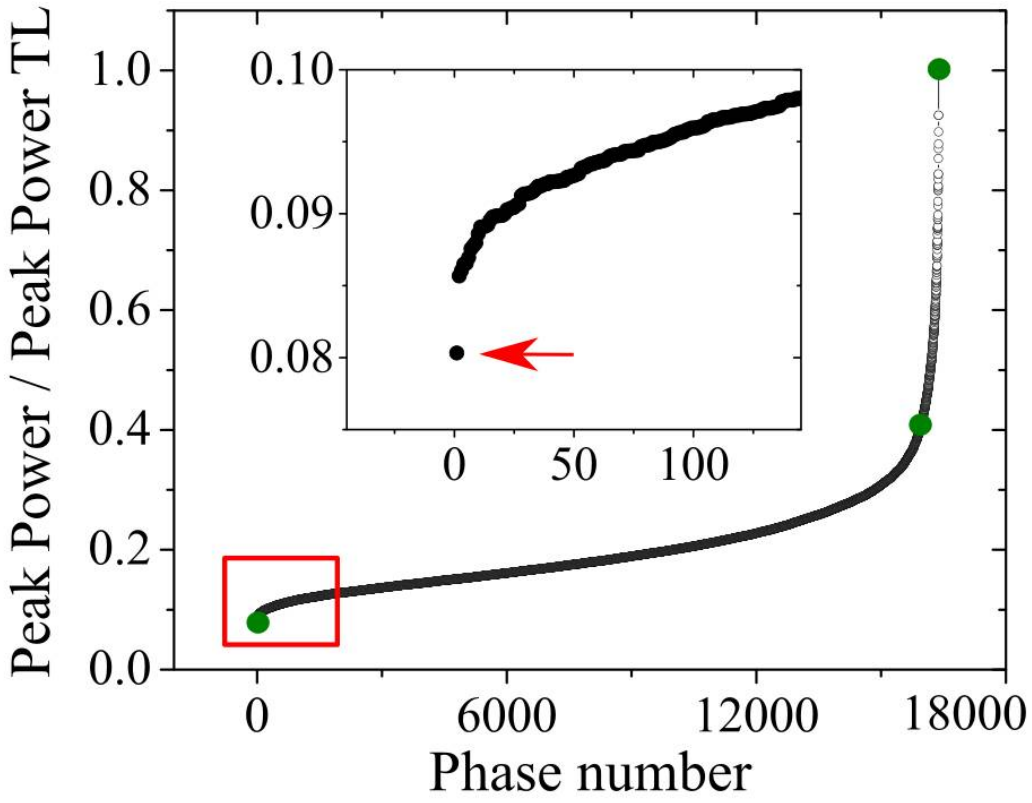

Figure 24. Peak power ratio values from Figure 31 sorted in ascending order. The green dots correspond to the phases shown in Figure 30b. The red arrow points to the optimal phase.

The number of bits needed to decrease the peak power of an ultrafast laser was first explored through numerical simulation. The plot is presented in double logarithmic scale (Figure 25). All the possible phase combinations were evaluated up to 25 bits; see the region between arrows, fitted with red dashed line, and smallest peak power normalized on TL peak power is plotted against corresponding bit number. The smallest peak power was the condition in our algorithm to choose the optimal phase. The slope of the linear fit is -0.95. The deviation from the linear behavior for the bit number >25 arises from the fact that we did not use the optimal binary phase due to computational resources limit; instead of analyzing all possible phase combinations, only 10^6 of them were analyzed. From the prediction line (red dashed line), it follows that with 1400 bits one can achieve 1000 times peak power reduction, which is comparable with stretching applied in CPA systems [99].

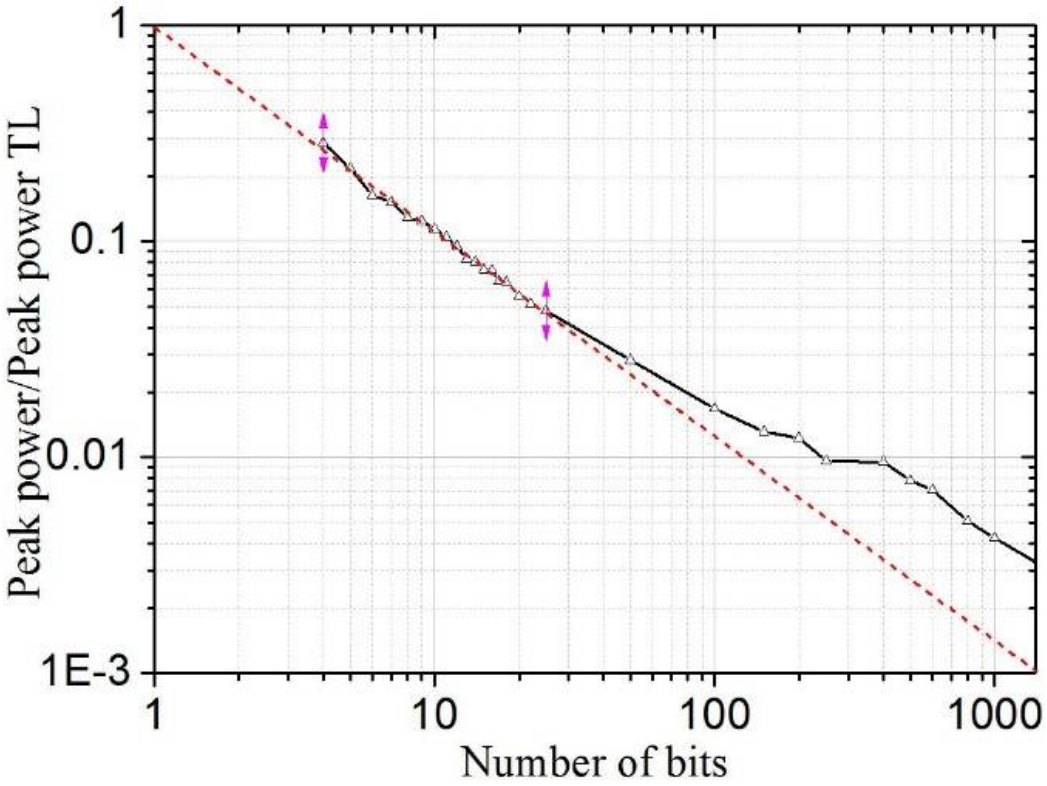

Figure 25. Simulation of binary phase peak-power reduction for 40fs pulses. The dependence of normalized peak power versus binary phase in double logarithmic scale. Triangles connected with black line correspond to calculated values. Red line is a fit based on the linear region. Figure from [88].

For experimental measurements we used a laser system comprising of a Ti:sapphire oscillator (KM labs) and regenerative amplifier (Spitfire, Spectra-Physics, USA), and a pulse shaper (MIIPS HD, BioPhotonic solutions, Inc., USA) with a two-dimensional SLM (792×600 pixels, LCOS-SLM, Hamamatsu, Japan). The laser produces pulses with 40fs duration with the spectrum shown in Figure 22a centered at 800 nm. After the shaper the laser beam was focused on a 1 mm fused silica slab placed on a controllable stage, see Figure 26a. The laser light was collected by spectrometer (USB 4000, Ocean Optics, USA) through a diffusive surface. We measured self-focusing as a function of chirp (quadratic phase) and for selected binary phases.

Before the measurements, the laser pulses were compressed to TL duration using multiphoton intrapulse interference phase-scan [19]. The best binary phase for a particular bit number was found out of 10^6 random phase combinations and applied by SLM on top of compression mask. The fused silica

plate was placed on the stage and a z-scan [100] measurement was performed in order to detect self-focusing. In order to find the chirp-to-bit correspondence BPS mask was switched off and the same scan was run at the same average power with different chirp phases to find the chirp value that matched the amount of self-focusing for binary phase. Two such scans are illustrated for chirp ($29.3\times\tau_0^2 \approx 47000$ fs^2) and binary phase (150-bit phase); see Figure 26b red and black points, respectively. During the experiment we ensured there was no change in the laser spectrum before sample. The dispersion length of the sample is much greater than the thickness of the slab used, therefore all the effects relate to nonlinearities.

The same measurements were performed for 25, 50, 100, and 200 bit phases. Figure 26c, black squares, illustrate the experimental binary phase to chirp correspondence. The red dashed line is the theoretical prediction of binary phase and it's chirp equivalent for 40fs duration pulse. Figure 26c shows that the experimental curve follows the behavior of the theoretical curve with deviation as expected due to limited number of phases being evaluated.

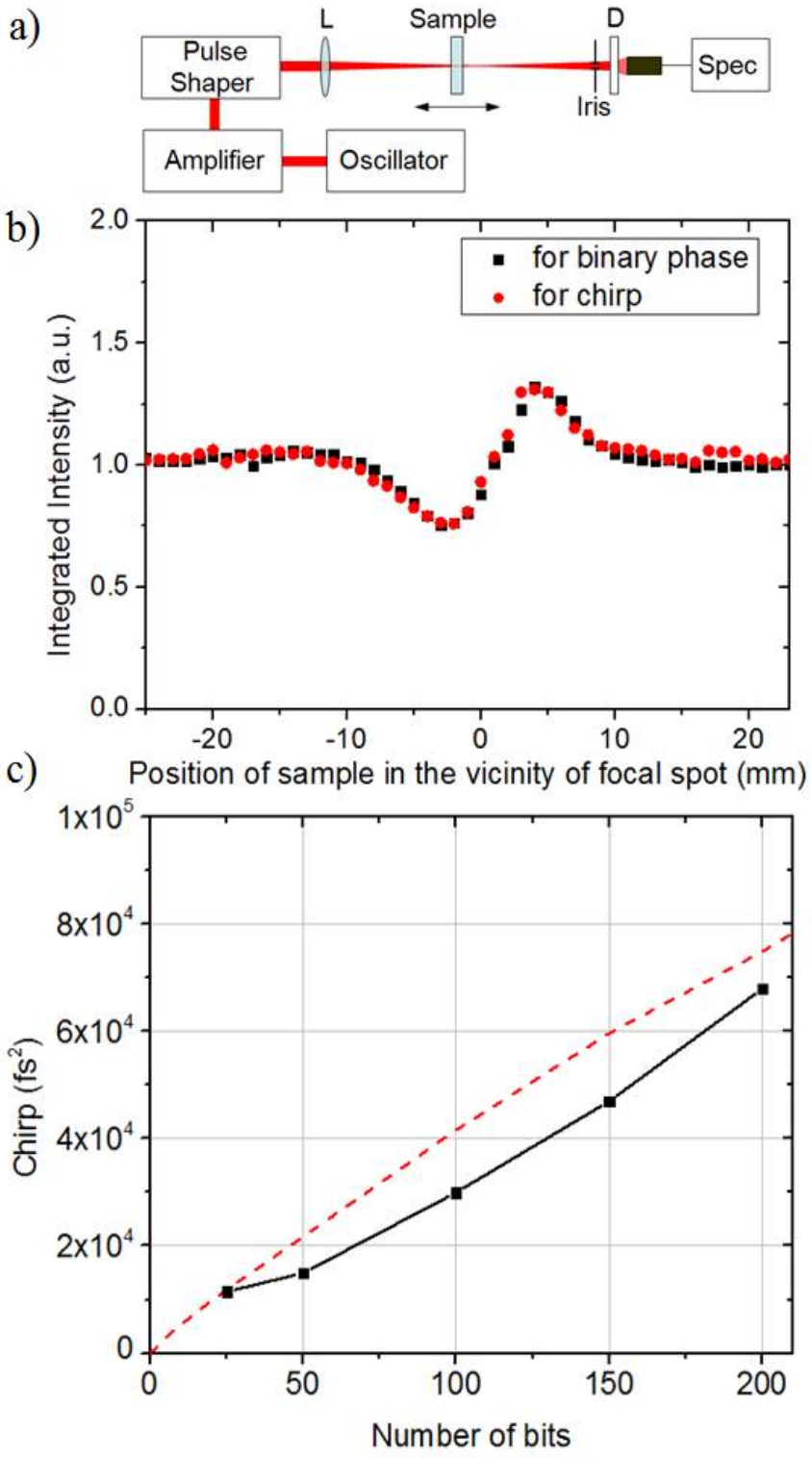

Figure 26. Experimental results. (a) Experimental setup. L, lens; D, diffuser. (b) Integrated signal at different positions of the fused silica window from the focal spot for 150-bit phase, black squares, and chirp value of ~$29.3\times\tau_0^2$ fs^2, red circles. (c) Experimental bit to chirp correspondence (black squares). Red dashed line is a theoretical prediction assuming optimum binary phases. Figure from [88].

A significant difficulty involved finding optimum BPS for large number of bits. Optimization algorithms depend on the search space and on knowledge about the optimum solution. Problems such as optimization of second harmonic signal can be solved quickly because the global optimum is surrounded by promising nearby solutions, i.e. the search space is convex. The other extreme is known as a "needle-in-a-haystack," for which no method is superior to random search [101, 102]. The synthesis of a-priori defined temporal pulses has been solved through the combination of genetic algorithms and Fourier based algorithms [103, 104]. However, these approaches require knowledge of the optimum solution. For example, if the optimum pulse should have a flat top temporal profile, the spectral phase required can be directly written without the need for optimization algorithms [105].

3.3.2 Conclusion

It has been demonstrated that binary phase shaping can be used for self-action processes mitigation. For CPA systems, a large number of bits would be needed, however, spatial light modulators with 12,288 pixels exist (Meadowlark Optics, Colorado). Binary phase modulation could be suitable for laser endoscopy applications, where the final compression would be implemented by a fiber Bragg grating or special multilayer dielectric mirror, for example. The means to estimate how many bits are needed to reduce the peak power for a particular application we provided.

Chapter 4 Designing laser systems for spectroscopy

This chapter discusses the development of two ultrafast laser systems, which are different from typical 800 nm Ti:sapphire systems widely used in ultrafast research. The invention of lasers capable of generating ultrashort femtosecond pulses in the 1980s led to fundamental discoveries in chemistry, physics and biology and prompted the development of novel microscopy methods for biomedical imaging and spectroscopy methods for remote chemical sensing and imaging. Unfortunately, the cost and complexity of ultrashort pulsed lasers has confined them to specialized research laboratories, which in turn has prevented the adoption of nonlinear optical methods as new standards for commercial biomedical imaging or for sensing applications. With the development of the two fiber-based ultrafast systems, we are addressing the problem by presenting more compact, robust, easier to operate ultrafast lasers systems with parameters approaching to those of Ti:sapphire oscillators. The presence of a pulse shaper in the systems enables tailoring pulse parameters to particular applications.

4.1 High-precision high-stability frequency comb source

In stark contrast to ultrafast femtosecond lasers, diode based continuous wave (CW) lasers, i.e. non pulsed, are rugged and inexpensive and therefore used in a thousands of applications ranging from communications to CD and DVD recorders to laser pointers. In this section I present our results on a source of ultrashort pulses that is one order of magnitude less expensive than conventional ultrafast lasers but comparable in performance. The source can be compact, reliable, require no manual tweaking and incorporate computer control arbitrary pulse train synthesis. Immediate applications can be expected in the areas of biomedical imaging, sensing, metrology and communications. In addition, the new source can be ideal for portable sensing instrumentation given the rugged, compact, and energy efficient components.

Ultrashort pulse generation requires bandwidth as well as control of the relative phase of each frequency component of the output. Unlike the lasers that use a cavity with a broad bandwidth gain the current source directly converts two or more individual frequencies into a broad-bandwidth output through the cascaded four-wave mixing (cFWM) process. This process, which is necessary but not sufficient for the creation of ultrashort pulses, has already been intensively studied and demonstrated in

labs elsewhere [106, 107]. In fact, this process is now being considered of great interest in the telecommunications field for wavelength-division multiplexing (WDM) [108]. Trillo in 1994 showed the theory of FWM in optical fibers along with experimental data for long segments of standard single mode fiber (SMF) [109]. Later pulses with picosecond pulse duration (1-10ps) appeared in works of Guy Millot [110, 111]. With the development of fiber based optical communication technology these optical combs were used in signal transmission and required specific shapes of the spectrum, like a flat-top spectrum, rather than shortest pulse duration [112, 113]. The widest bandwidth for this type of laser source was presented in highly non-linear fibers like photonic crystal fibers (PCF). Cerqueira et al. showed about 200 cFWM products spanning 300 nm [114]. Ozeki et all utilizes an idea of alternating segments of highly-nonlinear fiber (HNLF) and SMF, called a comb-like profile fiber, resulting in 97fs pulses [115]. Finally, Cruz showed the ability of this light to generate second harmonic signal, which promises potential good coherence of the light and perhaps form ultrashort pulses [116].

Four-wave mixing process in an optical fiber is a nonlinear interaction among four different waves. In this process energy and momentum of waves must be conserved. During FWM process photons from one or more waves are annihilated and new photons are created. For instance, three waves with frequencies ω_1, ω_2 and ω_3 interact in the fiber in such a way that two photons ω_1 and ω_2 are annihilated and two new photons ω_3 and $\omega_4 = \omega_1 + \omega_2 - \omega_3$ are created. Notice that photon of frequency ω_3 was already present in the field, therefore is amplified. The photon ω_4 is at newly generated frequency, and therefore represents spectral broadening. The special case where $\omega_1 = \omega_2$ is referred to as degenerate FWM. FWM can be described as a nonlinear optical polarization [114]:

$$P(\omega_4) \propto E_1 E_2 E_3^* e^{-i[\beta(\omega_1)+\beta(\omega_2)-\beta(\omega_3)]z}, \tag{22}$$

where E_i is the electric field amplitude at ω_i, $\beta(\omega)$ is the waveguide propagation constant at frequency ω and z is the propagation distance inside the fiber. For efficient generation, there should be a phase matching between phase of nonlinear polarization and a phase of field at frequency ω_4. This phase-matching requirement occurs when the net wave-vector mismatch $\kappa = 0$, where κ is given by:

$$\kappa = \Delta\kappa_M + \Delta\kappa_W + \Delta\kappa_{NL}=0, \quad (23)$$

where $\Delta\kappa_M$, $\Delta\kappa_W$ and $\Delta\kappa_{NL}$ represent the mismatch occurring as a result of material dispersion, waveguide dispersion and nonlinear effects, respectively. To obtain phase matching, at least one of them should be negative. In order to obtain high efficiency, the product $\Delta\beta L$ must be small, where L is the fiber length, and

$$\Delta\beta = \beta(\omega_4) + \beta(\omega_3) - \beta(\omega_1) - \beta(\omega_2). \quad (24)$$

As the waves propagate through the fiber, FWM processes may occur involving the waves generated previously, creating in this way photons at further new frequencies (see Figure 27), which is called as cascaded or multiple FWM. This frequency cascading is formed by signals with well-defined frequency and phase differences, therefore predicted to have very good coherent properties.

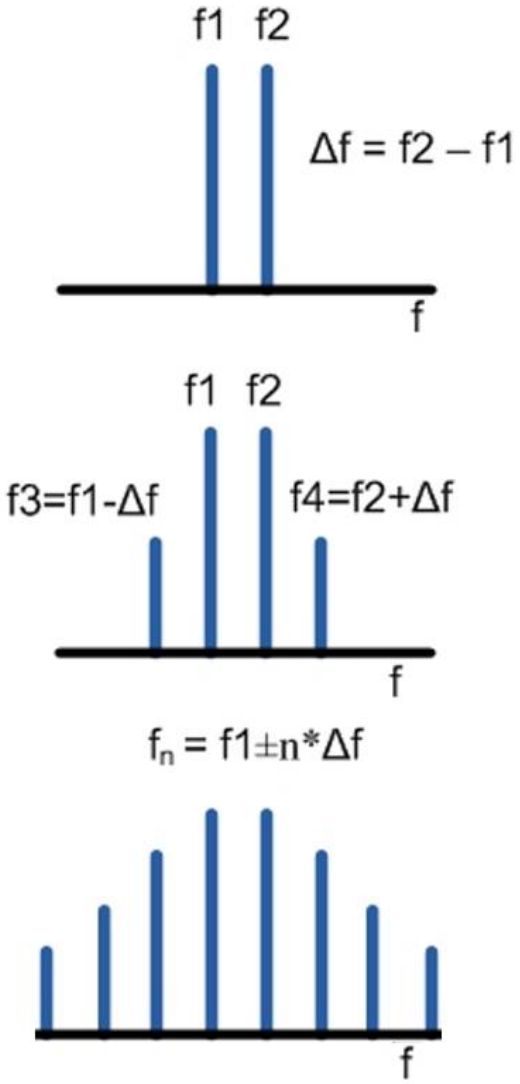

Figure 27. A schematic illustration of cascaded four-wave mixing process.

Material dispersion plays a fundamental role in phase matching. The efficiency of cascaded FWM can be optimized by using two pump lasers with frequencies near the zero-dispersion frequency. Therefore, the use of fibers that provide efficient dispersion management and high nonlinearity at the same time, can be useful to enhance the efficiency of the multiple FWM process.

In order FWM to be efficient, nonlinearity of the fiber should be substantial. The fused silica a material with a very low nonlinear index and nonlinearities become visible only at very high peak intensities in bulk materials. On the other hand, nonlinearities in optical fibers are easily generated due to the tight confinement of the optical power into a small core area and the long interaction length with an

optical field. Practically, the nonlinear coefficient of γ is often used to determine the magnitude of the Kerr nonlinearities in fibers and can be written as:

$$\gamma = \frac{2\pi}{\lambda} \cdot \frac{n_2}{A_{eff}}, \tag{25}$$

where λ is the free-space wavelength, n_2 is nonlinear refractive index and A_{eff} is the effective area of a fiber. To enhance γ, a fiber heavily doped with GeO_2 in the core area, and a large refractive index difference between the core and the cladding is preferable because such fibers have a small A_{eff} and a large n_2. Figure 28 [117] shows the schematic refractive index profiles of an HNLF and a standard single-mode fiber (SMF). In typical HNLFs, the relative refractive index difference of the core to the outer cladding is around 3%, while the core diameter is around 4 μm. Consequently, γ of typical HNLFs is enlarged to about 10 $(W \cdot km)^{-1}$, which is about ten times as large as that in SMF.

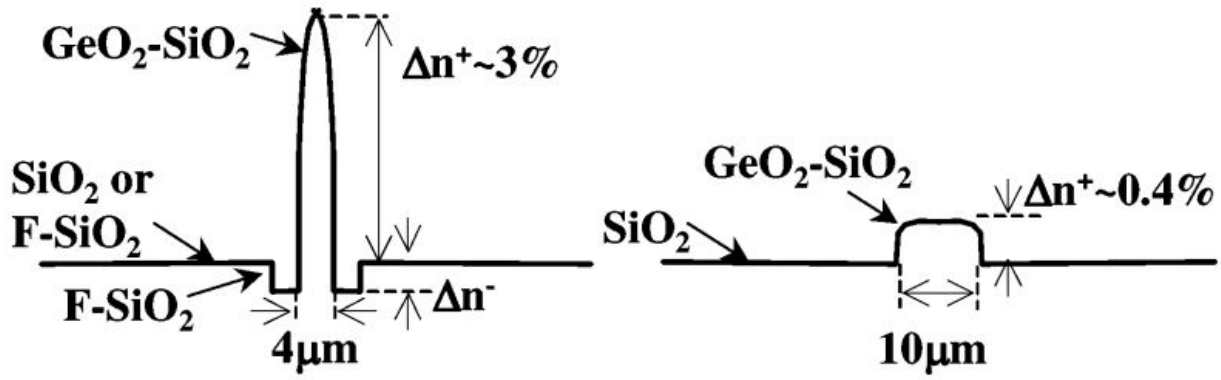

Figure 28 Comparison of refractive index profiles for HNLF and SSMF.

In this work we investigate the phase properties of the laser source based on CFWM process in highly nonlinear optical fiber using 4-f pulse shaper as a phase manipulation instrument. Phase characterization and compensation leads to effective compression of the output pulses to sub-45fs, comparable with current mode-locked solid-state and fiber lasers.

4.1.1 Laser schematic

The cascaded FWM laser experimental setup is illustrated in Figure 29 [118]. Two distributed feedback (DFB) fiber lasers with linewidth<0.1 kHz, each producing 6 mW single-frequency continuous

wave, are combined by a 50/50 polarization-maintaining (PM) fiber coupler. The output of these two DFB lasers can be tuned independently from 1,549.17 to 1,551.36 nm. A $LiNbO_3$ Mach-Zehnder intensity modulator converts the combined CW light into 40 ns pulses with low duty cycle. The modulated pulses are seeded into an Erbium-doped fiber amplifier (EDFA), which can deliver maximum output average power of 4 W. Then, the amplified pulses are coupled into a segment of HNLF to generate cFWM. The HNLF used here has zero-dispersion at 1550 nm, a dispersion slope of 0.019 ps/(nm^2·km) and a nonlinear coefficient of 11.5 W^{-1}km^{-1}. The spectrum of the output pulses is monitored by an optical spectrum analyzer (OSA, HP70951A) with 0.1 nm resolution.

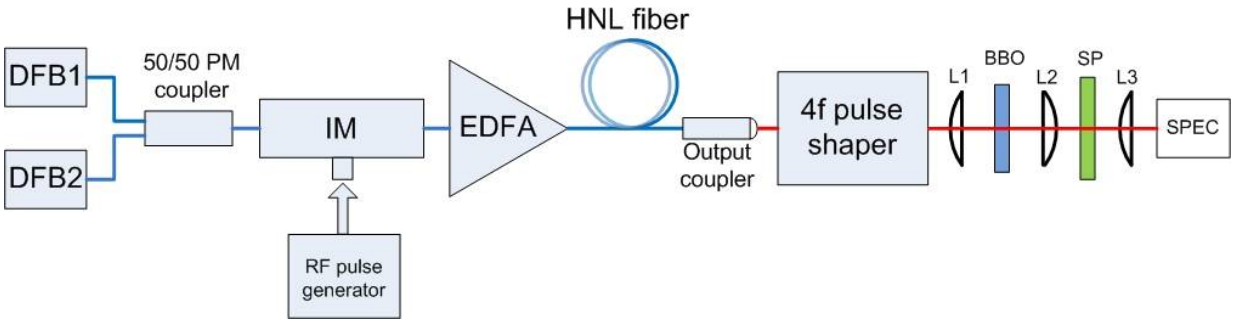

Figure 29. Schematic of laser setup and its characterization and compression. DFB, distributed feedback fiber laser; IM, intensity modulator; EDFA, erbium doped fiber amplifier; HNLF, highly nonlinear fiber; BBO, barium-borate crystal; SP, short-pass filter; L1, L2, L3, lenses; SPEC, spectrometer. Figure from [118].

The generated cFWM comb pulses from HNLF are characterized and compressed using a MIIPS-enabled 4-f pulse shaper (MIIPS Box 640, Biophotonic Solutions Inc.) [52], which can perform discrete phase manipulation for each comb line individually. Output pulses from the shaper are focused onto a 1-mm-thick BBO crystal. The generated second harmonic generation signal is detected by a compact spectrometer (QE65k, Ocean Optics) and used as feedback for phase control. A thinner 0.1-mm-thick BBO crystal also was tested, and the SHG signals were identical in shape and behavior. This indicates that 1-mm-thick fully supports the bandwidth. Intensity autocorrelation (AC) of the compressed pulses is measured by the pulse shaper and a non-collinear autocorrelator separately.

4.1.2 Laser performance and pulse compression

Two DFB lasers outputs are tuned to 1549.17 nm and 1551.36 nm, respectively, which are near the zero-dispersion wavelength of the HNLF. These wavelengths are extreme for DFB laser we have. This seed wavelength separation results in 273 GHz repetition rate of final pulse train. The intensity modulator produces 40 ns pulses with 170 kHz repetition rate. This condition is required to obtain optimized amplification and get high peak power. Amplification by the EDFA, results in pulsed output with average power of ~0.4 W which is then coupled into a 13 m long HNLF. The output spectrum from the HNLF consists of equidistantly spaced spectral lines that span from 1500 nm to 1590 nm (Figure 30). The line gap of 2.19 nm and two central lines in the spectrum are coincident with the output of the two DFB lasers. The rest of the frequency comb lines are generated by cFWM on both sides of the seed frequencies. It is observed that the total number of lines depends on the length of HNLF and the power of radiation launched into it. Under current experimental conditions, 13 m HNLF is found to be optimum to generate maximum number of comb lines, ~40 with intensities >−30 dBm. With shorter fiber, fewer lines are produced due to less nonlinearity. Longer fiber does not necessarily lead to a greater number of comb lines because the HNLF used here has a non-zero dispersion slope, thus, phase matching is not fulfilled far from the seed frequencies. Generally, more power also gives more spectral lines because of the nonlinear nature of the cFWM process; however, it is still limited by phase-matching requirements. With certain HNLF length, increasing pump power produces supercontinuum generation which does not have a predefined comb structure and is not fully coherent.

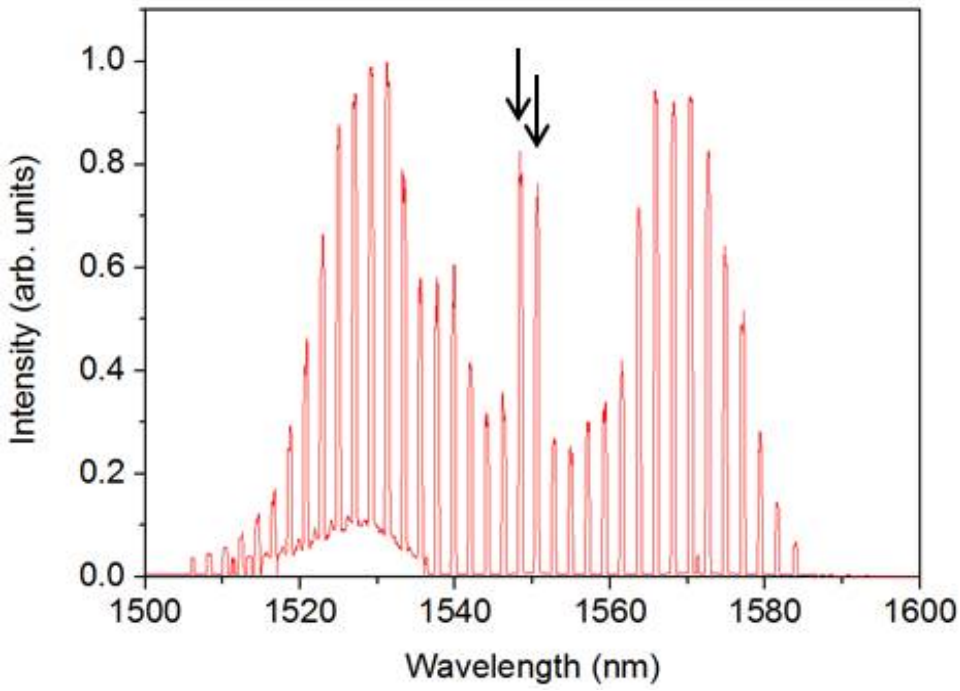

Figure 30. Experimental fundamental spectrum for 13 m segment HNLF. Two black arrows show seeding lines from DFB lasers. Figure from [118].

The shape of the spectrum, periodic modulation of envelope, indicates the presence of self-phase modulation process in addition to cFWM. This diminishes an application of this laser source in telecommunication or metrology, which require more uniform spectrum. On the other hand, for generation of ultrashort pulses SPM is playing positive role by broadening the spectrum, provided pulses can be compressed on the output [119].

To characterize the generated pulses, the HNLF output is sent to the 4-f pulse shaper, with the laser spectrum spread across a spatial light modulator. This enables discrete phase modulation for each line individually. With the phases of other lines fixed, one line is scanned from $-\pi$ to $+\pi$, while the integrated SHG signal is monitored. After the scan, the delay corresponding to maximum SHG signal is applied to this set of pixels. Then, this process is repeated for each of the comb lines, and then repeated across the whole spectrum a few more iterations until the integrated SHG signal no longer improves. The final phase settings for 9 central lines are shown in Figure 31a with a polynomial fit of the discrete phase plot (red curve in Figure 31a), that shows a mainly quadratic phase distortion of about $-12\ 000\ fs^2$. The

sign and magnitude of the linear chirp depends on the length of HNLF and output powers from EDFA. In our experiments it evolved with the spectrum change and varied from −80 000 fs^2 to +10 000 $fs^2$for fiber lengths from 50 to 5 meters respectively. It is also noticed that, the SHG spectrum changes with the compensation phase applied (Figure 31b).

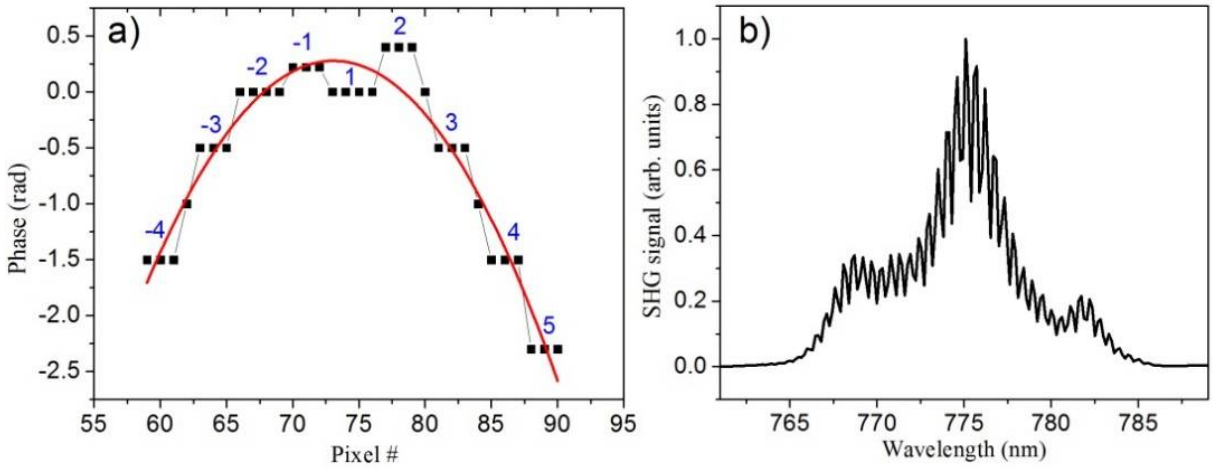

Figure 31. (a) Line-by-line phase corrections (shown only 9 central lines, indexed with blue numbers). Each black dot shows the phase of corresponding pixel. Red curve is a second order polynomial fit of phase values. Pump lines corresponding to 1549 and 1551 nm are denoted as -1 and +1, respectively. (b) SHG spectrum changes with continuous quadratic phase applied across all spectral lines. Figure from [118].

The result of phase compensation obtained for 13 meters of HNL fiber is presented in Figure 32. The compressed pulses are further characterized by autocorrelation. Shaper-based collinear non-interferometric auto correlation (Figure 32a) shows full-width-half-maximum (FWHM) of ~70 fs, which corresponds to 45 fs pulse duration. The peak-to-baseline ratio for these parameters is about 4:1, which indicates the presence of uncompressed light or a broader pedestal. We believe this light can come partially from the EDFA, which was pushed to its limits of amplification. Another source of the pedestal can be supercontinuum generation inside of HNLF, which takes place at some point after cFWM process stops.

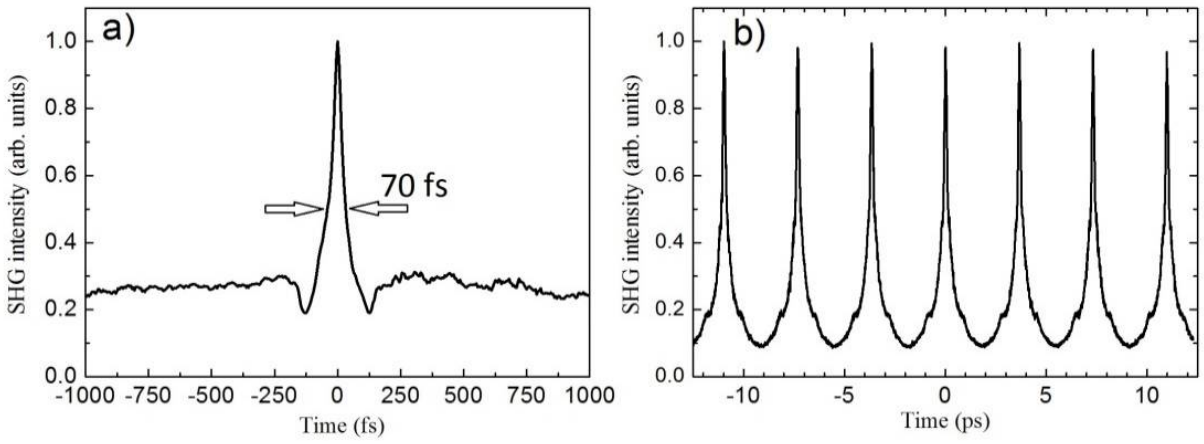

Figure 32. Pulse characterization. (a) Shaper-based non-interferometric auto correlation. (b) Train of pulses with repetition rate 3.6 ps (not compressed output). Figure from [118].

Additional autocorrelation measurement (Figure 32b) is performed using a non-collinear optical autocorrelator with a scan range of ~30 ps. This autocorrelation shows the repetition period of femtosecond pulses is 3.66 ps which is in agreement with the 2.1 nm line separation in comb spectrum. The repetition rate is tunable but strongly affects pulse duration as it changes bandwidth of spectrum (which is roughly number of lines timing line separation). According to long range AC, laser output is very stable in amplitude and phase, note that one pulse is correlating with subsequent pulse in the pulse train.

4.1.3 Conclusion

Synthetic frequency comb generation by cascaded four-wave mixing in highly-nonlinear fiber was investigated for its ability to generate ultrashort femtosecond pulses. Line by line shaping was carried out using a 4-f pulse shaper and it resulted in mainly linear chirp (quadratic phase dispersion). The autocorrelation of the compressed output pulses showed a pulse duration of 45 fs, which is the shortest pulse duration reported from external cavity frequency comb sources. The simplicity of the all-fiber design and superb stability observed over time are encouraging for application of the source for spectroscopy.

4.2 Characterization and adaptive compression of multi-soliton laser source

We have considered developing an eye-safe long-wavelength (1400-2000 nm) range laser system for coherent Raman scattering spectroscopy. For a long time, the inverse 4th-power wavelength dependence of spontaneous Raman signal has led to great interest in the development of UV-Raman for trace explosives detection. In particular, systems using wavelengths shorter than 260 nm have been shown to avoid fluorescent signals [120]. Conversely, near-infrared wavelength lasers have been considered impractical because the spontaneous Raman signal from a 250 nm laser would be 1477 times stronger than the signal from a 1550 nm laser, because of the inverse 4th-power wavelength dependence mentioned above. Fortunately, coherent Raman processes such as coherent anti-Stokes Raman scattering do not have the same wavelength dependence. Spontaneous emission, given by Einstein's coefficient A_{21}, can be written as

$$A_{21} = \frac{16\pi^3 c}{3\varepsilon_0 h\lambda^3}\left|M_{21}\right|^2, \tag{26}$$

where λ is the wavelength of light, ε_0 is permittivity of vacuum, h is Planck's constant, and M_{21} is the transition dipole moment. Spontaneous emission is responsible for the high-order dependence on wavelength. On the other hand, stimulated emission/excitation does not have this wavelength dependence, as can be seen from the Einstein B_{12} coefficient:

$$B_{21} = \frac{2\pi^3}{3\varepsilon_0 h^2}\left|M_{21}\right|^2. \tag{27}$$

One can thus conclude that the 1400 to 2000 nm wavelength region can be used for eye-safe high sensitivity coherent Raman spectroscopy, avoiding the steep wavelength penalty of spontaneous processes. Soliton self-frequency shift (SSFS) in optical fibers resulting from anomalous dispersion regime pumping [121-123], has been considered ideal for generating the broad bandwidth above 1400 nm, especially when using large mode area (LMA) fibers or photonic crystal (PC) rods [124]. The low dispersion of an isolated SSFS soliton leads to well behaved ~70 fs pulses [124, 125]. When pumped

with high-energy pulses, however, SSFS in a PC rod results in greater than 300 nm bandwidth output spectrum consisting of a dispersive wave and a train of independent pulses resulting from soliton fission, each one experiencing different spectral shift, dispersion, and time delay [126, 127]. In this project we explore the possibility of characterizing and compressing such a complex multi-soliton source with the hope of having greater intensity, bandwidth and shorter pulses.

Characterization of supercontinuum pulses from photonic crystal fibers in the normal dispersion regime is challenging but has been reported [128-132], and in few cases has led to sub-10 fs compressed pulses [132]. Multi-soliton SSFS sources are particularly difficult to characterize because they consist of multiple (two or more) solitons, each with different carrier frequency and group velocity dispersion. Characterization and compression of the multi-soliton output requires the independent characterization and compression of each soliton, followed by coherent phase combining of all the solitons into a single coherent pulse. While accomplishing this manually seems a formidable task, we take advantage of a broadband pulse shaper and the multiphoton intrapulse interference phase scan characterization and compression method [17-19, 45]. Results from two different laboratories are presented.

4.2.1 Experimental setup and results

The experiments were carried out in two different laboratories, one at Cornell and one at Michigan State University (MSU). The experimental setup, see Figure 33, for both laser setups was very similar. The setup consists of a pump laser (Cazadero, Calmar Laser) producing ~500 fs pulses at ~1550 nm central wavelength. At Cornell, the laser was running at 1 MHz, producing 1.3 μJ/pulse, coupled into 37 cm long LMA PC rod (100 μm diameter, NKT Photonics, Denmark). At MSU the laser was running at 2 MHz, producing 0.41 μJ/pulse, coupled into 45 cm LMA PC rod (100 μm diameter, NKT Photonics, Denmark). The soliton order was calculated to be 14 and 7 for the first and the second laser setups, respectively [127]. Dispersion of the rods was anomalous in the spectral range of interest, with dispersion parameter ~25 ps/nm/km at 1550 nm. The nonlinear parameter was estimated to be ~ 0.03 $W^{-1}km^{-1}$. Coupling efficiency into the rod was ~ 93% for both lasers. A pulse shaper (MIIPS Box 640, Biophotonic Solutions Inc., USA) was used to measure and correct phase distortions of the rod

output using MIIPS [19], and to obtain the interferometric autocorrelation on the pulses. The pulse shaper first isolated each of the solitons, to characterize their spectral phase, and to adaptively compress them by introducing a phase that cancels the dispersion measured for each soliton. After compression, the pulse shaper synchronized the arrival of each soliton in order to coherently combine them. We compared autocorrelations measured by the MIIPS software with a numerical simulation based on fundamental spectrum. Second harmonic signal was generated in 10 μm beta barium borate Type I crystal and used as a feedback for the pulse shaper. Phase matching bandwidth of the BBO crystal covered the entire optical bandwidth of system output.

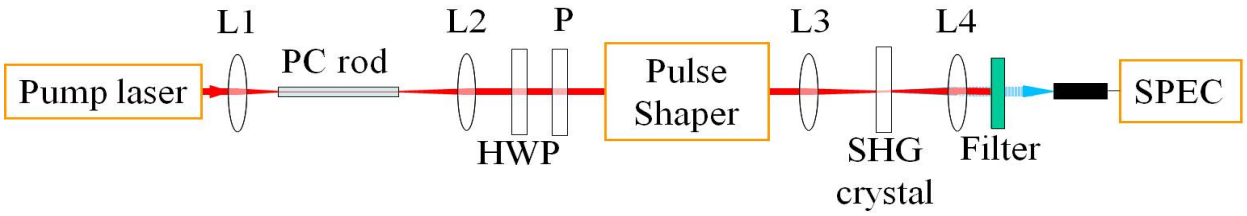

Figure 33. Schematic of the experimental setup for multi-soliton generation: L1-4, lenses; HWP, half-wave plate; P, polarizer.

Figures 34a and 34b show the multi-soliton broadband output spectra for the two laser setups. In both cases, we observe two fundamental solitons and a dispersive wave due to high-order nonlinear effects. The output spectrum depends on the pump intensity, wavelength-dependent fiber parameters, and self-induced Raman scattering process. As each soliton propagates in the PC rod, the intrapulse Raman scattering effect and group velocity walk-off separate them from the residual input and from one another [127, 133]. This also reduces the influence of blue-shifted non-soliton radiation, resulting in better stability for the longest wavelength soliton. The spectrum in general contains four components: a high intensity modulation instability (MI) region that overlaps some residual input pump pulse, a blue shifted dispersive wave, and two red shifted solitons 1 and 2 in Figures 34a and 34b. Note that the spectrum in Figure 34a is broader than the one in Figure 34b, because of the greater input pulse energy.

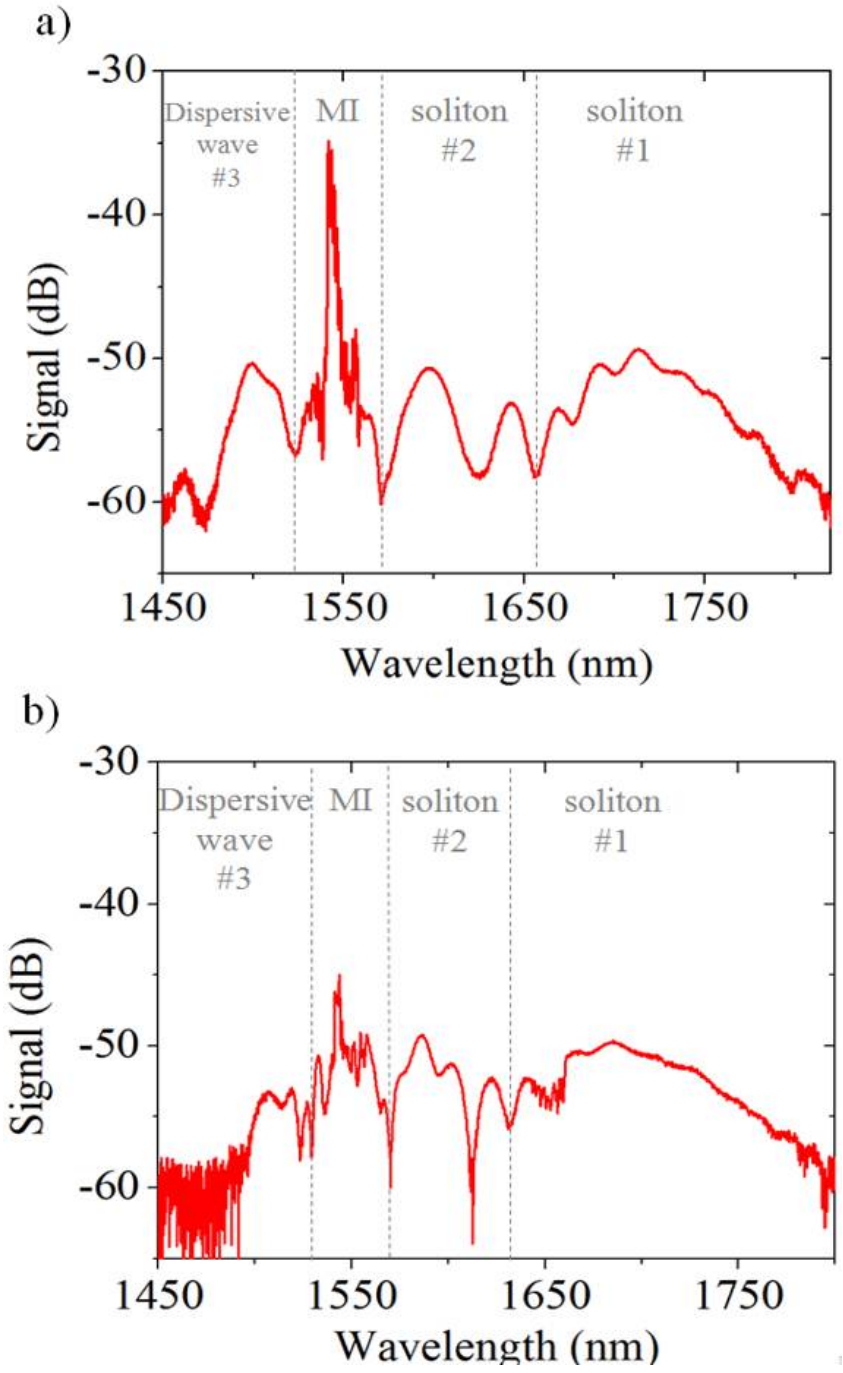

Figure 34. Multi-soliton spectra of LMA PC rod output in semi-logarithmic scale for (a)1.3 μJ pump pulse energy and 37 cm long PC rod; and (b) 0.4 μJ and 45 cm long PC rod.

We performed simulations for 100 pulses coupled to a PC rod with random intensity noise [127] in order to determine the expected output pulse-to-pulse fluctuations, degree of coherence. We used the experimentally measured parameters with 1% power fluctuations. Figure 35 (red curves) shows the

average spectrum for both laser systems, which are in a good agreement with the experimental spectra. The degree of coherence, calculated as in [134], is shown in Figure 35 as black curves. The overall coherence is high for the majority of the spectral components with spectral intensity.

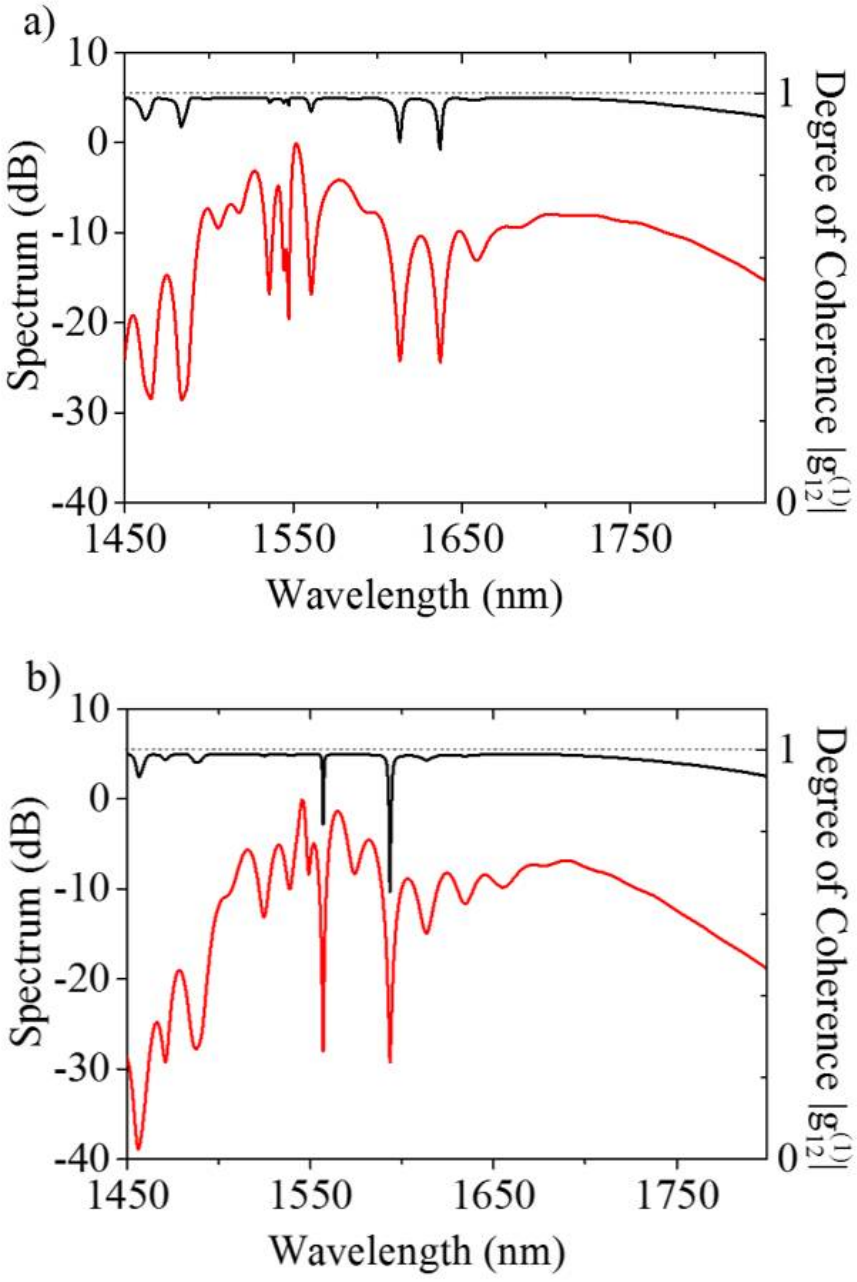

Figure 35. Average spectrum (left axis, red curve) and degree of coherence (right axis, black curve) calculated for an ensemble of 100 pulses for (a) the first laser system with 1.3 μJ pump pulse energy and 37 cm long PC rod; and (b) the second laser system with 0.4 μJ/pulse and 45 cm long PC rod.

Figures 36a and 36d show the MIIPS traces obtained for laser setups. In both cases, the incoherent MI with residual input region between 1540 nm and 1558 nm was blocked with a card at the spatial light modulator in the pulse shaper. In a MIIPS trace, second harmonic generation intensity is plotted as a function of wavelength and chirp applied by a pulse shaper [18]. One can distinguish the SHG from each of the two solitons marked as 1 and 2 and the dispersive wave emission marked as 3. Two additional signals, labeled as 1+2 and 2+3, result from sum-frequency generation. Individual compression, done by transmitting the desired part of spectrum and blocking other parts at the SLM, resulted in 57 fs, 155 fs, and 150 fs pulses for the first laser setup; and 90 fs, 156 fs and 210 fs for second laser setup, for spectral regions 1, 2, and 3, respectively. Delay scans for the first laser setup revealed a 540 fs delay between solitons 1 and 2, and ~120 fs between 2 and 3. Delay scans for the second laser setup showed 900 fs delay between solitons 1 and 2, and 700 fs between 2 and 3. After delay compensation, the coherent output is close to transform limited as confirmed by the MIIPS trace shown in Figures 36b and 36e, where most of the SHG intensity is concentrated at zero-chirp. Numerical simulation of SHG chirp scan based on the experimental spectra for a transform-limited pulse, shown in Figures 36c and 36f, is in close agreement with the experiment, indicating successful compression. Note that MIIPS corrected the dispersion of all optics including the shaper to achieve TL pulses.

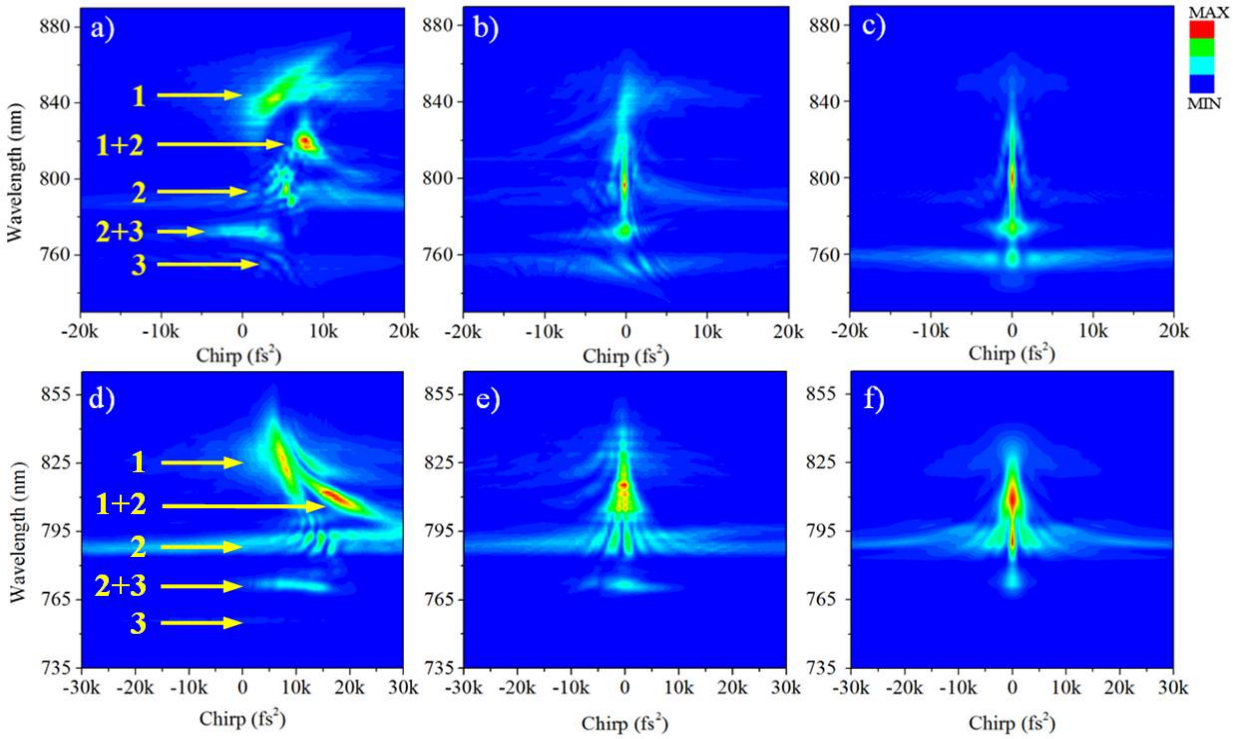

Figure 36. MIIPS traces showing the SHG intensity as a function of wavelength and spectral chirp: (a)-(c) for 1.3 μJ per pulse and 37 cm long PC rod; (d)-(f) for 0.4 μJ per pulse and 45 cm long PC rod. (a) and (d) before compression, (b) and (e) after compression, (c) and (f) numerical calculation assuming transform-limited pulses based on the input spectra. Each trace was independently normalized.

Cross-correlation frequency-resolved optical gating (XFROG) of the second laser system output, using the longer wavelength soliton at 1668 nm as a reference, reveals the time delay among the different output spectral regions, see Figure 37. In Figure 37a one can see that each of the components has a different time delay, for example 900 fs between solitons 1 and 2, and 700 fs between soliton 2 and the dispersive wave. In Figure 37b we show a corresponding trace after the dispersive-wave and the two solitons were synchronized, and coherently phase combined. The fundamental spectrum is shown on the right, Figure 37c, as a reference. Cross-correlations of the laser source prior to and after compression demonstrate the multi-soliton output with overall 'pulse duration' greater than 1500 fs is compressed to ~ 30 fs, resulting in a compression factor of ~50.

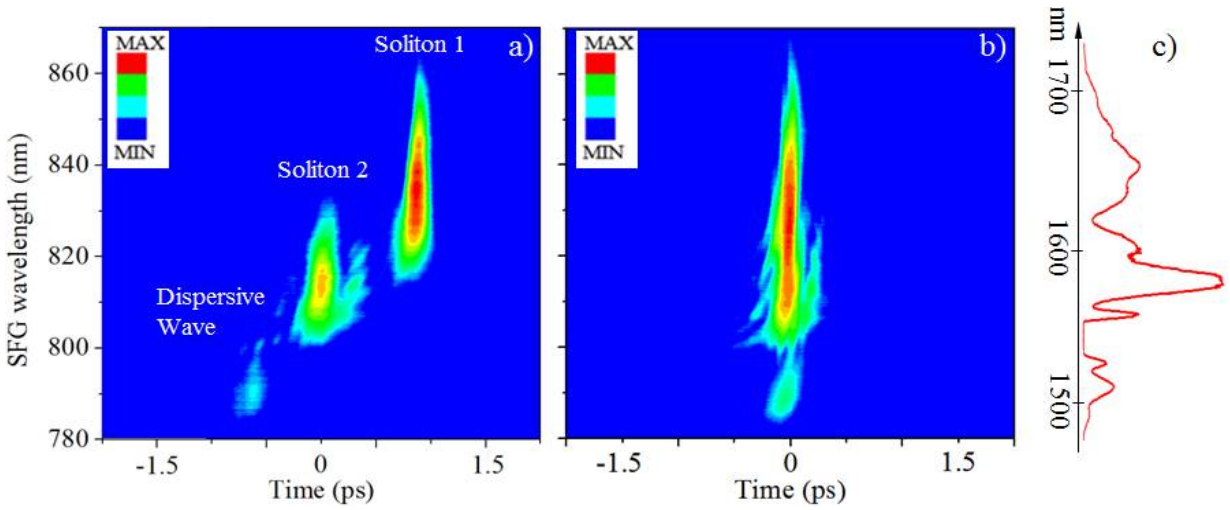

Figure 37. Measured cross-correlation traces of the PC rod output without (a) and with (b) delay compensation. Intensity is presented in logarithmic scale. Plots were centered at soliton 2 for symmetry. (c) Fundamental spectrum. Note the wavelength axis of the fundamental spectrum is not linear.

The integrated SHG intensity was ~3 times greater after the compression for both lasers. The SHG spectrum and interferometric autocorrelation of the output, and their numerical simulations, are shown in Figures 44a-44c for first laser sistem and Figures 38d-38f for second one. Side lobes in both cases result from the highly structured spectrum. The pulse used to calculate the pulse width was determined by fitting the autocorrelation. We found sech^2 fit well down to 10% of the amplitude, a Gaussian function did not fit well below the 50% intensity level. The pulse duration, full width at half maximum (FWHM), for the first and second lasers were 28 fs and 45 fs, respectively. For the first laser setup, the energy per pulse and peak power after compression were measured to be 0.3 μJ and 10 MW, respectively; and 0.15 μJ and 3.15 MW for the second one. These energies are almost an order of magnitude higher than the energy that has been used for *in vivo* three photon microscopy [135].

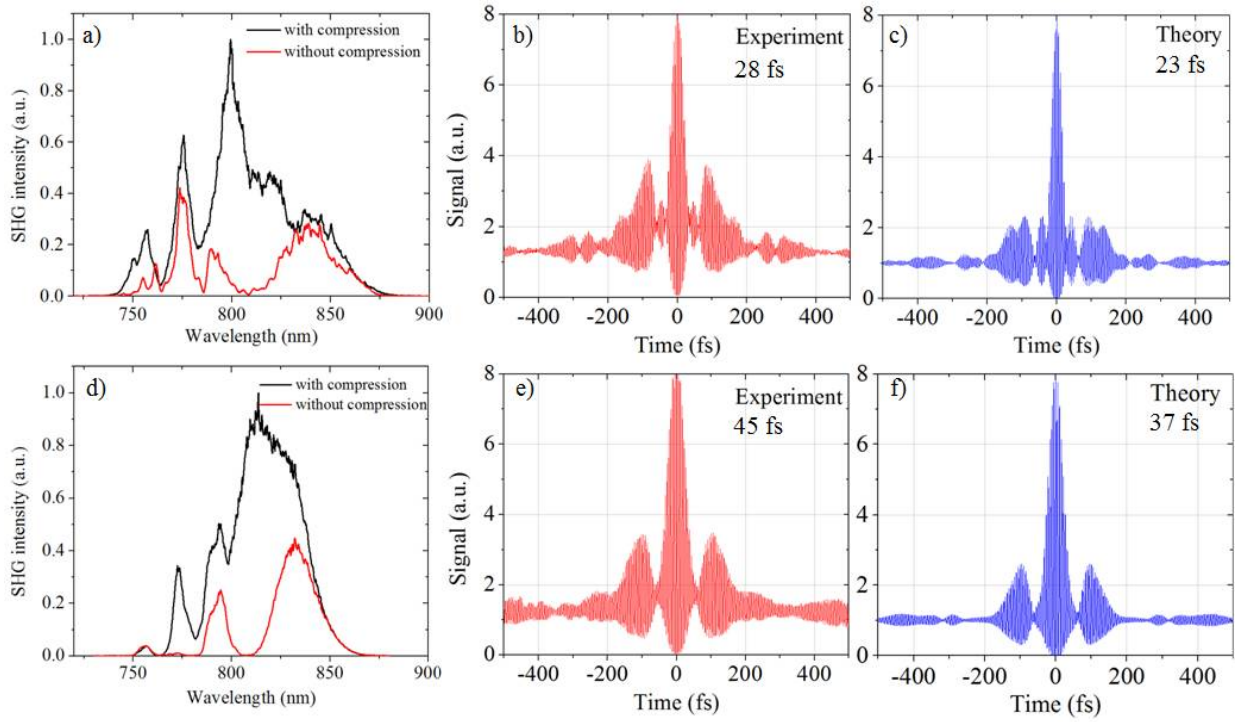

Figure 38. Results after compresssion. (top row) for the first laser setup, (bottom row) for the second laser setup. (a) and (d) are SHG normalized intensities before and after compression. (b) and (e) are experimental interferometric autocorrelations. (c) and (f) are theoretical interferometric autocorrelations.

In order to characterize the pulse-to-pulse noise of the laser source, namely spectral amplitude and phase fluctuations, we used the fidelity parameter [136]. The fidelity measurement involves a calculation of the ratio between theoretical and experimental normalized intensities of the second harmonic signal as a function of linear chirp. An ideal laser has a fidelity parameter of 1.0, Ti:Sapphire oscillators have a fidelity parameter greater than 0.9, and fiber lasers of 0.8-0.9. It has been shown that spectral phase and amplitude noise result in distinct fidelity signatures [136, 137]. Figure 39a shows the fidelity measurement for the multi-soliton source of the first laser setup. A fidelity parameter of ~0.48 is estimated as the asymptotic value (after ±15k fs^2) of our measurements. The second laser system had a 10% greater fidelity after a few technical improvements such as isolation the laser from ambient airflow, shorter optical path between pump laser and length of the PC rod. The relatively low fidelity values observed for multi-soliton compression indicate pulse-to-pulse spectral breathing in the output [136], but the shape of the fidelity curve indicates the phase of the output spectrum seems stable. Spectral breathing

results from the phase and amplitude instability of the pump laser, which degrades the coupled peak intensity in the PC rod. This behavior agrees with previous studies on the coherent properties of supercontinuum in a PC rod in the anomalous dispersion regime [134]. Fidelity measurements of the isolated (longest wavelength) soliton for the same laser system, shown in Figure 39b, give an asymptotic value of ~0.9, confirming superior pulse quality and coherence. Typically, this soliton is used for Raman microscopy and multiphoton microscopy [138, 139].

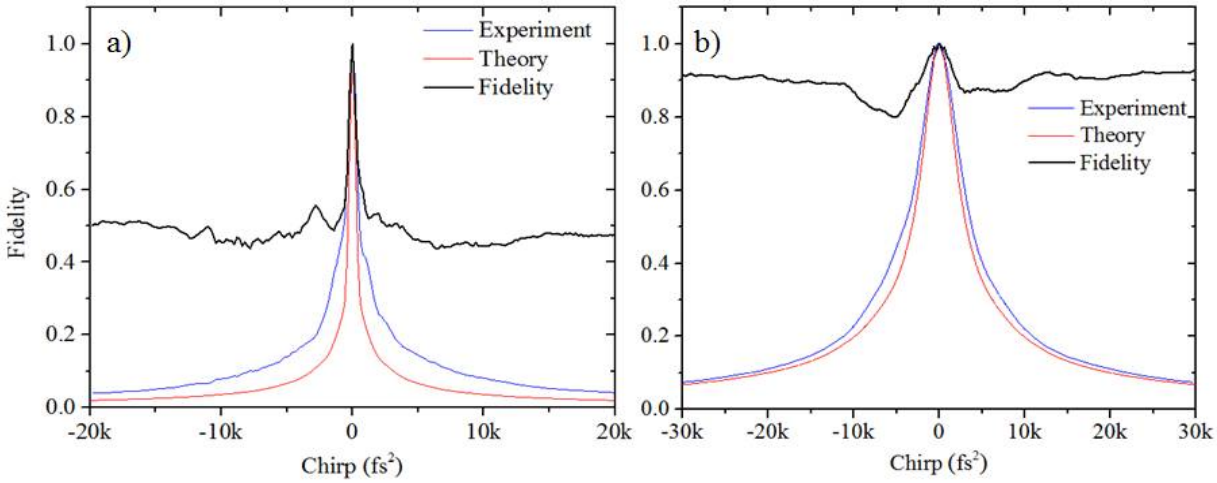

Figure 39. Fidelity measurements for the multi-soliton source after compression obtained (a) for the entire spectrum and (b) for the isolated long-wavelength soliton.

In order to further test the phase stability of the coherently combined multi-soliton output, we scanned the phase of one of the solitions with respect to the rest of the output. The phase of the long-wavelength solition was varied from –2π to 2π using the pulse shaper, in 0.5 rad increments, see Figure 40a. Multiphoton intrapulse interfernce [41, 140] modulates the sum frequency generation signal with complete destructive interference at values of $\pm\pi$ as shown in Figure 40b. The modulation depth, 100% theoretically, indicates a high level of phase coherence between different parts of the spectrum. Detecting the second harmonic signal at the wavelengths corresponding to sum frequency generation, indicated in Figure 40b with blue arrows, resulted in sinusoidal dependence as predicted by theory, see Figures 40c and 40d. In the Figure 40e a sinusoidal phase scan was performed. The spectral phase, $\varphi(\omega) = \alpha \cos\left[\gamma(\omega - \omega_0) - \delta\right]$ was applied by the pulse shaper, where α=2, γ=40 fs and δ was

scanned from 0 to 2π. The equidistant parallel lines are the signatures of TL pulses [17]. For a transform-limited output one can clearly see traces predicted by theory. The reproducibility of the phase scan and MIIPS traces was checked over a day operation of the laser. This behavior confirms good long term phase stability.

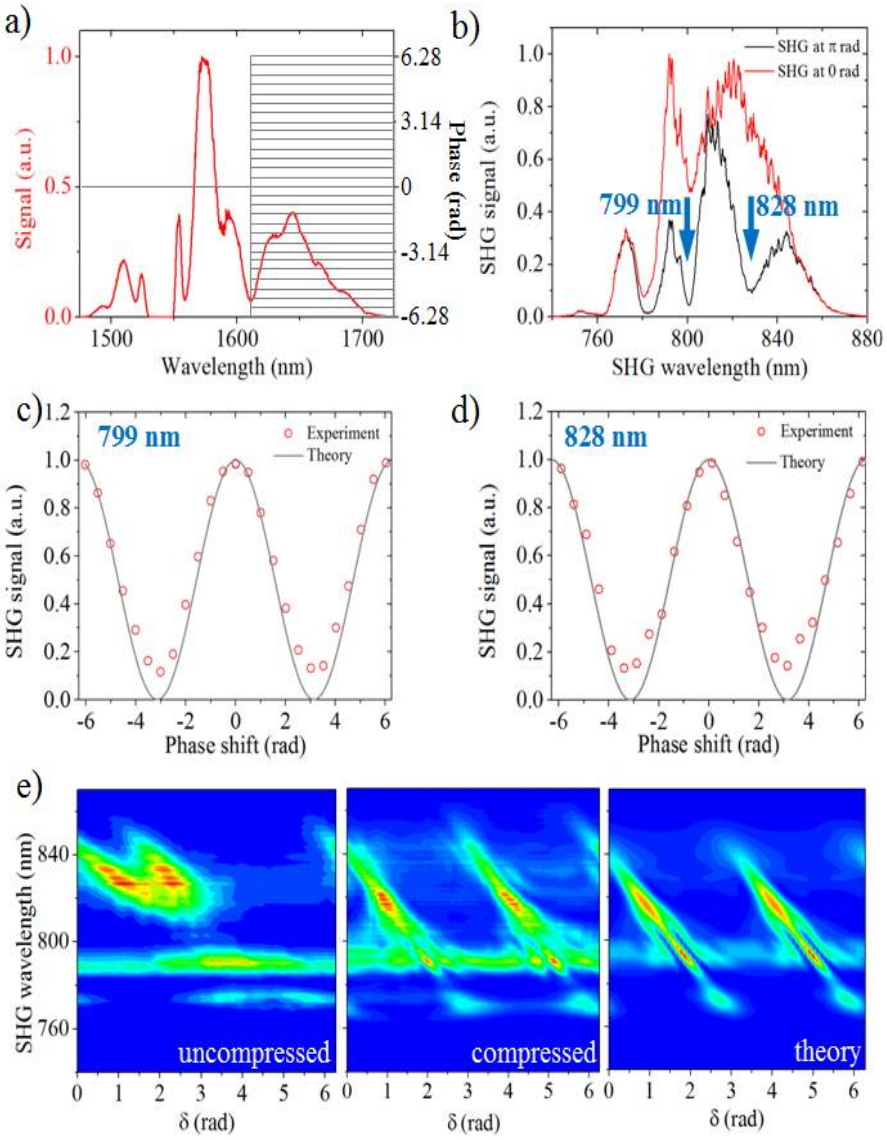

Figure 40. Phase coherence tests of the compressed multi-soliton source. (a) The fundamental spectrum and the phase from –2π to 2π applied to the longest-wavelength soliton. (b) Second harmonic spectra at 0 rad (red) and π rad (black). The arrow shows the wavelengths which appeared due to the sum frequency generation. Normalized experimental and theoretical results from the phase shift scan for 799 nm (c) and 828 nm (d). (e) MIIPS scans for uncompressed, compressed pulses and numerical simulation respectively.

4.2.2 Conclusion

The successful characterization, compression and coherent combining of multiple solitons from a large mode area photonic crystal fiber rod using a MIIPS enabled pulse shaper for two separate laser setups has been reported. Pulses as short as 28 fs were obtained, although in such a case some spectral breathing was identified based on fidelity measurements and degree of coherence simulation. When the long-wavelength soliton was isolated, pulses as short as 57 fs were measured, and these pulses had higher fidelity (coherent and pulse-to-pulse stability properties). The factor of two shorter pulses would result in a factor of 8 or 16 greater signal for third- or fourth-order nonlinear optical processes. The compression scheme used here should work well for two or more soliton-outputs and dispersive waves. We conclude that compression of complex multi-soliton sources offers a path to short pulse generation at wavelengths in the ~1.6-1.8 μm wavelength region where it can be used for non-linear spectroscopic methods such as coherent Raman scattering.

Chapter 5 Measuring and controlling the motion of particles

Physical Chemistry operates at two levels: a molecular level studied by spectroscopic methods and an ensemble level studied by statistical methods and thermodynamics. In real life chemical reactions depend on mixing of gaseous and liquid reagents and happen in a complex environment – in turbulent systems with complex flow of energy and mass. This is a subject for non-equilibrium thermodynamics. Figure 41 illustrates two examples of highly turbulent processes: a vortex pair behind airplane (left panel) and turbulence in a combustion chamber imaged via Laser Induced Fluorescence (right panel) [141].

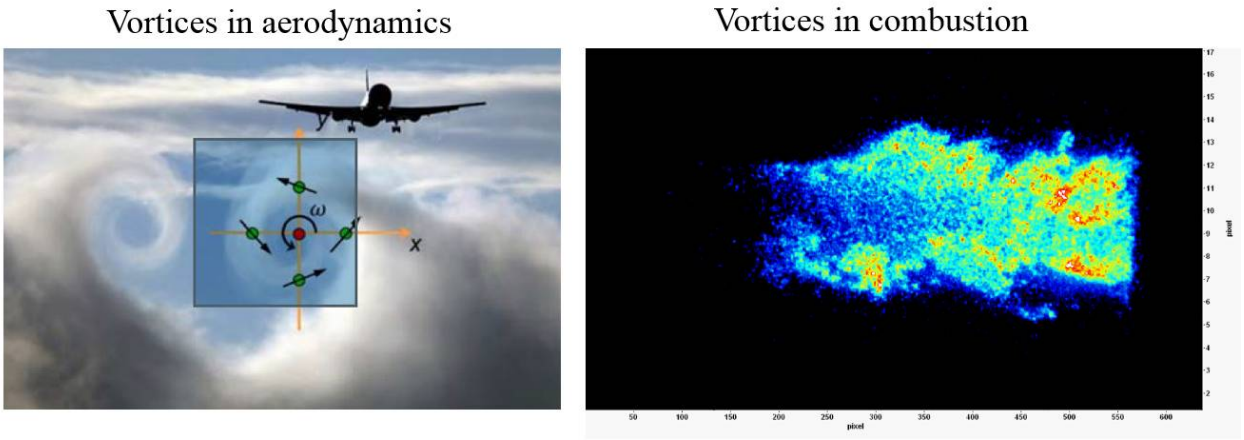

Figure 41. Example of complex fluid flow resulting in formation of vortices.

If one zooms in to a level of a single particle, it can be considered that those processes have similar mechanical dynamics although there is no chemical process with plane. For modeling of these processes, we need to learn how things are behaving at in a very small region of that space. More accurately we measure, better model we can get. In this chapter we discuss problems of measuring and controlling of motion of particles in a fluid. For these projects we had a collaboration with Department of Mechanical Engineering at Michigan State University, because the problem is similar to those they are solving for unsteady fluid mechanics and aerodynamics. The first section of the chapter presents an optical measurements of vorticity. The second one is focused the ability to control that motion and presents interesting results of laser-induced motion. It was suggested by theoretical calculations in Averbukh's research group, that there is a link between rotation of molecules on microscopic level and

subsequent macroscopic rotation due to collisions between molecules [142]. The experimental confirmation is yet to be done, which motivated us to conduct the experiment.

5.1 Fluid flow vorticity measurements

Vorticity is mathematically defined as the curl of the velocity vector, $\Omega = \nabla \times U$, and is physically interpreted as twice the local rotation rate (angular velocity) ω of a fluid particle, i.e. $\Omega = 2\omega$. In a turbulent flow, unsteady vortices of various scales and strengths contribute to the chaotic nature of turbulence. The complexity of the problem led Richard Feynman to state that "Turbulence is the most important unsolved problem of classical physics" [143]. Even though spatially- and temporally-resolved direct measurement of instantaneous vorticity has been a long-held goal, it has proven elusive to date. Currently in all non-intrusive methods, whether particle-based such as Laser Doppler Velocimetry (LDV) and Particle Image Velocimetry (PIV) [144, 145], or molecular-based as in Molecular Tagging Velocimetry (MTV) [146], vorticity is estimated from a number of velocity field measurements at several points near the point of interest, which then allow computation of the velocity derivatives over space. These methods provide a measurement of vorticity that is spatially averaged over the (small) spatial resolution area of each method. The first direct measurement of vorticity was attempted more than three decades ago by measuring the rotation rate of planar mirrors embedded in 25μm transparent spherical beads that were suspended in a refractive-index-matched liquid [147]. The implementation of this method is very complex and requirement of index matching significantly limits its use and prohibits its application in gas (e.g. air) flows. A capability to directly measure vorticity in fluid flows in a non-intrusive time-resolved manner would greatly impact the field of fluid mechanics.

5.1.1. Concept for optical measurements of vorticity

Direct non-intrusive measurement of vorticity requires a laser-based method that is sensitive to rotational motion. Translational velocities can be measured with laser Doppler velocimetry by taking advantage of the (linear) Doppler Effect, which causes a frequency shift when objects move towards or away from a source of light. Analogously, but much less utilized, the Rotational Doppler Effect (RDE)

can be used to measure the angular velocity of a rotating object [148-151]. Measuring with RDE requires the use of Laguerre-Gaussian (LG) light beams that possess orbital angular momentum (OAM), a spatial (azimuthal) modulation of the beam phase front. The creation of beams with arbitrary orbital angular momentum l, or beams having a superposition of counter-rotating OAM ($\pm l$), requires computer controlled 2D spatial light modulators capable of introducing complex phase designs. Figure 42 shows phase masks, imprinted on SLM (left column), and intensity profiles of laser beam reflected of the SLM (right column) for l=2, 4,18.

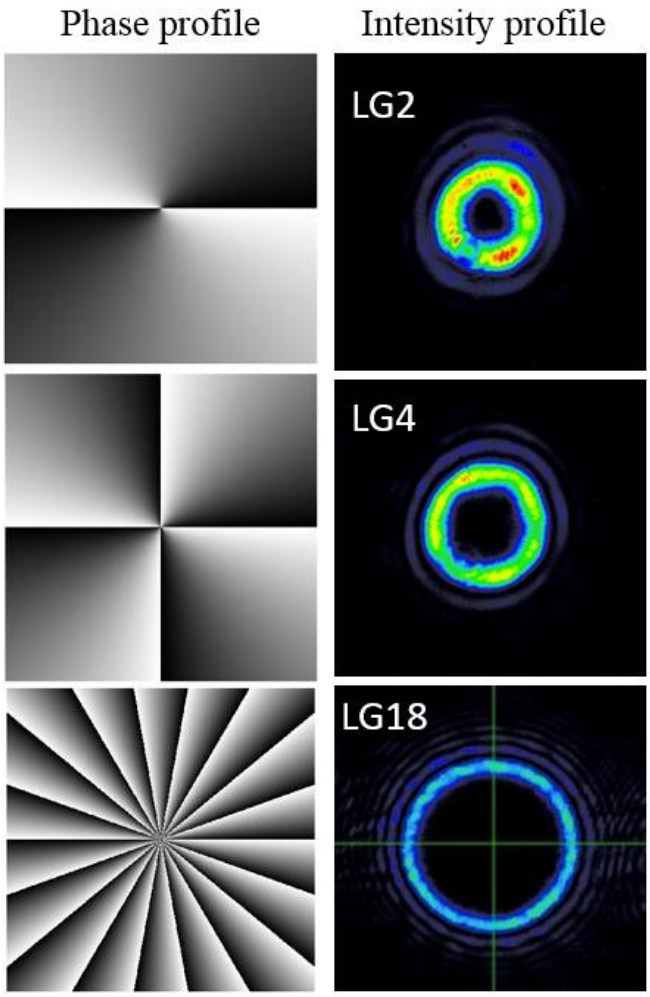

Figure 42. Phase masks and resulted experimentally measured intensity profiles for beams with different OAMs.

The use of LG laser beams with counter-rotating OAM (±*l*) to determine the angular speed of a rotating solid disk based on RDE was recently reported by Lavery et al. [149]. When the illumination comprises two helically phased beams of opposite values of *l*, their scattering into a common detection mode gives opposite frequency shifts resulting in an intensity modulation of frequency $f_{\mathrm{mod}} = 2|l|\omega/2\pi$, where ω is the angular velocity of the rotating object. Lavery et al. [149] tested this type of setup and were able to measure the angular velocity of a spinning disk. Similar concepts have been employed to measure the angular velocity of a microparticle trapped in an optical trap [152, 153]. The idea of measuring flow vorticity with helically phased LG beams has been considered by Belmonte et al. [154], where they tested it on a digital micromirror device but not in a fluid flow.

We present [155] what we believe is the first direct vorticity measurement in a fluid flow based on angular velocity measurement of micron-sized particles free flowing in the fluid using RDE and LG laser beams with OAM. Very small particles faithfully track the fluid flow and, at steady state, they move with the local flow speed and rotate with the local angular velocity of the fluid (or half the local flow vorticity at the particle center) [156]. We demonstrate the technique in a flow field known as solid body rotation or rigid body flow field—for which the angular rotational velocity is uniform and particles carried by the flow also rotate about their center as if they were part of the rigid body. In this type of flow, the vorticity is the same everywhere. We present two sets of experiments. In the first, the signal from a group of 6 μm microparticles is integrated to obtain the average fluid rotation rate about the beam optical axis within a 100 μm illumination region, thus obtaining the spatially-averaged vorticity within that region. In the second experiment, the same information is obtained by measuring the angular velocity of a single 100 μm particle in the flow. The latter is the type of transient measurement required to determine vorticity in more complex flows fields.

5.1.2 Experimental setup

The experimental setup for measurements of the local flow angular velocity and vorticity is shown in Figure 43a. The 488 nm continuous wave beam from an optically pumped semiconductor laser

(Genesis MX, Coherent, USA) with initially Gaussian beam profile is expanded by a telescope (L1, L2) and shaped by a two-dimensional liquid crystal on silicon spatial light modulator (LCOS-SLM, Hamamatsu, Japan). The SLM is programmed with a diffraction pattern that introduces the LG spatial modulation and diffracts the spatially shaped beam as shown in Figure 43b. The shaped beam possesses the orbital angular momentum corresponding to a superposition of LG ±18 modes, and its far-field intensity profile corresponds to a circular periodic structure with 36 petals, see Figure 43c. The use of optical angular momentum in the context of the experiments presented here has been reviewed recently [157]. The beam is then focused with long focal length lens L3 and first diffraction order is selected with an aperture. Lens L4 collimates the beam, which after reflection from dichroic mirror (DM) is focused by lens L5 (60mm focal length) into the center of a rotating cylindrical container with the beam optical axis aligned along the rotation axis. The beam diameter at the focus is measured to be about 100 μm and the average power is 12 mW, an intensity that is at least one order of magnitude too weak for causing laser trapping. The container is filled with fluorescent micro-particles suspended in a density matched solution of water and glycerin (density about 1.05). Two sets of red fluorescent polymer microspheres (Thermo Fisher Scientific Inc.) are used in these measurements, one with 6 μm diameter (15% variance) and the other 100 μm diameter (7% variance). The container cap is fitted with a thin quartz window that touches the liquid surface at all times to eliminate free surface effects. The angular velocity ω of the container is controlled by an optically encoded motor (3501 Optical Chopper, New Focus, USA) rotating at frequency f and angular velocity $\omega = 2\pi f$. Measurements were done after the container was spun for a few minutes to ensure a steady state rotation flow field had been established. The resulting flow field is devoid of any secondary flow and is precisely characterized by the solid-body rotation velocity field $U = r \times \omega$ and its spatially uniform vorticity field $\Omega = 2\omega$.

Backscatter fluorescent light from the irradiated particles is collected with lens L6 and is focused onto a photodiode. A small diameter pinhole is set before photodiode in order to spatially filter out signal from outside of focal volume in fluid. The intensity modulated signal from the fluorescent particles is

recorded at 10 kHz sampling rate and spectrally analyzed. Earlier efforts from our group to detect vorticity based on back scatter resulted in very poor signal to noise ratios due to multiple sources of scatter [158]. The use of fluorescent particles, in combination with clean OAM shaped laser excitation, allows us to reject scattered light from the rotating surfaces of the container and guarantees the measured signal originates from within the rotating body of fluid. The vertical resolution of the measurements presented is estimated to be 2mm, and is determined by the focal length of the lens used and by the iris near the detector.

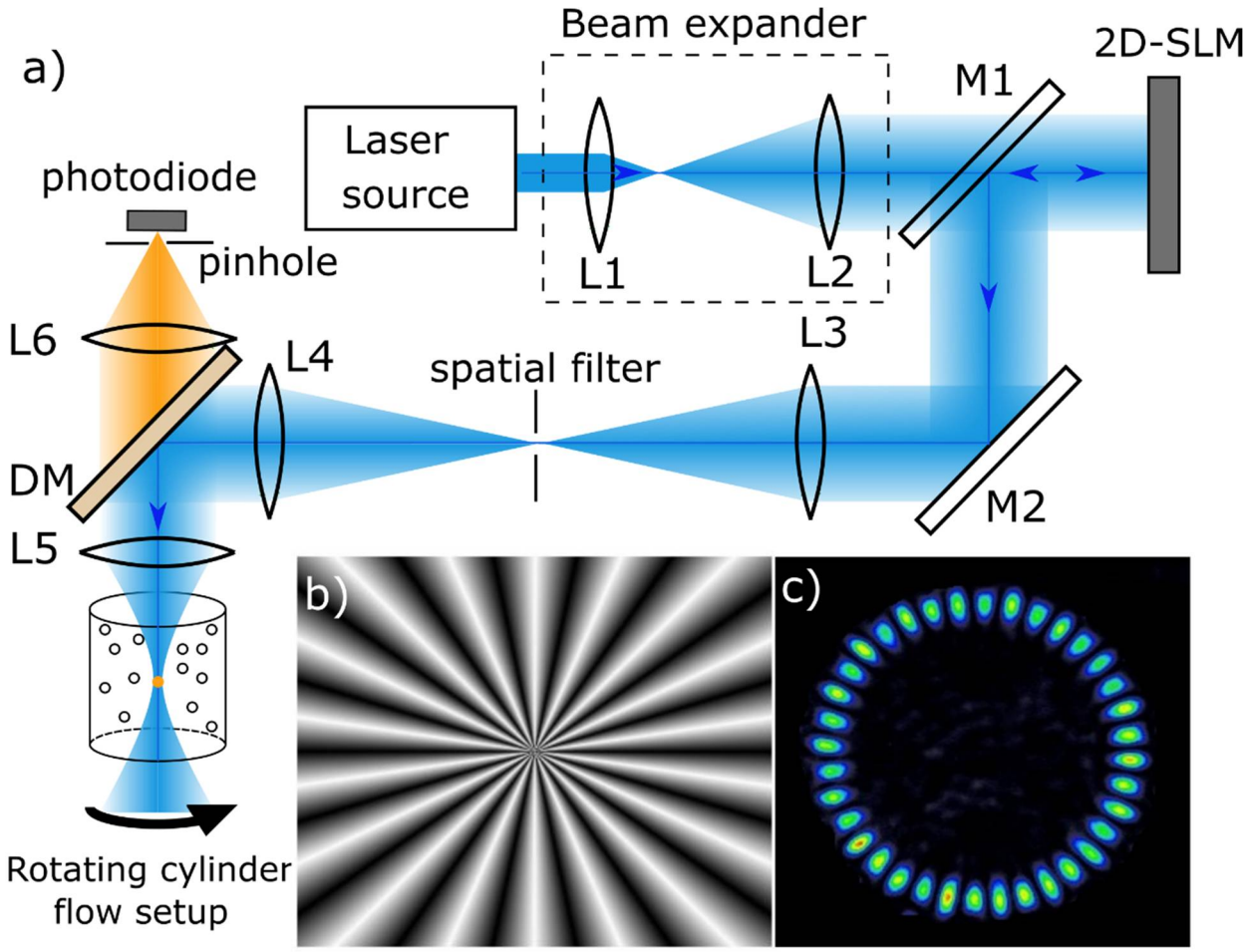

Figure 43. (a) Experimental setup. L1-L6, lenses; M1-M2, mirrors; DM, dichroic mirror. (b) Diffraction pattern generating LG ±18 modes. Actual pattern on 2D SLM included diffraction grating pattern to suppress original Gaussian mode and SLM flatness correction pattern, both not shown here. White color corresponds to 0 phase shift while black corresponds to 2π phase shift with 256 steps in between. (c) Resulting beam structure used to illuminate particles in fluid flow. Figure from [155].

5.1.3 Results and discussion

For the measurements presented, the LG laser beam has an OAM with $l = \pm 18$, resulting in 36 bright features (petals). Scattering from objects rotating at angular velocity ω (or rotation frequency f) leads to intensity modulation at frequency $f_{\text{mod}} = 36\omega/2\pi = 36f$. The first set of data in Figure 44 shows the measurement with 6 μm fluorescent particles, with density about 100 particles per focal volume. In this case, by measuring the rotation rate of an ensemble of particles within the ≈ 100 μm beam diameter we obtain the averaged fluid rotation rate within that region. Figure 44a shows examples of intensity modulation of collected (AC-coupled) signal for four different prescribed rotation frequencies of the cylindrical container. Fourier transforms of each signal provides the spectral information in Figure 44b using a short data record of about 200 ms in length.

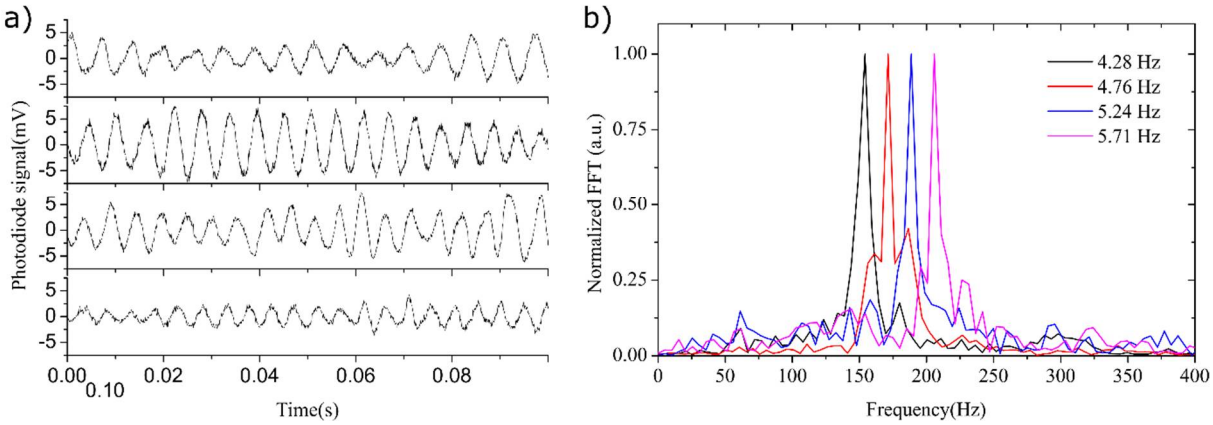

Figure 44. Measurement results for ensemble of particles. (a) 100 ms long time series of collected signal for four different rotation frequencies of the container: f = 4.28 Hz, 4.76 Hz, 5.24 Hz and 5.71 Hz. (b) Power spectrum of the signals in (a) (200 ms data record). Figure from [155].

From the spectral peaks in Figure 44b we measure the modulation frequencies for the four cases to be 154.16±5 Hz, 171.37±5 Hz, 188.58±5 Hz, and 205.76±5 Hz. These values correspond to the measured fluid rotation rates of 4.28±0.14 Hz, 4.76±0.14 Hz, 5.24±0.14 Hz, and 5.72±0.14 Hz, respectively. These values are in excellent agreement with the prescribed rotation frequencies of the rotating fluid container. Accuracy of these measurements is limited by FFT resolution divided by two-times the OAM. For a 200 ms data record and OAM with $l = \pm 18$ we obtain 5/36 = 0.14 Hz. Given the

steady flow field in this experiment, one can improve the measurement accuracy, if desired, by increasing the length of the data record for FFT analysis or increasing the beam's OAM. For arbitrary flows, one could speed up data acquisition to 20 ms, reducing accuracy to 1.4 Hz.

The second set of experiments was carried on with larger 100 μm particles with low particle density in solution to ensure single particle measurement within the ≈ 100 μm beam diameter. This was confirmed by visually observing the single particle presence in the focal volume of structured laser beam based on its intensity time series during data collection. Typical photodiode signal for two different prescribed rotation frequencies of the cylindrical container, f = 4.28 Hz and 4.76 Hz, is presented in Figure 45a. FFT analysis for the signals is presented in Figure 45b. The peaks indicate modulation frequencies of 154.08±5 Hz, and 170.10±5 Hz for these two cases. The corresponding values of the measured fluid rotation rates are 4.28±0.14 Hz, 4.73±0.14 Hz, which are again in excellent agreement with the imposed rotation frequencies of the rotating fluid container.

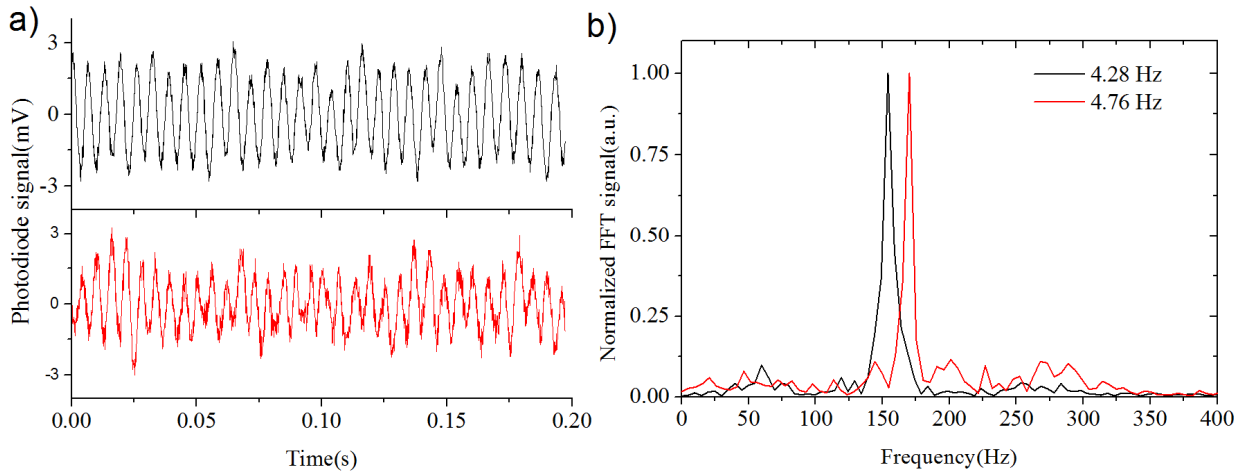

Figure 45. Measurement results for a single of particle. (a) Time series of collected signal for two different rotation frequencies of the cylindrical container: f = 4.28 Hz (top), and 4.76 Hz (bottom). (b) Power spectrum of signals in (a). Figure from [155].

The solid body rotation flow field was selected for these proof-of-concept experiments because it is relatively simple to create and has well-characterized velocity and vorticity fields. When the liquid-filled cylindrical container initially at rest starts to spin, the fluid layer near the moving wall starts to move with the cylinder due to the no-slip viscous boundary condition at the wall. The motion is then

propagated throughout the container by viscous shear until the entire body of liquid rotates at the same speed of the container. The final steady state velocity field is that of solid body rotation with vorticity that is constant in time and uniform in space, with axis parallel to the axis of rotation of cylinder and magnitude equal to twice the cylinder angular velocity. While we have demonstrated here the idea of vorticity measurement using laser beams with OAM in a steady flow environment, clearly most exciting applications would be in unsteady flows. For micro particles in Stokes flow regime, particle rotation time can be estimated from $\tau = \rho_p d^2 / 60\mu$, where ρ_p and d are the particle density and diameter, and μ is the fluid viscosity [159]. For 100 μm particles like those used in our experiment the rotation time is about 100 μsec. Therefore, unsteady vorticity measurements are feasible and could be obtained by acquiring shorter record lengths of data. Because of the quadratic dependence of particle rotation time on diameter, one can select the appropriate particle size to ensure a response time that is faster than the flow-fluctuation time scale. We performed this type of measurement but under steady flow conditions. The time invariant spectral peak (200ms FFT window) in Figure 46 is obtained from a 100 μm particle that lingers within laser illumination at the axis of the rotating container while spinning with the fluid rotation rate. Measuring the spectral peak based on the 40 s data record yields a modulation frequency of 171.5±0.025 Hz, or particle/fluid rotation rate of 4.76 Hz, in perfect agreement with the imposed rotation frequency of the fluid container.

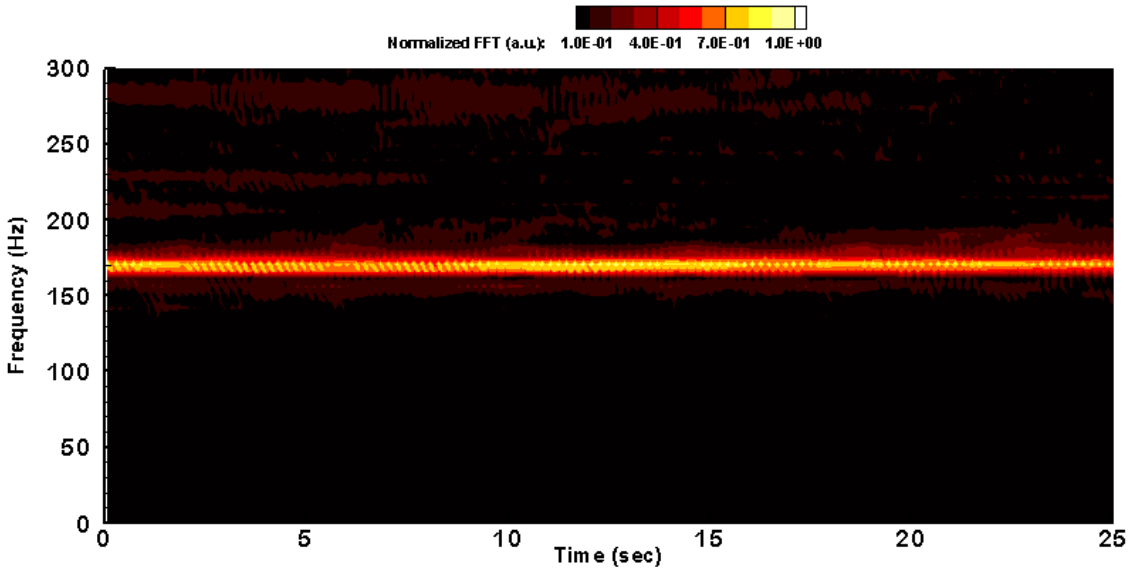

Figure 46. FFT map of signal for a single 100 μm particle in solution over time (f = 4.76 Hz). Figure from [155].

While the experiments we have reported here represent the extension of the work of Lavery et al. [149] to the field of fluid dynamics, there are certain differences between the two as well. In the latter, the scattering signal originates from the planar surface of a spinning disk. In ours, measurements are carried out within the body of the fluid and the scattering signal is from a finite volume inside the fluid. For measurements with high spatial resolution, this scattering volume needs to be localized to a small region. In the current experiments, this was achieved by focusing the laser beam to about 100 μm diameter inside the liquid container.

5.1.4 Conclusion

The first direct and localized non-intrusive measurement of vorticity in a fluid flow using the Rotational Doppler Effect and Laguerre-Gaussian spatially modulated light beams that possess orbital angular momentum has been presented. The approach has been demonstrated in the flow field of solid body rotation where the flow vorticity is known precisely. In one experiment, measurements with a group of 6 μm microparticles is used to obtain the average fluid rotation rate about the beam optical axis within the 100 μm illumination region, and therefore, the spatially-averaged vorticity within. In another experiment, the same information is obtained by measuring the angular velocity of a single 100 μm

particle in the laser beam. In both experiments, the measured results are in excellent agreement with those expected from the prescribed rotation frequencies of the rotating fluid container.

Although, the technique is demonstrated here in a simple flow where vorticity is uniform and steady, the approach holds great promise for unsteady flows with spatially varying vorticity field. It is intended to explore extensions of this measurement technique to more complex flow environments. Part of this effort involves imposing a prescribed rotation rate onto the periodic structure of the beam pattern in the focal volume in order to introduce a bias in the measured frequency and allow the determination of direction of rotation

5.2. Motion induced by laser filamentation

Femtosecond filamentation - whereby self-focusing caused by the optical Kerr effect and defocusing caused by plasma formation are in balance - was discovered approximately twenty years ago [160]. Since then, a significant body of work on this subject has accumulated with excellent reviews available [161, 162]. The unusual properties of femtosecond filaments have led to the suggestion of numerous applications such as LIDAR [163, 164], lightning protection [165], generation of single cycle pulses [166], laser induced breakdown spectroscopy [167], and fluid dynamics measurements [168, 169].

The observation of laser-induced water vapor condensation in the atmosphere and in cloud chambers using the 220 mJ Teramobile laser [170], has inspired field and cloud chamber experiments in which charged species, formed by the laser, were identified as the nucleation agents [171, 172]. Cloud chamber experiments with a 1kHz 2mJ laser source identified an updraft of warm moist air creating vortices perpendicular to the filament ~ 5mm below the laser; the laser-induced flow having a significant effect on water condensation and snow formation [173-175]. In this project we have explored the fluid flow dynamics that ensue in dry air as a result of filamentation with 0.7 mJ pulses at 1kHz. Taking advantage of light-sheet illumination to obtain a cross-section of the fluid flow, we find the formation of pairs of counter-rotating vortices in the wake of the laser filament, which could affect fluid dynamics measurements involving filamentation [168, 169]. The observation [176] is made in the absence of a complicated thermofluids environment involving humid air, an imposed temperature stratification

(bottom plate temperature at -19.5ºC while the temperature in the top was +19ºC), and in the absence of phase changes (condensation) [173-175].

5.2.1 Experimental setup

A schematic of the experimental setup is presented in Figure 47. The output from a 1 kHz regenerative amplifier with 800 nm central wavelength, is focused with a long focal length concave mirror (f = 500 mm). The laser pulses are first characterized and their spectral phase is corrected to near transform limited by using multiphoton intrapulse interference phase scan [177, 178]. The transform limited pulse duration at full-width half-maximum is 40 fs. For all the measurements presented here the average power is set to 700 mW. The beam is focused in air. Glass tubes of two different diameters (4mm and 14mm) and lengths are used to keep room air currents to a minimum. The glass tubes are intersected by a laser sheet, which is created by a CW green laser diode (532 nm) focused by a cylindrical lens. In order to visualize the fluid flow, a small amount of butanol is sprayed in the air near the tube; the butanol mist enters the tube and scattering allows us to see the fluid flow dynamics surrounding the filament taking advantage of Mie scattering. Pictures and video of the fluid dynamics were acquired using a digital single-lens reflex (DSLR) camera set at a 30° angle from the laser direction of prorogation.

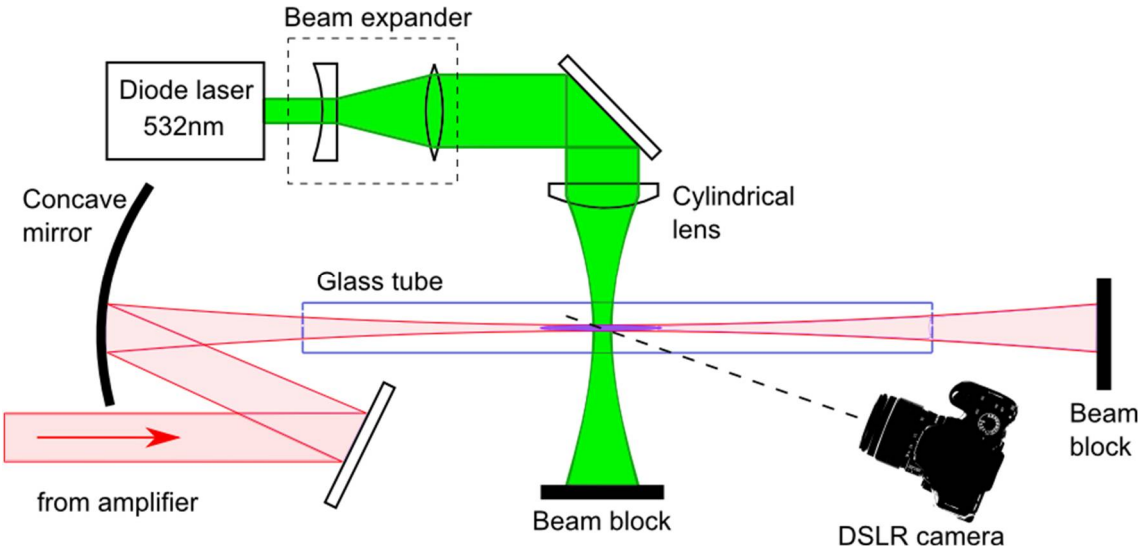

Figure 47. Experimental setup. Green diode laser is used to create a laser sheet in the vertical plane. DSLR camera images green scattered light from seed particles, unveiling the fluid flow resulting from filamentation in a narrow glass tube. Figure from [176].

5.2.2 Results

Results of laser-induced fluid flow are illustrated in Figure 48, obtained with the smaller diameter tube. In these cases, two almost identical vortices (a vortex pair of opposite rotation) are created with symmetry in vertical and horizontal planes. Vortex rotation direction is opposite for right-left or top-bottom. The circular motion with gradually increasing rotational frequency starts when the laser filament is formed. The speed of the rotation is stabilized within a very short period of time (about 1 second) and stays constant all while the filament is present. When the filament is not formed or the laser is blocked, the motion stops completely.

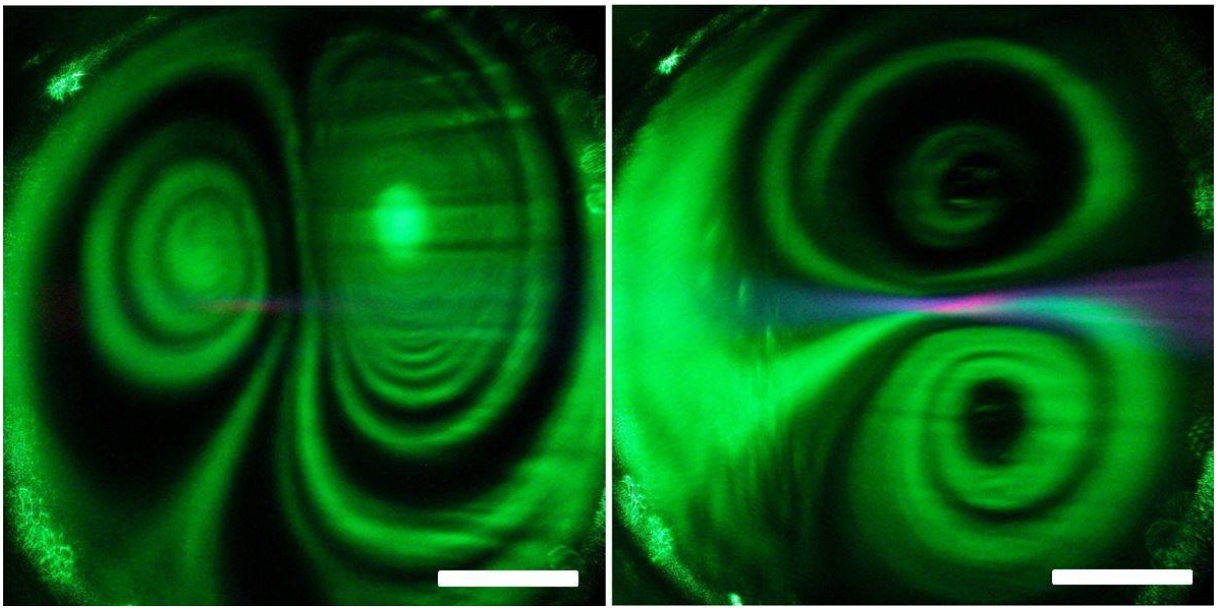

Figure 48. Two different vortex pairs observed in the 4 mm diameter glass tube induced by laser filamentation. The laser filament is observed as a purple hue in the middle of each image. Scale bars are 1 mm. The number of vortices as well as their relative orientation depends on the position of the laser filament relative to the center of the tube. Figure from [176].

The orientation of vortices (Figure 48 left image versus right image) is found to depend on the position of the filament relative to center of the tube. With a slight offset from the central position inside the tube vortices have a preference to form in a certain configuration. For instance, the difference between the two cases illustrated in Figure 48 is the filament is displaced in the vertical direction relative to center

of the tube (left) or in the horizontal direction (right). When the filamentation is closest to with a symmetry axis of the tube other flow arrangements are possible such as – three- and four-vortices.

To study the influence of the tube on the fluid flow dynamics in the wake of laser filamentation we used a tube with a larger inner diameter – 14 mm. All other experimental parameters were kept the same. The result is presented in Figure 49. In this arrangement we observed two counter-rotating vortices with much slower rotation speed, counterclockwise for the left vortex and clockwise for the one on the right.

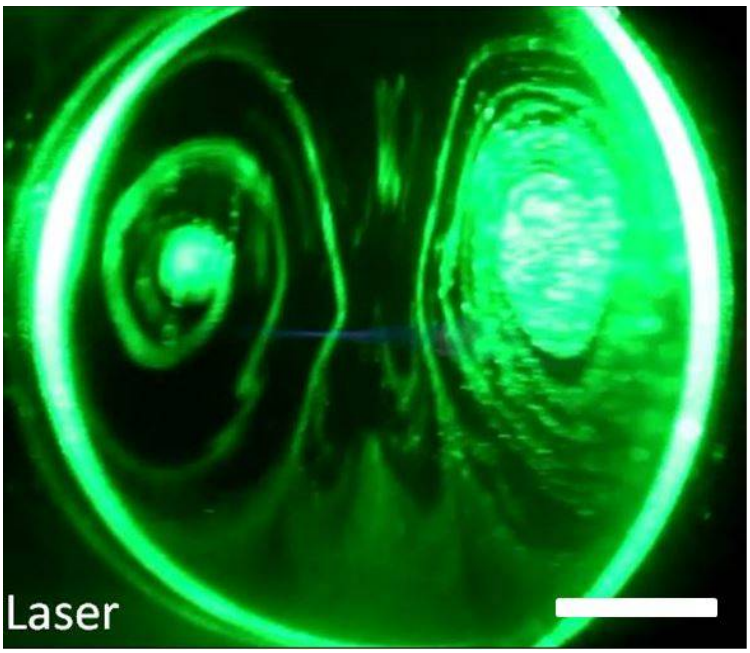

Figure 49. Vortex pair formed in the glass tube with 14 mm in diameter created by laser filamentation. The filament can be observed as a faint purple hue in the middle of the image. The scale bar is 3mm. Figure from [176].

5.2.3 Discussion and implications

Ionization associated with the filament suggests the laser deposits sufficient energy to cause local heating, which then causes convective fluid flow within the confined cylindrical volume. The heat deposited by the laser plasma with estimated local temperature of 3000-5000 K [179] is transferred to gas molecules surrounding the filament, thereby causing gas expansion and creating fluid motion by several possible mechanisms, including radially expanding shock waves and an upward motion for these

molecules due to gravity. When the expanding gas reaches the cylindrical wall of a tube it forms counter-rotating vortices. Despite the high temperatures, the overall heating effect from laser filaments may be neglected when using low repetition rate sources [170-172], but becomes significant when using kHz laser sources [173-175].

To test the buoyancy-generated flow hypothesis, we replaced the laser filament by a resistance wire diameter of 0.45 mm at the center of a 14-mm tube. When the wire is heated the temperature gradient in the gas creates vortices identical to those created by laser, see Figure 50. When the temperature of the wire reaches 150°C, the rate of rotation in the vortices matches that of the laser induced vortices. This measurement gives us a sense of the local macroscopic heating caused by the laser filament. In some cases, we see more complex vortex pairs (not shown) that are not explained by the simple buoyancy hypothesis. We plan to evaluate if those cases are related to multi-filament formation.

Our findings are complementary to cloud-chamber measurements of laser-filamentation-induced condensation and snow formation [170, 173]. Condensation was found to result from the creation of plasma generated nucleating agents [170], and particle growth is enhanced by laser-induced motion of air flow [173, 175]. Cloud chamber measurements and associated simulations under high humidity and near a cold plate visualized the formation of a vortex formed a few millimeters below the filament [175]. The light-sheet illumination experiments presented here on dry air capture the formation of vortex pairs along the filament. These findings support the fact that heating by the filament cannot be neglected and affects fluid flow, even in the absence of temperature stratification and condensation.

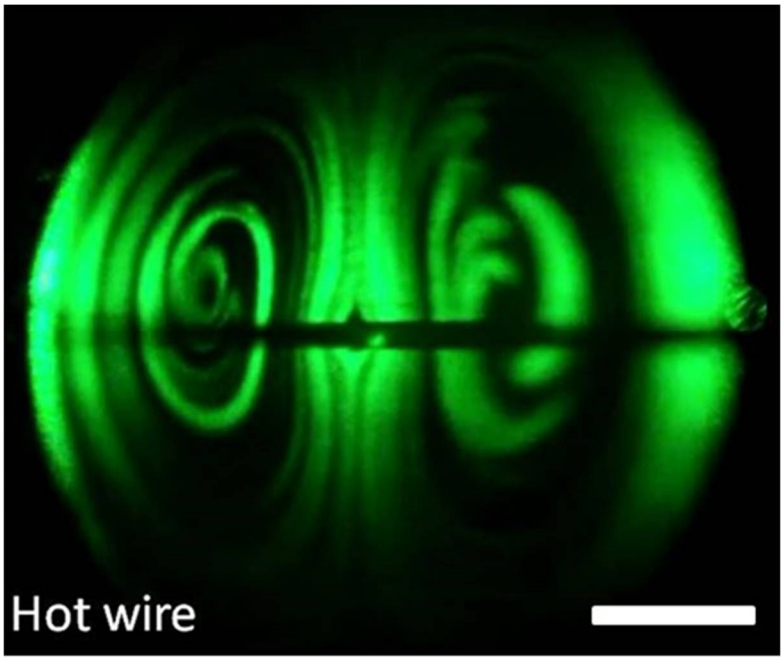

Figure 50. Vortex pair formed in the glass tube with 14 mm in diameter created by a hot resistance wire, which casts a horizontal shadow. The temperature of the wire was adjusted to match the period of rotation of the laser-induced vortices. The scale bar is 3mm. Figure from [176].

The measurements presented here are useful for implementation of applications based on laser filaments. For single pulse applications, the laser experiences no distortion from local heating as it propagates. However, the fluid flow dynamics in the wake of the pulse are disturbed by local heating. We are aware of one type of measurement whereby a femtosecond laser excites the excited B-state of nitrogen, and the emission is used to achieve molecular tagging velocimetry [146] for fluid dynamics studies in air [168]. Findings of local heating introduced by a filament and the changes in fluid dynamics surrounding the filament suggest that MTV experiments need to take these effects into account and care must be exercised in the interpretation of results. Conversely, the findings reported here indicate filaments can be used to affect fluid flow dynamics remotely.

5.2.4 Conclusion

The experimental observation of fluid flow caused by propagation of femtosecond filaments in dry air is presented. Significant flow disturbance comprising multiple vortices has been observed. We hypothesize that the nature of this fluid flow arises from gas expanding of the heated region created by the

plasma associated with filamentation. Convection processes and the constrained volume force the gas to form vortices. This hypothesis has been tested with a heated wire placed in the tube instead of laser beam, and the observed vortex formation was very similar to the laser-induced one. These findings confirm the importance of heat flux from filaments and the resulting fluid flow, a result relevant to applications of filaments for molecular tagging velocimetry, condensation and in general for the use of high-repetition rate sources where the medium does not renew fast enough and subsequent pulses travel in areas with increasing thermal energy. The analysis presented explains the simplest case of a single pair of vortices induced by an updraft caused by thermal buoyancy. Under certain conditions of intense laser excitation and confinement more complicated fluid flow is observed. It is planned to explore the higher energy regime, and different chamber configurations using axial as well as transverse light sheet illumination.

Chapter 6 Summary and outlook

This chapter summarizes the work and results presented in this dissertation. The topics I worked on included pulse shaping (real-time femtosecond pulse correction and dispersion compensation using an additional laser pulse), understanding laser self-action processes and their mitigation using binary phase shaping, designing two laser sources for spectroscopic applications, and fluid and air flow studies.

6.1 Pulse shaping: new methods of pulse stabilization and laser-induced dispersion control

The sensitivity of the second-harmonic generation signal to the spectral phase of a femtosecond pulse through multi-photon intrapulse interference plays a key role in many pulse characterization and compression techniques. In the RT-MIIPS method we used the well-understood and predictable response of the SHG signal to spectral phase fluctuations for second- and third- order phase dispersion in order to measure those fluctuations. By narrowing the SHG signal and tracking the position of its peak, we can accurately measure the SOD and TOD of pulses in real-time, in what is essentially a single-shot manner. The results were demonstrated on different laser systems and confirmed the stability of the laser parameters. Long-term automatic peak power stabilization opens up possibilities for long-term experiments, where measurements can be free from errors due to drifts in the phase and amplitude of laser pulses. The single-shot nature of this method allowed us to study laser-induced dispersion in fused silica and develop an optical method for pulse dispersion control.

In some situations, the use of conventional dispersion control methods, like prisms and grating compressors, is not feasible due to their bulky dimensions, high losses or challenging wavelengths of interest. We have developed an all-optical method for controlling the dispersion of femtosecond pulses using another intense pulse and the cross-phase modulation effect in fused silica. The experimental results show that the dispersion can be controlled in the range of hundreds of fs^2, which corresponds to the chromatic dispersion of a few centimeters of optical glass.

6.2 Laser self-action and its mitigation

In many optical setups for photochemical experiments, a femtosecond pulse travels through optically transparent media before it reaches a sample. This media could be a cuvette wall for a liquid sample or a window in a vacuum chamber, and it can introduce a phase shift in the laser pulse that alters its shape and spectroscopic properties. When the thickness and the refractive index of a material are known, the chromatic dispersion introduced by the media can be calculated and either corrected for using a pulse compressor or taken into account during data processing and analysis. For intense laser pulses, the non-linear refractive index starts to play an important role and leads to laser-induced dispersion. We studied the effect of self-phase modulation and related to it laser-induced dispersion for femtosecond pulses propagated in fused silica. For transform-limited pulses and positively-chirped pulses, the effects we measured were in very good agreement with theory. In contrast, the surprising and anomalous dispersions observed in negatively pre-chirped pulses cannot be simply explained by optical Kerr effect theory. We speculate that for negatively chirped pulses, the energy transfer from high-frequencies to low frequencies, caused by the non-instantaneous response of the medium, is responsible for this anomalous effect. The finding is extremely important because it highlights not only the magnitude of the expected dispersion but also its sign, which without proper acknowledgement, could lead to inaccurate results in a photochemical experiment.

In most applications, phase distortions introduced by propagation media have negative effects on laser system performance. These include pulse degradation due to spectral modulation, breakage of pulses into trains of pulses, self-focusing, and destruction of optics. In this work, we have studied mitigation of self-action processes, including self-focusing and self-phase modulation, using binary shaping of the spectral phase. We applied a spectral phase consisting of zeros and π-s and measured the amount of pulse degradation following propagation through a fused silica window. We studied the relationship between the way the phase mitigates phase distortion and decreases peak power of a laser pulse. We studied a few thousands of phases with different number of elements, both numerically and experimentally, and found that the efficiency of self-action mitigation for binary phase shaping is proportional to the number of

elements in the phase. For instance, to attenuate a pulse by a factor of 1000 (a minimum requirement for viable chirp pulse amplification), the phase mask requires 1400 elements. A phase mask can be a fixed-phase plate or a programmable SLM, but in both cases, it is completely reversible—after passing through the same mask, the light is restored to its original pulse shape. The task of finding the optimal phase mask for arbitrary number of elements is a highly non-trivial task. We also addressed this problem and provided insights into the solution by taking advantage of the symmetries of the search space and its fractal properties.

6.3 Laser systems for specific spectroscopic applications

We developed two broadband laser systems with a particular emphasis on spectroscopic applications. Both systems have specific advantages.

The first system has an especially unique design. The main feature distinguishing it from conventional "classical" lasers, which have a cavity, a gain media, and a mode-locking mechanism, is that the ultrashort pulse generation is based on a cascaded four-wave mixing process in a highly nonlinear optical fiber. The straightforward all-fiber "in-line" design, without bulk optics, makes this turnkey laser very robust, stable and maintenance-free. This type of laser is related to frequency comb lasers. The bandwidth the laser produces consists of multiple extremely narrow spectral lines centered at 1550 nm. The spacing between lines, defined and controlled by electronics, is on the order of a few nanometers, which makes each line distinguishable and measurable by an optical spectrum analyzer. This is a big advantage for spectroscopic applications, which require precise and accurate information on the positions and magnitudes of spectral components. The bandwidth was found to be coherent experimentally, to produce sub-45 fs pulses. A spectral phase correction, performed with a pulse shaper, was necessary to compress pulses to a transform-limited pulse duration. It is worth noting, that since second-order dispersion was found to be the main component in the phase corrections, a simple grating-based compressor can be used. Finally, the use of off-the-shelf telecom components and fibers reduced both the cost and size of the source, which along with its robustness, makes it suitable for use outside of a research laboratory.

The second system is based on bandwidth broadening in photonic crystal fibers via the soliton fission process and soliton self-frequency shift. These allow pulses from a commercial fiber-laser amplifier to be compressed from 500 fs to 30 fs, with corresponding bandwidth broadening from 15 nm to >300 nm in the 1600 nm region. The challenge in this work was in the multi-pulse nature of the generated light: the output of the fiber is a train of pulses with different wavelengths, spectral amplitudes and phases, and with pulse separations of hundreds of femtoseconds. Compressing each pulse and them coherently combining them using a MIIPS-enabled pulse shaper resulted in a single ultrafast broadband pulse. The compressed source was found to have good coherence and phase stability, though fidelity measurements did indicate moderate spectral breathing. The system has potential applications in nonlinear spectroscopy and multi-photon deep-tissue imaging.

6.4 Fluid flow: measurements with spatially shaped laser beams and creation with intense laser

The problem of measuring a fluid flow is of great interest in research areas dealing with complex turbid media, such as aerodynamics, combustion processes and chemical reactors. One of the most important flow parameters, vorticity, is usually computed by post processing video recording, but this limits both time and spatial resolutions. In this work, we presented the first optical measurements of vorticity in real flows with 100-micron resolution. The studies were conducted on fluorescent micron-size spheres suspended in a density-matching liquid in a steady-state flow. We used a 488 nm laser with an optical angular momentum, generated using a phase mask on 2D SLM, that is sensitive to rotation. Spectral analysis of the intensity modulation of the fluorescent signals from the particles revealed the rotational frequency. The measurements for an ensemble of 6 μm particles and a single 100 μm particle were in very good agreement with expected values.

As the first step toward inducing and controlling the macroscopic motion of molecules in the gas phase with optical pulses, we conducted an experimental study of air flow under intense laser radiation. A laser filamentation, a few centimeters-long region of ionized medium and plasma contained in a micron diameter light channel, was created by focusing 0.7 mJ laser pulses with a long focal length lens in air. The filament was surrounded by a glass tube to shield the interaction region from the ambient air flow.

We used laser-sheet side illumination with a green laser on highly scattering aerosol-like particles to observe and record the formation of pairs of vortices. We related the motion to a temperature gradient originating from hot plasma electrons. The geometry of the flow, namely the number of vortices and their direction of their rotation, can be explained by updraft motion of heated air molecules inside the confined volume of the tube. The hypothesis was tested by replacing the filamentation with a heated metal wire. The resulting flow was very similar to that induced by the laser, which confirmed the hypothesis. The finding indicates the importance of heat flux from filaments and the resulting fluid flow for applications with high-repetition rate lasers where the media does not quickly recover and subsequent pulses travel in areas with increasing thermal energy.

APPENDICES

Appendix-I Matlab code for generating binary phases and searching for an optimal solution

The following code generates a set of *n*-bit binary spectral phases, calculates peak power for each of them for a 38 fs pulse and plots the results in *m* by *m* matrix, where *m*=sqrt(2^*n*). The code assumes 600-pixel pulse shaper and Gaussian shape spectrum. The result for *n*=14 is shown in Figure 23.

```
%% initialize
clc;
clear all;
reverseStr = '';
c=3*10^8;%m/s

%% Time and frequency axis setup
T=20000; %fs
nt=2^12;
dt=T/nt;                        % timestep (dt)
t=(-nt/2:1:nt/2-1)'*dt;             % time vector
w=2*pi*(-nt/2:1:nt/2-1)'/(dt*nt);
w_min=min(w);
w_max=max(w);
%lambda0=800; %central wavelength in m, 800nm
%w0=2*pi*c/lambda0;
%lambda=2*pi*3e2./(w+2*pi*3e2/lambda0);
dw=abs(w(1)-w(2));

%% Laser pulse parameters
tau=38; % initial pulse duration, FWHM of intensity, fs
tau0=tau/2/log(2)^0.5; %pulse duration for calcs, fs
u0=1*exp(-1/2*(t/tau0).^2); %pulse in time
spec0=fftshift(ifft(fftshift(u0)))*dt;  %spectrum of intial pulse

%% Phases setup
nbits=14;     %number of bits in phase
nphases=2^nbits;%number of phases for current bit number
ncarpet=sqrt(nphases);

%% setting up phase range on spectrum
Th=0.005; % threshold for binary phase range
BW=find(abs(spec0).^2>Th*max(abs(spec0).^2));
npxlsBW=length(BW);    %number of points within spectrum range
w_BWmin=w(BW(1));
w_BWmax=w(BW(length(BW)));
% PXLS division
npxls_ideal=600;
npxlsperbit=ceil(npxls_ideal/nbits);
npxls_real=npxlsperbit*nbits;
% New w axis
dw_new=(w_BWmax-w_BWmin)/(npxls_real-1);
w_BW=(w_BWmin:dw_new:w_BWmax)';
```

```
nw_ext=(w_BWmin-w_min)/dw_new;
w_postBW=(w_BWmax+dw_new:dw_new:w_BWmax+nw_ext*dw_new)';
w_preBW=(w_BWmin-dw_new*(nw_ext-1):dw_new:w_BWmin)';
w_new=cat(1,w_preBW,w_BW,w_postBW);
nt_new=length(w_new);
% New t axis
dt_new=2*pi/(dw_new*nt_new);                % step in time domain
t=(-nt_new/2:1:nt_new/2-1)'*dt_new;          % time vector
% Interpolation on new w axis
spec0=interp1(w,spec0,w_new,'spline');
u0=fftshift(fft(fftshift(spec0)))*1/dt;  %intial pulse interpolated

%% Initializing arrays for main loop
phi_BW=zeros(length(w_BW),1);   % creates empty array for phase within spectrum
phi_pre=zeros(length(w_preBW),1); %creates zeros before spectrum
phi_post=zeros(length(w_postBW),1); %creates zeros after the spectrum
smallest=1;
allresults=zeros(nphases,1);

%% Main loop
tic;
for i=1:nphases
      phi_ref=dec2bin(i-1,nbits)'=='1'; %generates phase combination
        for j=1:nbits
            phi_BW(npxls_real/nbits*(j-1)+1:npxls_real/nbits*j)=phi_ref(j);
        end
      phi=cat(1,phi_pre,phi_BW,phi_post);
      phi=phi.*pi;
      spec=spec0.*exp(-1i*phi);
      u=fftshift(fft(fftshift(spec)))*1/dt;
      current_peak=max(abs(u).^2./max(abs(u0).^2));
      allresults(i,:)=current_peak;
      if current_peak<smallest
         smallest=current_peak;
         smallest_phi_ref=phi_ref;
         %-----------------
         phi_ref2=dec2bin(i-1,nbits);
         half1=phi_ref2(1:nbits/2);
         half2=phi_ref2(nbits/2+1:nbits);
         y1=bin2dec(fliplr(half1))+1;
         x1=bin2dec(half2)+1;
         %------------------
         peak_coordinates=[y1 x1];
      else
         smallest=smallest;
      end
%%
       figure(1)
       subplot(1,2,1);
        plot(w_new,abs(spec0).^2./max(abs(spec0).^2),w_new,phi.*0.5./pi);
        title(['#Phase= ',num2str(i)]);
```

```
        xlim([-0.1 0.1]);
        ylim([0 1.1]);
        subplot(1,2,2);
        plot(t,abs(u).^2./max(abs(u0).^2),t,abs(u0).^2./max(abs(u0).^2));
        xlim([-200 200]);
        ylim([0 1.1]);
        pause(1);
  percentDone = 100 * i / nphases;
  msg = sprintf('Percent done: %3.1f', percentDone);
  fprintf([reverseStr, msg]);
  reverseStr = repmat(sprintf('\b'), 1, length(msg));
end
toc;
 figure(2)
 plot(w_new,abs(spec0).^2./max(abs(spec0).^2),w_new,smallest_phi.*0.5./pi);
 title(['Smallest peak= ',num2str(smallest)]);
 xlim([-0.12 0.12]);
 ylim([0 1.1]);
figure(3)
plot(1:nphases, sort(allresults))
```

For bit number more than 25 computational cost makes it impractical to evaluate all phases in a set. We used a pseudo-random generation of phases to test bit numbers above 25. Figure 51 shows a 3D representation of a 12-bit set of binary phases to illustrate the algorithm of phase selection. The first phase is picked randomly and peak power is calculated. Then 8 adjacent phases are also evaluated and peak power for each phase is compared. If peak intensity for any of the phases is lower than the peak intensity of the original first phase, then the algorithm keeps searching around that phase to find a local minimum of peak power (dark blue valleys in Figure 51). When peak power can no longer be reduced by moving to adjacent phases, the local minimum is recorded and the algorithms starts over with another random start phase. After a number of local minima are obtained, they are compared to each other to yield the global minimum.

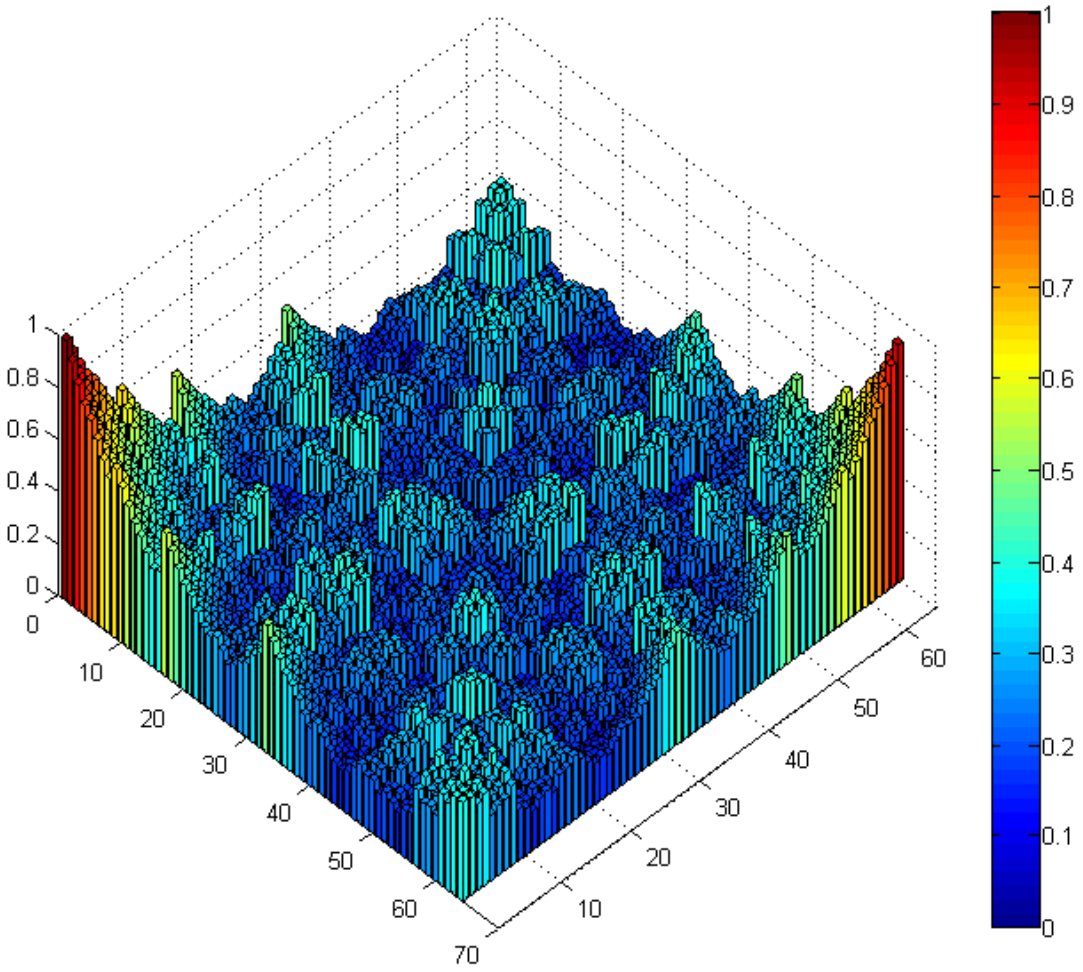

Figure 51. 3D plot of pulse intensities normalized on TL pulse intensity for 12-bit binary phases (64 by 64 matrix). Red color corresponds to high peak intensities; blue color corresponds to a good attenuation.

A Matlab code of the pseudo random search algorithm is following:

```
clc;
clear all;
reverseStr = '';
c=3*10^8;%m/s
T=65000; %fs
nt=2^14;

nbits=50; %number of bits in phase
nsites=10000; %number of phases for current bit number
%% Axis setup
dt=T/nt;                        % timestep (dt)
t=(-nt/2:1:nt/2-1)'*dt;             % time vector
w=2*pi*(-nt/2:1:nt/2-1)'/(dt*nt);
w_min=min(w);
```

```
w_max=max(w);
dw=abs(w(1)-w(2));
tau=38; % initial pulse duration, FWHM of intensity, fs
tau0=tau/2/log(2)^0.5; %pulse duration for calcs, fs
u0=1*exp(-1/2*(t/tau0).^2); %pulse in time
spec0=fftshift(ifft(fftshift(u0)))*dt;  %spectrum of intial pulse
Th=0.005; % threshold for binary phase range
BW=find(abs(spec0).^2>Th*max(abs(spec0).^2));
npxlsBW=length(BW);  %number of points within spectrum range
w_BWmin=w(BW(1));
w_BWmax=w(BW(length(BW)));
npxlsperbit=round(npxlsBW/nbits);
npxls_real=npxlsperbit*nbits;
phi_BW=zeros(npxls_real,1);              % creates empty array for phase within spectrum
phi_pre=zeros(BW(1),1);                 %creates zeros before spectrum
phi_post=zeros(length(w)-length(phi_BW)-length(phi_pre),1); %creates zeros after the spectrum
% phi_ref=zeros(nbits,1);
phi_random=zeros(nbits,1);

%% Main loop
global_min=1;
pulse=0;
a=0;
count=0;
k=0;
v=0;
stop=0;
tic;
for i=1:nsites
   a=a+1;
%    a
   for n=1:nbits %generates RANDOM phase
      phi_random(n,:)=round(rand(1));
   end
   phi_center=phi_random;
   stop=0;
   area_min=1;
   while stop==0;
      k=k+1;
%       k
      phi_neigbors=gen8numbers_around_Gaus(phi_center); %Generates 8 neighbors around initial phase
      local_min=1;
      for m=1:9 %calculates peak intensity for each of 9 phases
         count=count+1;
%          c
         for j=1:nbits % remaos a phase on 600 pxls
            phi_single=phi_neigbors(:,m);
            phi_BW(npxls_real/nbits*(j-1)+1:npxls_real/nbits*j)=phi_single(j);
         end
         phi=cat(1,phi_pre,phi_BW,phi_post);
         phi=phi.*pi;
```

```
            spec=spec0.*exp(-1i*phi);
            u=fftshift(fft(fftshift(spec)))*1/dt;
            current_peak=max(abs(u).^2./max(abs(u0).^2));
            if current_peak<local_min
               local_min=current_peak;
               local_u=u;
               local_phi=phi;
               local_phi_short=phi_single;
               phi_center=phi_single;
            end
         end
         if local_min<area_min;
            area_min=local_min;
            area_u=local_u;
            area_phi=local_phi;
            area_phi_short=local_phi_short;
            stop=0;
         else stop=1;
         end
         continue
      end
      if area_min<global_min;
         global_min=area_min;
         global_u=area_u;
         global_phi=area_phi;
         global_phi_short=area_phi_short;
      end
end
toc;
eltime=toc;
nbits
nsites
global_min
final_pulse=abs(global_u).^2./max(abs(u0).^2);
spectrum=abs(spec0).^2./max(abs(spec0).^2);
waxis=w;
taxis=t;
% k
count
%% Plot
figure(2)
subplot(2,1,1);
% plot(w,abs(spec0).^2./max(abs(spec0).^2),w,global_phi.*0.5./pi, w,SquareSpex);
plot(w,abs(spec0).^2./max(abs(spec0).^2),w,global_phi.*0.5./pi);
title('Spectrum and induced binary phase');
xlabel('angular frequency, w-w0, fs^-1');
ylabel('normalized intensity, arb.u.');
xlim([-0.15 0.15]);
ylim([0 1.1]);
subplot(2,1,2);
plot(t./1000,abs(global_u).^2./max(abs(u0).^2));
```

```
title(['Pulse with induced phase.  Peak power ratio to TL= ',num2str(global_min)]);
xlabel('time, ps');
ylabel('peak power/peak power TL, arb.u.');
xlim([-25 25]);
ylim([0 0.01]);
```

Functions to generate coordinates of 8 adjacent phases:

```
function out=gen8numbers_around_Gaus(array)
n=length(array);
firsthalf=array(1:n/2);
secondhalf=array(n/2+1:n);
n_center=array;
n_east=cat(1,firsthalf,bi_plus_one(secondhalf));
n_north=cat(1,bi_plus_one_Gaus(firsthalf),secondhalf);
n_northeast=cat(1,bi_plus_one_Gaus(firsthalf),bi_plus_one(secondhalf));
n_west=cat(1,firsthalf,bi_minus_one(secondhalf));
n_south=cat(1,bi_minus_one_Gaus(firsthalf),secondhalf);
n_southwest=cat(1,bi_minus_one_Gaus(firsthalf),bi_minus_one(secondhalf));
n_northwest=cat(1,bi_plus_one_Gaus(firsthalf),bi_minus_one(secondhalf));
n_southeast=cat(1,bi_minus_one_Gaus(firsthalf),bi_plus_one(secondhalf));
out=cat(2,n_center,n_east,n_north,n_northeast,n_west,n_south,n_southwest,n_northwest,n_southeast);
end
function out=bi_plus_one_Gaus(array) % fliplr if row vector
% and flipud if column vector
a=array;
i=find(a==0, 1, 'first');
a(i)=1;
a(1:i-1)=0;
% out=a;
out=a;
end
function out=bi_minus_one_Gaus(array) % fliplr if row vector
% and flipud if column vector
a=array;
i=find(a==1, 1, 'first');
a(i)=0;
a(1:i-1)=1;
out=a;
end
```

Appendix-II List of publications

1. G. Rasskazov, A. Ryabtsev, D. Pestov, B. Nie, V.V. Lozovoy and M. Dantus, "Anomalous laser-induced group velocity dispersion in fused silica", Opt. Express **21**, 17695 (2013).
2. A. Ryabtsev, B. Nie and M. Dantus, "45 fs optical pulses from phase corrected broadband cascaded four wave mixing products", Laser Phys. Lett. **10**, 125109 (2013).
3. D. Pestov, A. Ryabtsev, G. Rasskazov, V.V. Lozovoy, and M. Dantus, "Real-time single-shot measurement and correction of pulse phase and amplitude for ultrafast lasers," Opt. Eng. **53**, 051511 (2014).
4. G. Rasskazov, A. Ryabtsev, V.V. Lozovoy and M. Dantus, "Laser-induced dispersion control," Opt. Lett. **39,** 3208 (2014).
5. A. Ryabtsev, S. Pouya, M. Koochesfahani, and M. Dantus, "Vortices in the wake of a femtosecond laser filament," Opt. Express **22**, 26098 (2014).
6. V.V. Lozovoy, G. Rasskazov, A. Ryabtsev, and M. Dantus, "Phase-only synthesis of ultrafast stretched square pulses," Opt. Express **23**, 27105 (2015).
7. G. Rasskazov, A. Ryabtsev, V.V. Lozovoy, and M. Dantus, "Mitigating self-action processes with chirp or binary phase shaping," Opt. Lett. **41**, 131 (2016).
8. A. Ryabtsev, S. Pouya, A. Safaripour, M. Koochesfahani, and M. Dantus, "Fluid flow vorticity measurement using laser beams with orbital angular momentum," Opt. Express **24**, 11762 (2016).
9. G. Rasskazov, A. Ryabtsev, K. Charan, T. Wang, C. Xu and M. Dantus, "Characterization and adaptive compression of a multi-soliton laser source", *submitted to Opt. Express*.
10. G. Rasskazov, A. Ryabtsev and M. Dantus, "Eye-Safe Near-Infrared Trace Explosives Detection and Imaging", *submitted to JACS*.
11. G. Rasskazov, A. Ryabtsev, D. Pestov, V. V. Lozovoy and M. Dantus, "Kerr effect induced transient group-velocity dispersion of fused silica measured via real-time MIIPS and spectral interferometry," *Lasers and Electro-Optics Europe (CLEO EUROPE/IQEC), 2013 Conference on and International Quantum Electronics Conference*, Munich (2013).
12. Pestov, D., Rasskazov, G., Ryabtsev, A., Pastirk, I., Dantus, M., "Shaper-based approach to real-time correction of ultrashort pulse phase drifts and transient pulse dispersion measurements", XVIIIth International Conference on Ultrafast Phenomena, EPJ Web of Conferences **41**, 11007 (2013).
13. Ryabtsev, A., Nie, B., Dantus, M., "Sub-50 fs pulses from frequency comb generated by cascaded four-wave mixing in highly-nonlinear fiber", *Conference on Lasers and Electro-Optics*, pp. CF1E.2, CLEO (2013).
14. Rasskazov, G., Ryabtsev, A., Lozovoy, V.V., Dantus, M., "Laser-induced dispersion control", *Conference on Lasers and Electro-Optics Europe - Technical Digest*, 6989393 (2014).
15. G. Rasskazov, A. Ryabtsev, M. Dantus, "Binary phase shaping for mitigating self-phase modulation", *Proc. SPIE 9344, Fiber Lasers XII: Technology, Systems, and Applications*, 934429 (2015).
16. A. Ryabtsev, S. Pouya, M. Koochesfahani, M. Dantus, "Characterization of vorticity in fluids by a spatially shaped laser beam", *Proc. SPIE 9343, Laser Resonators, Microresonators, and Beam Control* XVII, 93431G (2015).
17. G. Rasskazov, A. Ryabtsev, K. Charan, T. Wang, C. Xu, and M. Dantus, "Multi-soliton pulse characterization and compression," *International Conference on Ultrafast Phenomena, OSA Technical Digest*, paper UTh4A.27 (2016).

BIBLIOGRAPHY

BIBLIOGRAPHY

1. "The grand challenges of the office of science for u.S. Department of energy ", retrieved http://science.energy.gov/bes/efrc/research/grand-challenges.

2. "Big ideas for future national science foundation investments", retrieved https://www.nsf.gov/about/congress/reports/nsf_big_ideas.pdf.

3. R. Ell, U. Morgner, F. X. Kärtner, J. G. Fujimoto, E. P. Ippen, V. Scheuer, G. Angelow, T. Tschudi, M. J. Lederer, A. Boiko, and B. Luther-Davies, "Generation of 5-fs pulses and octave-spanning spectra directly from a ti:Sapphire laser," Opt Lett **26**, 373-375 (2001).

4. T. M. Fortier, A. Bartels, and S. A. Diddams, "Octave-spanning ti:Sapphire laser with a repetition rate >1 ghz for optical frequency measurements and comparisons," Opt Lett **31**, 1011-1013 (2006).

5. R. R. Alfano and S. L. Shapiro, "Observation of self-phase modulation and small-scale filaments in crystals and glasses," Phys Rev Lett **24**, 592-594 (1970).

6. T. A. Birks, W. J. Wadsworth, and P. S. J. Russell, "Supercontinuum generation in tapered fibers," Opt Lett **25**, 1415-1417 (2000).

7. P. M. Paul, E. S. Toma, P. Breger, G. Mullot, F. Augé, P. Balcou, H. G. Muller, and P. Agostini, "Observation of a train of attosecond pulses from high harmonic generation," Science **292**, 1689-1692 (2001).

8. E. Treacy, "Optical pulse compression with diffraction gratings," Ieee J Quantum Elect **5**, 454-458 (1969).

9. O. E. Martinez, J. P. Gordon, and R. L. Fork, "Negative group-velocity dispersion using refraction," J. Opt. Soc. Am. A **1**, 1003-1006 (1984).

10. R. L. Fork, O. E. Martinez, and J. P. Gordon, "Negative dispersion using pairs of prisms," Opt Lett **9**, 150-152 (1984).

11. R. Szipöcs, C. Spielmann, F. Krausz, and K. Ferencz, "Chirped multilayer coatings for broadband dispersion control in femtosecond lasers," Opt Lett **19**, 201-203 (1994).

12. F. Ouellette, "Dispersion cancellation using linearly chirped bragg grating filters in optical waveguides," Opt Lett **12**, 847-849 (1987).

13. D. E. Spence, P. N. Kean, and W. Sibbett, "60-fsec pulse generation from a self-mode-locked ti:Sapphire laser," Opt Lett **16**, 42-44 (1991).

14. A. Chong, J. Buckley, W. Renninger, and F. Wise, "All-normal-dispersion femtosecond fiber laser," Opt Express **14**, 10095-10100 (2006).

15. P. Devi, V. V. Lozovoy, and M. Dantus, "Measurement of group velocity dispersion of solvents using 2-cycle femtosecond pulses: Experiment and theory," Aip Adv **1**(2011).

16. A. M. Weiner, "Femtosecond pulse shaping using spatial light modulators," Review of Scientific Instruments **71**, 1929-1960 (2000).

17. V. V. Lozovoy, I. Pastirk, and M. Dantus, "Multiphoton intrapulse interference. Iv. Ultrashort laser pulse spectral phase characterization and compensation," Opt Lett **29**, 775-777 (2004).

18. B. Xu, J. M. Gunn, J. M. D. Cruz, V. V. Lozovoy, and M. Dantus, "Quantitative investigation of the multiphoton intrapulse interference phase scan method for simultaneous phase measurement and compensation of femtosecond laser pulses," Journal of the Optical Society of America B **23**, 750-759 (2006).

19. Y. Coello, V. V. Lozovoy, T. C. Gunaratne, B. Xu, I. Borukhovich, C.-h. Tseng, T. Weinacht, and M. Dantus, "Interference without an interferometer: A different approach to measuring, compressing, and shaping ultrashort laser pulses," Journal of the Optical Society of America B **25**, A140-A150 (2008).

20. A. Konar, Y. Shu, V. V. Lozovoy, J. E. Jackson, B. G. Levine, and M. Dantus, "Polyatomic molecules under intense femtosecond laser irradiation," The Journal of Physical Chemistry A **118**, 11433-11450 (2014).

21. A. Konar, V. V. Lozovoy, and M. Dantus, "Solvent environment revealed by positively chirped pulses," The Journal of Physical Chemistry Letters **5**, 924-928 (2014).

22. A. Konar, V. V. Lozovoy, and M. Dantus, "Stimulated emission enhancement using shaped pulses," The Journal of Physical Chemistry A **120**, 2002-2008 (2016).

23. M. T. Bremer and M. Dantus, "Standoff explosives trace detection and imaging by selective stimulated raman scattering," Appl Phys Lett **103**, 061119 (2013).

24. M. T. Bremer, P. J. Wrzesinski, N. Butcher, V. V. Lozovoy, and M. Dantus, "Highly selective standoff detection and imaging of trace chemicals in a complex background using single-beam coherent anti-stokes raman scattering," Appl Phys Lett **99**, 101109 (2011).

25. T. Juhasz, H. Frieder, R. M. Kurtz, C. Horvath, J. F. Bille, and G. Mourou, "Corneal refractive surgery with femtosecond lasers," Ieee J Sel Top Quant **5**, 902-910 (1999).

26. R. R. Krueger, J. Kuszak, H. Lubatschowski, R. I. Myers, T. Ripken, and A. Heisterkamp, "First safety study of femtosecond laser photodisruption in animal lenses: Tissue morphology and cataractogenesis," J Cataract Refr Surg **31**, 2386-2394 (2005).

27. B. N. Chichkov, C. Momma, S. Nolte, F. vonAlvensleben, and A. Tunnermann, "Femtosecond, picosecond and nanosecond laser ablation of solids," Appl Phys a-Mater **63**, 109-115 (1996).

28. X. Liu, D. Du, and G. Mourou, "Laser ablation and micromachining with ultrashort laser pulses," Ieee J Quantum Elect **33**, 1706-1716 (1997).

29. F. Krausz, M. E. Fermann, T. Brabec, P. F. Curley, M. Hofer, M. H. Ober, C. Spielmann, E. Wintner, and A. J. Schmidt, "Femtosecond solid-state lasers," Ieee J Quantum Elect **28**, 2097-2122 (1992).

30. G. Rasskazov, A. Ryabtsev, D. Pestov, B. Nie, V. V. Lozovoy, and M. Dantus, "Anomalous laser-induced group velocity dispersion in fused silica," Opt Express **21**, 17695-17700 (2013).

31. T. Ditmire, S. Bless, G. Dyer, A. Edens, W. Grigsby, G. Hays, K. Madison, A. Maltsev, J. Colvin, M. J. Edwards, R. W. Lee, P. Patel, D. Price, B. A. Remington, R. Sheppherd, A. Wooton, J. Zweiback, E. Liang, and K. A. Kielty, "Overview of future directions in high energy-density and high-field science using ultra-intense lasers," Radiat Phys Chem **70**, 535-552 (2004).

32. D. Yelin, D. Meshulach, and Y. Silberberg, "Adaptive femtosecond pulse compression," Opt Lett **22**, 1793-1795 (1997).

33. T. Baumert, T. Brixner, V. Seyfried, M. Strehle, and G. Gerber, "Femtosecond pulse shaping by an evolutionary algorithm with feedback," Appl Phys B-Lasers O **65**, 779-782 (1997).

34. M. M. Mielke, D. M. Gaudiosi, M. Hamamoto, K. Kim, R. Cline, and S. P. Sapers, "Pulse width stabilization for ultrafast laser systems," Physics Procedia **12, Part B**, 437-444 (2011).

35. A. Brun, P. Georges, G. Lesaux, and F. Salin, "Single-shot characterization of ultrashort light-pulses," J Phys D Appl Phys **24**, 1225-1233 (1991).

36. D. J. Kane, "Recent progress toward real-time measurement of ultrashort laser pulses," Ieee J Quantum Elect **35**, 421-431 (1999).

37. T. M. Shuman, M. E. Anderson, J. Bromage, C. Iaconis, L. Waxer, and I. A. Walmsley, "Real-time spider: Ultrashort pulse characterization at 20 hz," Opt Express **5**, 134-143 (1999).

38. V. R. Supradeepa, D. E. Leaird, and A. M. Weiner, "Single shot amplitude and phase characterization of optical arbitrary waveforms," Opt Express **17**, 14434-14443 (2009).

39. M. Lelek, F. Louradour, A. Barthelemy, and C. Froehly, "Time resolved spectral interferometry for single shot femtosecond characterization," Opt Commun **261**, 124-129 (2006).

40. D. Pestov, A. Ryabtsev, G. Rasskazov, V. V. Lozovoy, and M. Dantus, "Real-time single-shot measurement and correction of pulse phase and amplitude for ultrafast lasers," Opt Eng **53**(2014).

41. V. V. Lozovoy, I. Pastirk, K. A. Walowicz, and M. Dantus, "Multiphoton intrapulse interference. Ii. Control of two- and three-photon laser induced fluorescence with shaped pulses," J Chem Phys **118**, 3187-3196 (2003).

42. J. P. Ogilvie, D. Debarre, X. Solinas, J. L. Martin, E. Beaurepaire, and M. Joffre, "Use of coherent control for selective two-photon fluorescence microscopy in live organisms," Opt Express **14**, 759-766 (2006).

43. I. Pastirk, J. M. Dela Cruz, K. A. Walowicz, V. V. Lozovoy, and M. Dantus, "Selective two-photon microscopy with shaped femtosecond pulses," Opt Express **11**, 1695-1701 (2003).

44. B. Nie, D. Pestov, F. W. Wise, and M. Dantus, "Generation of 42-fs and 10-nj pulses from a fiber laser with self-similar evolution in the gain segment," Opt Express **19**, 12074-12080 (2011).

45. V. V. Lozovoy, B. Xu, Y. Coello, and M. Dantus, "Direct measurement of spectral phase for ultrashort laser pulses," Opt Express **16**, 592-597 (2008).

46. B. Hou, J. H. Easter, J. A. Nees, Z. He, A. G. R. Thomas, and K. Krushelnick, "Compressor optimization with compressor-based multiphoton intrapulse interference phase scan (miips)," Opt Lett **37**, 1385-1387 (2012).

47. G. Rasskazov, A. Ryabtsev, V. V. Lozovoy, and M. Dantus, "Laser-induced dispersion control," Opt Lett **39**, 3208-3211 (2014).

48. M. N. Islam, L. F. Mollenauer, R. H. Stolen, J. R. Simpson, and H. T. Shang, "Cross-phase modulation in optical fibers," Opt. Lett. **12**, 625-627 (1987).

49. R. J. Jones, K. D. Moll, M. J. Thorpe, and J. Ye, "Phase-coherent frequency combs in the vacuum ultraviolet via high-harmonic generation inside a femtosecond enhancement cavity," Phys Rev Lett **94**(2005).

50. R. A. Bartels, T. C. Weinacht, N. Wagner, M. Baertschy, C. H. Greene, M. M. Murnane, and H. C. Kapteyn, "Phase modulation of ultrashort light pulses using molecular rotational wave packets," Phys Rev Lett **88**, 139031-139034 (2002).

51. V. Kalosha, M. Spanner, J. Herrmann, and M. Ivanov, "Generation of single dispersion precompensated 1-fs pulses by shaped-pulse optimized high-order stimulated raman scattering," Phys Rev Lett **88**, 1039011-1039014 (2002).

52. Y. Coello, V. V. Lozovoy, T. C. Gunaratne, B. Xu, I. Borukhovich, C. H. Tseng, T. Weinacht, and M. Dantus, "Interference without an interferometer: A different approach to measuring, compressing, and shaping ultrashort laser pulses," Journal of the Optical Society of America B: Optical Physics **25**(2008).

53. L. Lepetit, G. Chériaux, and M. Joffre, "Linear techniques of phase measurement by femtosecond spectral interferometry for applications in spectroscopy," Journal of the Optical Society of America B: Optical Physics **12**, 2467-2474 (1995).

54. E. Tokunaga, A. Terasaki, and T. Kobayashi, "Frequency-domain interferometer for femtosecond time-resolved phase spectroscopy," Opt. Lett. **17**(1992).

55. P. Martin, S. Guizard, P. Daguzan, G. Petite, P. D'Oliveira, P. Meynadier, and M. Perdrix, "Subpicosecond study of carrier trapping dynamics in wide-band-gap crystals," Physical Review B - Condensed Matter and Materials Physics **55**, 5799-5810 (1997).

56. E. Tokunaga, A. Terasaki, and T. Kobayashi, "Femtosecond phase spectroscopy by use of frequency-domain interference," Journal of the Optical Society of America B: Optical Physics **12**, 753-771 (1995).

57. M. Sheik-Bahae, A. A. Said, T. H. Wei, D. J. Hagan, and E. W. Van Stryland, "Sensitive measurement of optical nonlinearities using a single beam," Ieee J Quantum Elect **26**, 760-769 (1990).

58. G. I. Stegeman, Contemporary Nonlinear Optics, 16-18 (1992).

59. A. M. Weiner, Ultrafast-Pulse Measurement Methods in Ultrafast Optics, 112-118 (2009).

60. L. Rapp, HAL: hal-00301019, http://hal.archives-ouvertes.fr/hal-00301019. (2008).

61. K. Dota, J. A. Dharmadhikari, D. Mathur, and A. K. Dharmadhikari, "Third-order nonlinear optical response in transparent solids using ultrashort laser pulses," Applied Physics B: Lasers and Optics **107**, 703-709 (2012).

62. S. Smolorz and F. Wise, "Femtosecond two-beam coupling energy transfer from raman and electronic nonlinearities," Journal of the Optical Society of America B: Optical Physics **17**, 1636-1644 (2000).

63. Q. Yang, G. Xu, X. Liu, J. Si, and P. Ye, "Phase-modulation-induced two-wave mixing in a temporal-nonlocal medium," Applied Physics B: Lasers and Optics **66**, 589-592 (1998).

64. M. Nisoli, S. Stagira, S. De Silvestri, O. Svelto, S. Sartania, Z. Cheng, M. Lenzner, C. Spielmann, and F. Krausz, "A novel-high energy pulse compression system: Generation of multigigawatt sub-5-fs pulses," Applied Physics B: Lasers and Optics **65**, 189-196 (1997).

65. G. Stibenz, N. Zhavoronkov, and G. Steinmeyer, "Self-compression of millijoule pulses to 7.8 fs duration in a white-light filament," Opt Lett **31**, 274-276 (2006).

66. A. R. Motamedi, A. H. Nejadmalayeri, A. Khilo, F. X. Kärtner, and E. P. Ippen, "Ultrafast nonlinear optical studies of silicon nanowaveguides," Opt Express **20**, 4085-4101 (2012).

67. N. K. Metzger, W. Lubeigt, D. Burns, M. Griffith, L. Laycock, A. A. Lagatsky, C. T. A. Brown, and W. Sibbett, "Ultrashort-pulse laser with an intracavity phase shaping element," Opt Express **18**, 8123-8134 (2010).

68. F. Shimizu, "Frequency broadening in liquids by a short light pulse," Phys Rev Lett **19**, 1097-1100 (1967).

69. P. Audebert, P. Daguzan, A. Dos Santos, J. C. Gauthier, J. P. Geindre, S. Guizard, G. Hamoniaux, K. Krastev, P. Martin, G. Petite, and A. Antonetti, "Space-time observation of an electron gas in sio2," Phys Rev Lett **73**, 1990-1993 (1994).

70. D. Grojo, M. Gertsvolf, S. Lei, T. Barillot, D. M. Rayner, and P. B. Corkum, "Exciton-seeded multiphoton ionization in bulk sio2," Physical Review B - Condensed Matter and Materials Physics **81**(2010).

71. C. Itoh, K. Tanimura, and N. Itoh, "Optical studies of self-trapped excitons in sio<inf>2</inf>," Journal of Physics C: Solid State Physics **21**, 4693-4702 (1988).

72. S. S. Mao, F. Quéré, S. Guizard, X. Mao, R. E. Russo, G. Petite, and P. Martin, "Dynamics of femtosecond laser interactions with dielectrics," Applied Physics A: Materials Science and Processing **79**, 1695-1709 (2004).

73. M. Sakakura, M. Terazima, Y. Shimotsuma, K. Miura, and K. Hirao, "Thermal and shock induced modification inside a silica glass by focused femtosecond laser pulse," J Appl Phys **109**(2011).

74. C. B. Schaffer, A. Brodeur, and E. Mazur, "Laser-induced breakdown and damage in bulk transparent materials induced by tightly focused femtosecond laser pulses," Measurement Science and Technology **12**, 1784-1794 (2001).

75. S. Tzortzakis, L. Sudrie, M. Franco, B. Prade, A. Mysyrowicz, A. Couairon, and L. Bergé, "Self-guided propagation of ultrashort ir laser pulses in fused silica," Phys Rev Lett **87**, 2139021-2139024 (2001).

76. C. Kalpouzos, W. T. Lotshaw, D. McMorrow, and G. A. Kenney-Wallace, "Femtosecond laser-induced kerr responses in liquid cs2," The Journal of Physical Chemistry® **91**, 2028-2030 (1987).

77. W. T. Lotshaw, D. McMorrow, C. Kalpouzos, and G. A. Kenney-Wallace, "Femtosecond dynamics of the optical kerr effect in liquid nitrobenzene and chlorobenzene," Chemical Physics Letters **136**, 323-328 (1987).

78. L. Bergé, S. Skupin, and G. Steinmeyer, "Temporal self-restoration of compressed optical filaments," Phys Rev Lett **101**(2008).

79. F. W. Wise, A. Chong, and W. H. Renninger, "High-energy femtosecond fiber lasers based on pulse propagation at normal dispersion," Laser and Photonics Reviews **2**, 58-73 (2008).

80. D. Pestov, G. Rasskazov, A. Ryabtsev, I. Pastirk, and M. Dantus, "Shaper-based approach to real-time correction of ultrashort pulse phase drifts and transient pulse dispersion measurements," in *EPJ Web of Conferences*, 2013),

81. A. J. Taylor, G. Rodriguez, and T. S. Clement, "Determination of n2 by direct measurement of the optical phase," Opt Lett **21**, 1812-1814 (1996).

82. G. P. Agrawal, Nonlinear Fiber Optics (1995).

83. D. Strickland and G. Mourou, "Compression of amplified chirped optical pulses," Opt Commun **56**, 219-221 (1985).

84. S. Zhou, F. W. Wise, and D. G. Ouzounov, "Divided-pulse amplification of ultrashort pulses," Opt Lett **32**, 871-873 (2007).

85. K. Wang and C. Xu, "Wavelength-tunable high-energy soliton pulse generation from a large-mode-area fiber pumped by a time-lens source," Opt Lett **36**, 942-944 (2011).

86. K. Beckwitt, F. W. Wise, L. Qian, L. A. Walker, and E. Canto-Said, "Compensation for self-focusing by use of cascade quadratic nonlinearity," Opt Lett **26**, 1696-1698 (2001).

87. C. Dorrer, R. G. Roides, J. Bromage, and J. D. Zuegel, "Self-phase modulation compensation in a regenerative amplifier using cascaded second-order nonlinearities," Opt Lett **39**, 4466-4469 (2014).

88. G. Rasskazov, A. Ryabtsev, V. V. Lozovoy, and M. Dantus, "Mitigating self-action processes with chirp or binary phase shaping," Opt Lett **41**, 131-134 (2016).

89. C. Froehly, B. Colombeau, and M. Vampouille, "Shaping and analysis of picosecond light-pulses," Progress in Optics **20**, 65-153 (1983).

90. A. M. Weiner, J. P. Heritage, and E. M. Kirschner, "High-resolution femtosecond pulse shaping," Journal of the Optical Society of America B **5**, 1563-1572 (1988).

91. A. M. Weiner, D. E. Leaird, J. S. Patel, and J. R. Wullert, "Programmable shaping of femtosecond optical pulses by use of 128-element liquid-crystal phase modulator," Ieee J Quantum Elect **28**, 908-920 (1992).

92. D. Eliyahu, R. A. Salvatore, J. Rosen, A. Yariv, and J.-J. Drolet, "Retardation and reduction of pulse distortion by group-velocity dispersion through pulse shaping," Opt Lett **20**, 1412-1414 (1995).

93. V. V. Lozovoy, B. Xu, J. C. Shane, and M. Dantus, "Selective nonlinear optical excitation with pulses shaped by pseudorandom galois fields," Phys Rev A **74**, 041805 (2006).

94. M. Comstock, V. V. Lozovoy, I. Pastirk, and M. Dantus, "Multiphoton intrapulse interference 6; binary phase shaping," Opt Express **12**, 1061-1066 (2004).

95. V. V. Lozovoy, T. C. Gunaratne, J. C. Shane, and M. Dantus, "Control of molecular fragmentation using binary phase-shaped femtosecond laser pulses," Chemphyschem **7**, 2471-2473 (2006).

96. P. J. Wrzesinski, D. Pestov, V. V. Lozovoy, B. W. Xu, S. Roy, J. R. Gord, and M. Dantus, "Binary phase shaping for selective single-beam cars spectroscopy and imaging of gas-phase molecules," J Raman Spectrosc **42**, 393-398 (2011).

97. M. Wichers and W. Rosenkranz, "Chirped duobinary transmission (cdbt) for mitigating the self-phase modulation limiting effect," in *Optical Fiber Communication Conference and International Conference on Quantum Information*, 2001 OSA Technical Digest Series (Optical Society of America, 2001), WDD43.

98. I. Pastirk, B. Resan, A. Fry, J. MacKay, and M. Dantus, "No loss spectral phase correction and arbitrary phase shaping of regeneratively amplified femtosecond pulses using miips," Opt Express **14**, 9537-9543 (2006).

99. M. Pessot, P. Maine, and G. Mourou, "1000 times expansion/compression of optical pulses for chirped pulse amplification," Opt Commun **62**, 419-421 (1987).

100. M. Sheik-bahae, A. A. Said, and E. W. Van Stryland, "High-sensitivity, single-beam n2 measurements," Opt Lett **14**, 955-957 (1989).

101. L. Kallel, B. Naudts, and A. Rogers, *Theoretical aspects of evolutionary computing*, Natural computing series (Springer, New York, 2001), pp. x, 497 p.

102. M. Dantus and V. V. Lozovoy, "Experimental coherent laser control of physicochemical processes," Chemical Reviews **104**, 1813-1860 (2004).

103. M. Hacker, G. Stobrawa, and T. Feurer, "Iterative fourier transform algorithm for phase-only pulse shaping," Opt Express **9**, 191-199 (2001).

104. S. Thomas, A. Malacarne, F. Fresi, L. Poti, and J. Azana, "Fiber-based programmable picosecond optical pulse shaper," J Lightwave Technol **28**, 1832-1843 (2010).

105. V. V. Lozovoy, G. Rasskazov, A. Ryabtsev, and M. Dantus, "Phase-only synthesis of ultrafast stretched square pulses," Opt Express **23**, 27105-27112 (2015).

106. E. Lichtman, A. A. Friesem, R. G. Waarts, and H. H. Yaffe, "Exact solution of four-wave mixing of copropagating light beams in a kerr medium," Journal of the Optical Society of America B: Optical Physics **4**, 1801-1805 (1987).

107. X. M. Liu, "Theory and experiments for multiple four-wave-mixing processes with multifrequency pumps in optical fibers," Physical Review A - Atomic, Molecular, and Optical Physics **77**(2008).

108. R. W. Tkach, A. R. Chraplyvy, F. Forghieri, A. H. Gnauck, and R. M. Derosier, "J. Lightwave technol," Lightwave Technol. **13**(1995).

109. S. Trillo, S. Wabnitz, and T. A. B. Kennedy, "Nonlinear dynamics of dual-frequency-pumped multiwave mixing in optical fibers," Phys Rev A **50**, 1732-1747 (1994).

110. S. Pitois, J. Fatome, and G. Millot, "Generation of a 160-ghz transform-limited pedestal-free pulse train through multiwave mixing compression of a dual-frequency beat signal," Opt Lett **27**, 1729-1731 (2002).

111. J. Fatome, S. Pitois, and G. Millot, "20-ghz-to-1-thz repetition rate pulse sources based on multiple four-wave mixing in optical fibers," Ieee J Quantum Elect **42**, 1038-1046 (2006).

112. R. Wu, V. R. Supradeepa, C. M. Long, D. E. Leaird, and A. M. Weiner, "Generation of very flat optical frequency combs from continuous-wave lasers using cascaded intensity and phase modulators driven by tailored radio frequency waveforms," Opt Lett **35**, 3234-3236 (2010).

113. V. R. Supradeepa and A. M. Weiner, "Bandwidth scaling and spectral flatness enhancement of optical frequency combs from phase-modulated continuous-wave lasers using cascaded four-wave mixing," Opt Lett **37**, 3066-3068 (2012).

114. S. Arismar Cerqueira Jr, J. M. C. Boggio, A. A. Rieznik, H. E. Hernandez-Figueroa, H. L. Fragnito, and J. C. Knight, "Highly efficient generation of broadband cascaded four-wave mixing products," Opt Express **16**, 2816-2828 (2008).

115. Y. Ozeki, S. Takasaka, J. Hiroishi, R. Sugizaki, T. Yagi, M. Sakano, and S. Namiki, "Generation of 1 thz repetition rate, 97 fs optical pulse train based on comb-like profiled fibre," Electronics Letters **41**, 1048-1050 (2005).

116. F. C. Cruz, J. D. Marconi, A. Cerqueira S. Jr, and H. L. Fragnito, "Broadband second harmonic generation of an optical frequency comb produced by four-wave mixing in highly nonlinear fibers," Opt Commun **283**, 1459-1462 (2010).

117. M. Hirano, T. Nakanishi, T. Okuno, and M. Onishi, "Silica-based highly nonlinear fibers and their application," Ieee J Sel Top Quant **15**, 103-113 (2009).

118. A. Ryabtsev, B. Nie, and M. Dantus, "45 fs optical pulses from phase corrected broadband cascaded four wave mixing products," Laser Phys Lett **10**(2013).

119. T. Inoue and S. Namiki, "Pulse compression techniques using highly nonlinear fibers," Laser and Photonics Reviews **2**, 83-99 (2008).

120. S. Asher and C. Johnson, "Raman spectroscopy of a coal liquid shows that fluorescence interference is minimized with ultraviolet excitation," Science **225**, 311-313 (1984).

121. F. M. Mitschke and L. F. Mollenauer, "Discovery of the soliton self-frequency shift," Opt Lett **11**, 659-661 (1986).

122. J. P. Gordon, "Theory of the soliton self-frequency shift," Opt Lett **11**, 662-664 (1986).

123. S. A. Dekker, A. C. Judge, R. Pant, I. Gris-Sánchez, J. C. Knight, C. M. de Sterke, and B. J. Eggleton, "Highly-efficient, octave spanning soliton self-frequency shift using a specialized photonic crystal fiber with low oh loss," Opt Express **19**, 17766-17773 (2011).

124. K. Wang, N. G. Horton, K. Charan, and C. Xu, "Advanced fiber soliton sources for nonlinear deep tissue imaging in biophotonics," Ieee J Sel Top Quant **20**(2014).

125. L.-C. Cheng, N. G. Horton, K. Wang, S.-J. Chen, and C. Xu, "Measurements of multiphoton action cross sections for multiphoton microscopy," Biomed. Opt. Express **5**, 3427-3433 (2014).

126. M. N. Islam, G. Sucha, I. Bar-Joseph, M. Wegener, J. P. Gordon, and D. S. Chemla, "Femtosecond distributed soliton spectrum in fibers," Journal of the Optical Society of America B **6**, 1149-1158 (1989).

127. J. M. Dudley, G. Genty, and S. Coen, "Supercontinuum generation in photonic crystal fiber," Rev Mod Phys **78**, 1135-1184 (2006).

128. X. Gu, L. Xu, M. Kimmel, E. Zeek, P. O'Shea, A. P. Shreenath, R. Trebino, and R. S. Windeler, "Frequency-resolved optical gating and single-shot spectral measurements reveal fine structure in microstructure-fiber continuum," Opt Lett **27**, 1174-1176 (2002).

129. B. Schenkel, R. Paschotta, and U. Keller, "Pulse compression with supercontinuum generation in microstructure fibers," Journal of the Optical Society of America B **22**, 687-693 (2005).

130. T. C. Wong, M. Rhodes, and R. Trebino, "Single-shot measurement of the complete temporal intensity and phase of supercontinuum," Optica **1**, 119-124 (2014).

131. J. M. Dudley, X. Gu, L. Xu, M. Kimmel, E. Zeek, P. O'Shea, R. Trebino, S. Coen, and R. S. Windeler, "Cross-correlation frequency resolved optical gating analysis of broadband continuum generation in photonic crystal fiber: Simulations and experiments," Opt Express **10**, 1215-1221 (2002).

132. H. Tu, Y. Liu, J. Lægsgaard, U. Sharma, M. Siegel, D. Kopf, and S. A. Boppart, "Scalar generalized nonlinear schrödinger equation-quantified continuum generation in an all-normal dispersion photonic crystal fiber for broadband coherent optical sources," Opt Express **18**, 27872-27884 (2010).

133. K. Wang, T.-M. Liu, J. Wu, N. G. Horton, C. P. Lin, and C. Xu, "Three-color femtosecond source for simultaneous excitation of three fluorescent proteins in two-photon fluorescence microscopy," Biomed. Opt. Express **3**, 1972-1977 (2012).

134. J. M. Dudley and S. Coen, "Coherence properties of supercontinuum spectra generated in photonic crystal and tapered optical fibers," Opt Lett **27**, 1180-1182 (2002).

135. N. G. Horton, K. Wang, D. Kobat, C. G. Clark, F. W. Wise, C. B. Schaffer, and C. Xu, "In vivo three-photon microscopy of subcortical structures within an intact mouse brain," Nat Photon **7**, 205-209 (2013).

136. V. V. Lozovoy, G. Rasskazov, D. Pestov, and M. Dantus, "Quantifying noise in ultrafast laser sources and its effect on nonlinear applications," Opt Express **23**, 12037-12044 (2015).

137. G. Rasskazov, V. V. Lozovoy, and M. Dantus, "Spectral amplitude and phase noise characterization of titanium-sapphire lasers," Opt Express **23**, 23597-23602 (2015).

138. E. R. Andresen, P. Berto, and H. Rigneault, "Stimulated raman scattering microscopy by spectral focusing and fiber-generated soliton as stokes pulse," Opt Lett **36**, 2387-2389 (2011).

139. K. Wang and C. Xu, "Tunable high-energy soliton pulse generation from a large-mode-area fiber and its application to third harmonic generation microscopy," Appl Phys Lett **99**, 071112 (2011).

140. K. A. Walowicz, I. Pastirk, V. V. Lozovoy, and M. Dantus, "Multiphoton intrapulse interference. 1. Control of multiphoton processes in condensed phases," J Phys Chem A **106**, 9369-9373 (2002).

141. P. S. Hsu, N. Jiang, J. R. Gord, and S. Roy, "Fiber-coupled, 10 khz simultaneous oh planar laser-induced fluorescence/particle-image velocimetry," Opt Lett **38**, 130-132 (2013).

142. U. Steinitz, Y. Prior, and I. S. Averbukh, "Laser-induced gas vortices," Phys Rev Lett **109**, 033001 (2012).

143. R. P. Feynman, R. B. Leighton, and M. L. Sands, *The feynman lectures on physics,* Definitive ed. (Pearson/Addison-Wesley, San Francisco, 2006).

144. C. Tropea, A. L. Yarin, and J. F. Foss, *Springer handbook of experimental fluid mechanics* (Springer, Berlin, 2007), pp. xxviii, 1557 p.

145. C. E. Willert and M. Gharib, "Digital particle image velocimetry," Experiments in Fluids **10**, 181-193 (1991).

146. M. Koochesfahani and D. G. Nocera, "Molecular tagging velocimetry," Handbook of Experimental Fluid Mechanics (2007).

147. M. B. Frish and W. W. Webb, "Direct measurement of vorticity by optical probe," J Fluid Mech **107**, 173-200 (1981).

148. B. A. Garetz, "Angular doppler-effect," J. Opt. Soc. Am. **71**, 609-611 (1981).

149. M. P. J. Lavery, F. C. Speirits, S. M. Barnett, and M. J. Padgett, "Detection of a spinning object using light's orbital angular momentum," Science **341**, 537-540 (2013).

150. O. Korech, U. Steinitz, R. J. Gordon, I. S. Averbukh, and Y. Prior, "Observing molecular spinning via the rotational doppler effect," Nature Photonics **7**, 711-714 (2013).

151. M. P. J. Lavery, S. M. Barnett, F. C. Speirits, and M. J. Padgett, "Observation of the rotational doppler shift of a white-light, orbital-angular-momentumcarrying beam backscattered from a rotating body," Optica **1**, 1-4 (2014).

152. M. Chen, M. Mazilu, Y. Arita, E. M. Wright, and K. Dholakia, "Dynamics of microparticles trapped in a perfect vortex beam," Opt Lett **38**, 4919-4922 (2013).

153. D. B. Phillips, M. P. Lee, F. C. Speirits, S. M. Barnett, S. H. Simpson, M. P. J. Lavery, M. J. Padgett, and G. M. Gibson, "Rotational doppler velocimetry to probe the angular velocity of spinning microparticles," Physical Review A - Atomic, Molecular, and Optical Physics **90**(2014).

154. A. Belmonte, C. Rosales-Guzmán, and J. P. Torres, "Measurement of flow vorticity with helical beams of light," Optica **2**, 1002-1005 (2015).

155. A. Ryabtsev, S. Pouya, A. Safaripour, M. Koochesfahani, and M. Dantus, "Fluid flow vorticity measurement using laser beams with orbital angular momentum," Opt Express **24**, 11762-11767 (2016).

156. J. Happel and H. Brenner, "Low reynolds number hydrodynamics - with special applications to particulate media," (1983).

157. S. Franke-Arnold, L. Allen, and M. Padgett, "Advances in optical angular momentum," Laser and Photonics Reviews **2**, 299-313 (2008).

158. A. Ryabtsev, S. Pouya, M. Koochesfahani, and M. Dantus, "Characterization of vorticity in fluids by a spatially shaped laser beam," in *Proceedings of SPIE - The International Society for Optical Engineering*, 2015),

159. S. I. Rubinow and J. B. Keller, "The transverse force on a spinning sphere moving in a viscous fluid," J Fluid Mech **11**, 447-459 (1961).

160. A. Braun, G. Korn, X. Liu, D. Du, J. Squier, and G. Mourou, "Self-channeling of high-peak-power femtosecond laser pulses in air," Opt Lett **20**, 73-75 (1995).

161. A. Couairon and A. Mysyrowicz, "Femtosecond filamentation in transparent media," Physics Reports **441**, 47-189 (2007).

162. A. Mysyrowicz, "Laser filament creates long-lived conducting 'wire' in air," Laser Focus World **43**, 15 (2007).

163. E. Frejafon, J. Kasparian, P. Rambaldi, B. Vezin, V. Boutou, J. Yu, M. Ulbricht, D. Weidauer, B. Ottobrini, E. De Saeger, B. Krämer, T. Leisner, P. Rairoux, L. Wöste, and J. P. Wolf, "Laser applications for atmospheric pollution monitoring," European Physical Journal D **4**, 231-238 (1998).

164. L. Wöste, S. Niedermeier, F. Ronneberger, H. Schillinger, R. Sauerbrey, C. Wedekind, H. Wille, P. Rairoux, B. Stein, S. Nikolov, and C. Werner, "Femtosecond atmospheric lamp," Laser Optoelektron. **29**, 51-53 (1997).

165. J. C. Diels, R. Bernstein, K. E. Stahlkopf, and X. M. Zhao, "Lightning control with lasers," Sci. Am. **277**, 50-55 (1997).

166. Y. Tamaki, J. Itatani, Y. Nagata, M. Obara, and K. Midorikawa, "Highly efficient, phase-matched high-harmonic generation by a self-guided laser beam," Phys Rev Lett **82**, 1422-1425 (1999).

167. K. Stelmaszczyk, P. Rohwetter, G. Méjean, J. Yu, E. Salmon, J. Kasparian, R. Ackermann, J. P. Wolf, and L. Wöste, "Long-distance remote laser-induced breakdown spectroscopy using filamentation in air," Appl Phys Lett **85**, 3977-3979 (2004).

168. J. B. Michael, M. R. Edwards, A. Dogariu, and R. B. Miles, "Femtosecond laser electronic excitation tagging for quantitative velocity imaging in air," Appl Optics **50**, 5158-5162 (2011).

169. S. Pouya, A. Van Rhijn, M. Dantus, and M. Koochesfahani, "Multi-photon molecular tagging velocimetry with femtosecond excitation (femtomtv)," Experiments in Fluids **55**(2014).

170. P. Rohwetter, J. Kasparian, K. Stelmaszczyk, Z. Hao, S. Henin, N. Lascoux, W. M. Nakaema, Y. Petit, M. Queißer, R. Salamé, E. Salmon, L. Wöste, and J. P. Wolf, "Laser-induced water condensation in air," Nature Photonics **4**, 451-456 (2010).

171. S. Henin, Y. Petit, P. Rohwetter, K. Stelmaszczyk, Z. Q. Hao, W. M. Nakaema, A. Vogel, T. Pohl, F. Schneider, J. Kasparian, K. Weber, L. Wöste, and J. P. Wolf, "Field measurements suggest the mechanism of laser-assisted water condensation," Nature Communications **2**(2011).

172. M. Matthews, S. Henin, F. Pomel, F. Théberge, P. Lassonde, J. F. Daigle, J. C. Kieffer, J. Kasparian, and J. P. Wolf, "Cooperative effect of ultraviolet and near-infrared beams in laser-induced condensation," Appl Phys Lett **103**(2013).

173. J. Ju, J. Liu, C. Wang, H. Sun, W. Wang, X. Ge, C. Li, S. L. Chin, R. Li, and Z. Xu, "Laser-filamentation-induced condensation and snow formation in a cloud chamber," Opt Lett **37**, 1214-1216 (2012).

174. H. Sun, J. Liu, C. Wang, J. Ju, Z. Wang, W. Wang, X. Ge, C. Li, S. L. Chin, R. Li, and Z. Xu, "Laser filamentation induced air-flow motion in a diffusion cloud chamber," Opt Express **21**, 9255-9266 (2013).

175. J. Ju, H. Sun, A. Sridharan, T. J. Wang, C. Wang, J. Liu, R. Li, Z. Xu, and S. L. Chin, "Laser-filament-induced snow formation in a subsaturated zone in a cloud chamber: Experimental and theoretical study," Physical Review E - Statistical, Nonlinear, and Soft Matter Physics **88**(2013).

176. A. Ryabtsev, S. Pouya, M. Koochesfahani, and M. Dantus, "Vortices in the wake of a femtosecond laser filament," Opt Express **22**, 26098-26102 (2014).

177. Y. Coello, V. V. Lozovoy, T. C. Gunaratne, B. Xu, I. Borukhovich, C. H. Tseng, T. Weinacht, and M. Dantus, "Interference without an interferometer: A different approach to measuring, compressing, and shaping ultrashort laser pulses," Journal of the Optical Society of America B: Optical Physics **25**, A140-A150 (2008).

178. V. V. Lozovoy, I. Pastirk, and M. Dantus, "Multiphoton intrapulse interference. Iv. Ultrashort laser pulse spectral phase characterization and compensation," Opt Lett **29**, 775-777 (2004).

179. Z. Sun, J. Chen, and W. Rudolph, "Determination of the transient electron temperature in a femtosecond-laser-induced air plasma filament," Physical Review E - Statistical, Nonlinear, and Soft Matter Physics **83**(2011).